SAPIENZA
UNIVERSITÀ DI ROMA

High-gradient structures and rf systems for high-brightness electron linacs

Università degli studi di Roma - La Sapienza

Dottorato di Ricerca in Fisica degli Acceleratori – XXXII Ciclo

Candidate

Marco Diomede
ID number 1068794

Thesis Advisor

Dr. Massimo Ferrario

Co-Advisor

Dr. David Alesini

A thesis submitted in partial fulfillment of the requirements
for the degree of Doctor of Philosophy in Physics

17 January 2020

Thesis defended on 18 February 2020
in front of a Board of Examiners composed by:

Prof. Andrzej Wolski (chairman)

Prof. Maria Cristina Morone

Prof. Daniele Davino

High-gradient structures and rf systems for high-brightness electron linacs
Ph.D. thesis. Sapienza – University of Rome

This thesis has been typeset by LaTeX and the Sapthesis class.

Version: January 21, 2020

Author's email: marco.diomede@uniroma1.it

Dedicated to
my family

Abstract

Free electron lasers (FELs) driven by linacs have demonstrated to be a reliable tool for studying matter. The demand of new FEL facilities is increasing and the main issues of this kind of machines are costs and required space.

In this framework, the INFN project named EuPRAXIA@SPARC_LAB, is a proposal to upgrade the SPARC_LAB test facility (in Frascati, Italy) to a soft X-ray user facility based on plasma acceleration and high-gradient X-band accelerating structures. Also the European project CompactLight aims to design a compact FEL for users, in the hard X-ray range. Its main pillars are a new concept high-brightness photoinjector, high-gradient X-band accelerating sections and innovative short-period undulators.

In this thesis work, the rf designs of the X-band linacs for both the mentioned projects have been performed.

In Chapter 1, there is a brief description of what a linac is, its main applications, characteristics and issues. Moreover, the state of the art of X-band technology for accelerators is briefly summarized.

In Chapter 2, main concepts about the characteristics and design criteria of traveling wave structures for electron linacs are described: main parameters of a traveling wave structure, constant impedance and constant gradient structures, the SLED pulse compressor system and rf power coupling design approaches.

In Chapter 3, the main concepts about rf vacuum breakdown, together with the main parameters that have been introduced through the years to predict its probability, are summarized.

Chapter 4 is dedicated to describe the main concepts about wakefields and beam instabilities: longitudinal and transverse wake functions and potentials, asymptotic solutions, the simplified single-bunch beam breakup two-particle model.

In Chapter 5, the work flow for the design of electron linacs with traveling wave structures is explained. In particular, the designs of the EuPRAXIA@SPARC_LAB and CompactLight linacs are described in detail. The work flow involves the following main steps:

- calculation of the minimum average iris radius of the structure based on two-particle model and asymptotic solution of wakefields;
- electromagnetic design of the regular cell, which goal is to maximize the rf efficiency and, at the same time, reduce the breakdown probability;
- analytical and numerical design and optimization of the accelerating structures, finding the optimal length and tapering as the best compromise between rf

efficiency and breakdown probability;

- sensitivity study of the cells due to mechanical errors;
- design of the rf power couplers, which goal is to minimize the power reflection at the input port and the multipolar components of the fields that can reduce the beam quality;
- design of an rf module that is repeated the number of times needed to reach the desired energy;
- design of high repetition rate schemes for FEL applications;
- calculation of the wake function for beam dynamics simulations;
- thermal analysis and preliminary design of the structure cooling system.

Chapter 6 is finally dedicated to conclusions and outlook.

Acknowledgments

First of all, I would like to thank David Alesini and Massimo Ferrario for the opportunity to work on this interesting topic and to join the SPARC_LAB group.

Then, I would like to thank many people that helped me with comments and suggestions: Sandro Gallo, Bruno Spataro, Valery Dolgashev, Alexej Grudiev, Muhammad Shumail, Valerio Lollo, Gianluca di Raddo, Cristina Vaccarezza, Fabio Cardelli, Luigi Faillace, Christofer Nantista, Marco Marongiu, Michele Croia, Simone Bini, Anna Giribono, Xiaowei Wu, Mikhail Zobov.

I also want to thank the Accelerator group at SBAI: Luigi Palumbo, Andrea Mostacci, Mauro Migliorati and Luca Ficcadenti for letting me use their laboratory but, most importantly, for what they have taught me.

Last but not least, I want to thank my family and my girlfriend for the endless love and support they always give me.

Contents

Abbreviations

BBU Beam BreakUp

BC Bunch Compressor

BDR Breakdown Rate

BOC Barrel Open Cavity

CG Constant Gradient

CI Constant Impedance

CLTE Coefficient of Linear Thermal Expansion

EBW Electron-Beam Welding

EM Electromagnetic

FEL Free Electron Laser

FEM Finite Element Method

HRRK High Repetition Rate Klystron

HXR Hard X-Ray mode

IOT Inductive Output Tube

LINAC LINear ACcelerator

LWFA Laser WakeField Acceleration

NEG Non-Evaporable Getter

PWFA Particle WakeField Acceleration

RF Radio Frequency

RMS Root Mean Square

SLED SLAC Energy Doubler

SW Standing Wave

SXR Soft X-Ray mode

TE Transverse Electric

TIG Tungsten Inert Gas

TM Transverse Magnetic

TW Traveling Wave

Symbols

Symbol	Description	Unit
a	Cell iris radius	m
a/λ	Cell iris radius normalized to the wavelength	
α	Attenuation per unit length	m^{-1}
α_L	Coefficient of linear thermal expansion	K^{-1}
b	Cell outer radius	m
B	Magnetic flux density	T
β_c	Coupling coefficient	
β	Betatron function	m
BDR	Breakdown rate	bpp/m
c	Speed of light	$\mathrm{m\,s}^{-1}$
c_ϵ	Specific heat	$\mathrm{J\,K}^{-1}$
C	Minimum circumference of the structure	m
d	Cell length	m
df/dx	Frequency sensitivity to mechanical errors	$\mathrm{Hz\,m}^{-1}$
dP/dz	RF power loss per unit length	$\mathrm{W\,m}^{-1}$
$d\phi/dx$	Phase advance per cell sensitivity to mechanical errors	$^\circ\,\mathrm{m}^{-1}$
δ	Skin depth	m
ΔT	Pulse temperature rise	°C
ΔT_c	Maximum difference in temperature of the accelerating part of the cell	°C
ΔT_w	Maximum difference between the water temperature and the cell temperature	°C
Δx	Off-axis circle center of the rf power coupler	m
E	Electric field	$\mathrm{V\,m}^{-1}$
E_{acc}	Average accelerating gradient of the cell	$\mathrm{V\,m}^{-1}$
E_e	Electric field emitted from SLED cavities	$\mathrm{V\,m}^{-1}$
E_L	Electric field from the SLED to the load	$\mathrm{V\,m}^{-1}$

Symbol	Description	Unit
E_s	Surface electric field	$\mathrm{V\,m^{-1}}$
E_z	longitudinal electric field	$\mathrm{V\,m^{-1}}$
E_{SLED}/E_K	Instantaneous electric field gain factor due to the SLED	$\mathrm{V\,m^{-1}}$
η	Klystron efficiency	
F	Lorentz force	N
f_{rf}	Frequency of the rf power	Hz
f_{rep}	Repetition rate of the klystron	Hz
g	Cell gap length	m
$g(z)$	Accelerating gradient profile	$\mathrm{V\,m^{-1}}$
g'_B	Equivalent quadrupole gradient due to B field	$\mathrm{T\,m^{-1}}$
g'_E	Equivalent quadrupole gradient due to E field	$\mathrm{T\,m^{-1}}$
G	Structure accelerating gradient	$\mathrm{V\,m^{-1}}$
$\langle G \rangle$	Average accelerating gradient of the structure	$\mathrm{V\,m^{-1}}$
G_0	Gradient at the beginning of the accelerating structure	$\mathrm{V\,m^{-1}}$
G'_B	Equivalent quadrupole gradient due to B field	T
G'_E	Equivalent quadrupole gradient due to E field	T
γ	Lorentz factor	
H	Magnetic field	A/m
$H_\parallel$	Tangential magnetic field	A/m
I	Beam current	A
I_k	Klystron current	A
I_{k0}	Nominal klystron current	A
k	Thermal conductivity	$\mathrm{W\,m^{-1}\,K^{-1}}$
k_z	Waveguide propagation constant along z	$\mathrm{m^{-1}}$
k_β	Betatron wave number	$\mathrm{m^{-1}}$
L_1	Distance between the first and the second accelerating section	m
L_2	Distance between the second and the third accelerating section	m
L_3	Distance between the third and the fourth accelerating section	m
L_c	Length of the rf power coupler	m
L_s	Length of the structure	m
L_t	Total active length of the linac	m
λ	Wavelength	m

Symbol	Description	Unit
λ_b	Longitudinal bunch distribution	$\mathrm{C\,m^{-1}}$
M	SLED energy multiplication factor	
$M_{\mp,s}$	Multiple component of the electromagnetic fields of order s	V
N_c	Number of cells	
N_m	Number of modules	
N_s	Number of structures	
N_{sm}	Number of structures per module	
ω_{rf}	Angular frequency of the rf power	$\mathrm{rad\,s^{-1}}$
p_{diss}	Average dissipated power per unit length	$\mathrm{W\,m^{-1}}$
P	RF power that flows into the structure	W
P_c	Dissipated power in the SLED cavity	W
P_{coll}	Power released on the tube collector	W
P_{diss}	Total dissipated power	W
P_e	Power emitted from the coupling aperture	W
P_{in}	RF power at the section input	W
P_k	Klystron power	W
P_{ks}	Fraction of klystron power per structure	W
P_l	SLED cavity net reflected power	W
P_{out}	RF power at the section output	W
$P_{rf\ sat}$	Klystron maximum rf power in saturation	W
ϕ	RF phase	°
ϕ_0	Phase advance per cell	°
q	Charge	C
Q	Quality factor	
Q_0	Unloaded quality factor	
Q_e	External quality factor	
Q_l	Loaded quality factor	
r	Shunt impedance per unit length	$\Omega\,\mathrm{m^{-1}}$
r_0	Cell edge rounding radius	m
r_1	Waveguide-slot rounding of the rf power coupler	m
r_2	Slot-matching cell rounding of the rf power coupler	m
r_1/r_2	Cell iris ellipticity	
r_s	Effective shunt impedance per unit length	$\Omega\,\mathrm{m^{-1}}$
r_{wg}	Waveguide rounding	m
R_c	Matching cell radius of the rf power coupler	m
ρ	r upon Q	$\Omega\,\mathrm{m^{-1}}$

Symbol	Description	Unit
S_{11}	Reflection coefficient at the input port	
S	Poynting vector	$\mathrm{W\,m^{-2}}$
S_c	Modified Poynting vector	$\mathrm{W\,m^{-2}}$
$S_{c\,max}/E_{acc}^2$	Peak normalized modified Poynting vector	$\mathrm{A\,V^{-1}}$
σ	Electrical conductivity	$\mathrm{S\,m^{-1}}$
σ_z	RMS bunch length	m
t	Cell iris thickness	m
t_f	Filling time	s
t_{ft}	Klystron flat top pulse length	s
t_k	Klystron pulse length	s
t_p	Pulse time	s
t_t	Klystron transient pulse length	s
T_c	SLED cavity filling time	s
τ	Signal time delay	s
τ_s	Section attenuation	
θ	Structure tapering angle	$^\circ$
Υ	Growth parameter	
V	Voltage gain	V
V_k	Klystron voltage	V
V_{k0}	Nominal klystron voltage	V
v_g	Group velocity	$\mathrm{m\,s^{-1}}$
v_g/c	Group velocity normalized to the speed of light	
v_{ph}	Phase velocity	$\mathrm{m\,s^{-1}}$
w	Slot width of the rf power coupler	m
w_c	Stored energy in the cavity per unit length	$\mathrm{J\,m^{-1}}$
$w_\parallel$	Longitudinal wakefield	$\mathrm{V\,C^{-1}}$
$w_\perp$	Transverse wakefield	$\mathrm{V\,C^{-1}\,m^{-1}}$
W	Energy	J
W_0	Beam energy at the linac entrance	eV
W_c	SLED cavity stored energy	J
W_f	Beam energy at the linac end	eV
W_{gain}	Beam energy gain	eV
W_{L_1}	Beam energy at the end of linac1	eV
$W_\parallel$	Longitudinal wake potential	$\mathrm{V\,C^{-1}}$
$W_\perp$	Transverse wake potential	$\mathrm{V\,C^{-1}\,m^{-1}}$
z	Longitudinal coordinate	m
Z_0	Impedance of free space	Ω

Chapter 1

Introduction

This thesis work is mainly centered on development and design of radio frequency linacs.

A *linear accelerator (linac)* is a device that allows to generate and accelerate charged particles (electrons, protons, ions) in a straight line. The main advantage of the linear accelerator is its capability to produce high-energy, high-intensity charged particle beams of excellent quality in terms of beam emittance and energy spread [1]. These devices found applications in different fields such as research, health and industry [2].

The acceleration can be obtained with constant or time-varying electric fields. In the second case, we can have two types of linacs: radio frequency (rf) and induction. In particular, in *rf linacs*, the particle acceleration is obtained by electromagnetic (EM) fields confined in resonant cavities fed by sinusoidally time-varying power sources.

The design and the application of a linac depend on the type of particle that is being accelerated: electrons, protons or ions. In research field, rf electron linacs are mainly used as injectors for synchrotrons and storage rings (like SPring-8 at RIKEN [3, 4], APS at Argonne National Laboratory [5, 6], PETRA III at DESY [7, 8], ESRF [9, 10], CHESS at Cornell University [11, 12]), free electron lasers (like LCLS at SLAC [13, 14], European XFEL [15, 16], PAL-XFEL at Pohang University of Science and Technology [17, 18], SACLA at RIKEN [19, 20], SwissFEL at PSI [21, 22]) and e^+-e^- colliders (like SuperKEKB at KEK [23, 24], BEPC II at Institute of High Energy Physics, Chinese Academy of Sciences [25, 26], VEPP-4M at BINP [27, 28], DAΦNE at LNF-INFN [29, 30]).

More in detail, in an rf linear accelerator for electrons, particles are generated and pre-accelerated in the *injector*, which main components are the gun, that generates electrons by thermionic or photo-electric effects [31–34], followed by accelerating structures and magnetic elements (typically solenoids) used to bunch and increase

the beam energy, keeping under control the transverse beam dynamics in terms of emittance increase [35]. The injector is typically followed by the main linac, made up of several accelerating sections interleaved by magnetic elements (typically quadrupoles) that accelerate the beam up to the desired energy. Beam trajectories and dimensions along the linac are measured by different types of diagnostic devices such as stripline or cavity beam position monitors and beam screens [36]. Control, cooling, vacuum and rf distribution and power systems complete the basic scheme of a linear accelerator. A simplified block diagram of a linac is shown in Fig. 1.1 [37].

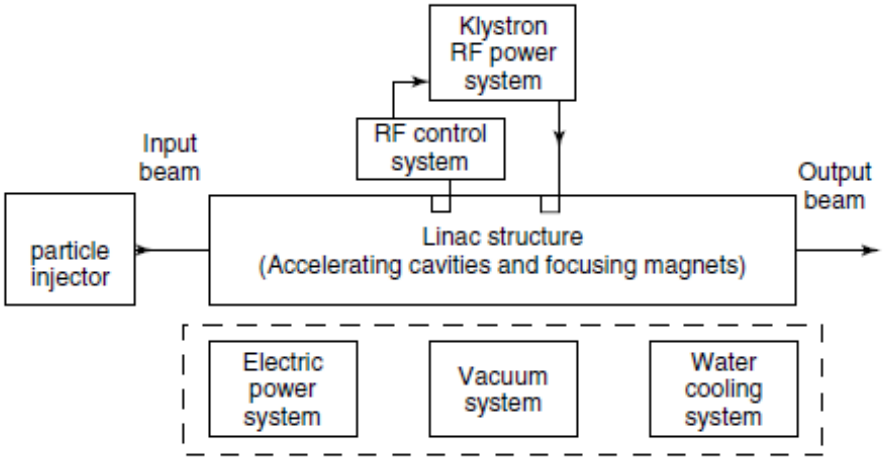

Figure 1.1. Simplified block diagram of a linac [37].

A strong impact on the size of an rf linac (especially in case of high-energy linacs) is the *frequency band* of the accelerating sections. The higher is the operational frequency, the higher is the maximum accelerating gradient that can be sustained in the sections. Indeed, the frequency dependence of rf breakdown level observed at low frequency continues to higher frequencies [38]. The main limits of using high-frequency technology are the beam transverse instabilites that can occour, generated by *wakefields*, due to the small trasnverse dimensions of the structures. In the microwave spectrum, the S-band has been successfully adopted for guns in user facilities [39–42]. Concerning the accelerating sections, the largest part of the facilities are based on S-band [43–46], while the C-band has been successfully adopted for facilities like SACLA [47] and SwissFEL [48]. Through the years, the X-band has been widely studied (see the following Section) but, up to now, there are no user facilities based on it.

Normal conducting rf linacs are generally operated at repetition rates (i.e. the number of shot per second) between 50 and 120 Hz. Nowadays, there is a high demand of light source facilities able to operate at higher repetition rates (1 kHz or above). The higher is the repetiton rate, the higher is number of photons produced

per second (photon flux). This request has been fulfilled with the adoption of the superconducting technology for linacs (like the European XFEL [15] and LCLS-II [49]). *Superconductivity* allows to minimise the power dissipation on the structure walls and therefore reduce the rf power required in each pulse [50]. The drawbacks of superconducting linacs are the high operational costs of the cryogenic plant and a maximum achievable gradient of ∼30 MV/m [51]. Power efficiency of normal conducting accelerating structures is much lower and the average power dissipated in klystrons and structures becomes the main issue. For normal conducting linacs, the repetition rate can be increased, at the expense of the average accelerating gradient, changing the high-voltage working point of the klystron and reducing the pulse duration (flat top and transient time, which is a characteristic of the modulator). This topic is described in Subsection 5.3.7.

In this framework, my thesis work has been oriented to the rf design of X-band linacs for two different projects, EuPRAXIA@SPARC_LAB [52] and CompactLight [53], which main goal, is to design a compact FEL facility for users. Considering the actual state of the art in terms of power sources and pulse compressor systems, I have designed the accelerating sections (optimized to have the best compromise between efficiency and breakdown probability), designed the power distribution waveguide network, performed calculations about possible klystron and linac configurations for high repetition rate operations, calculated the wake function of the accelerating structure for beam dynamics simulations, performed thermal analyses of the cell and a preliminary mechanical design of it.

1.1 Recent high-gradient results

Accelerating gradient is the main parameter that defines the compactness of an accelerator. Through the years, a lot of effort has been made on the R&D (research and development) of high-gradient technology. This allowed to make X-band a reliable technology for compact linacs. Thanks to the CERN-SLAC-KEK collaboration for the NLC/GLC linear colliders [54, 55], X-band traveling wave accelerating structures have been successfully operated at gradients higher than 100 MV/m [56–59]. At SLAC, short hard-copper-silver standing wave structures achieved gradients of 200 MV/m with breakdown rates of $\sim 10^{-3}$ breakdowns/pulse/m (bpp/m) [60].

RF vacuum breakdown

The main limit of high-gradient operations is rf vacuum breakdown (see Section 3). Up to now, there is no physical model that can correctly predict the breakdown behaviour [59]. Thus, studies are based on statistical considerations where the

breakdown rate has become a key parameter [61–64]. Many parameters have been introduced to try to predict the breakdown probability of accelerating structures: surface electric field [65], rf pulsed heating [66], power flow to iris circumference ratio [67], modified Poynting vector [68]. Scaling laws of these parameters have been found to predict the breakdown rate with different operating modes [62, 68, 69]. A good design approach is to keep all these parameters below fixed thresholds, which strongly depend on the requirements in terms of machine stability.

Materials and joining techniques

The most common metal used for room-temperature structures is copper, due to its high conductivity [70]. Several tests have demonstrated that hard Cu and hard CuAg structures have better high-gradient performances than soft Cu structures [59].

Many joining techniques have been developed: brazing, tungsten inert gas (TIG) welding, electron-beam welding (EBW) and diffusion bonding. When two workpieces of the same metallic material are heated locally above the melting temperature of the metal, this is *welding*. On the other hand, when a filler metal or alloy is used with a lower melting temperature than that of the two pieces to be joined (which can be different materials), this is *brazing* [70]. For accelerating structures, the most used technique is brazing. During the brazing process, the temperature (tipically 780 °C or higher) is such that the brazing alloy becomes liquid. Its drawback is that, after the brazing procedure, the structure becomes soft. *TIG welding* is characterized by the use of an inert gas (Ar) flow to shield the heated area around the joint from the oxidizing atmosphere, and a non-consuming tungsten electrode from which an arc forms to the workpiece to heat it locally. *Electron-beam welding* uses a finely (sub mm) focussed electron beam to vaporize (rather than melt) the workpiece near the joint to be. When joining copper pieces by EBW, the advantage compared to brazing is that only a small volume of copper is heated (annealed), while the bulk material will maintain its hardness. A *diffusion bond* is created between extremely smooth surfaces (optical finish) under high pressure ($>10\,\mathrm{N/mm^2}$) and temperature ($>350\,°\mathrm{C}$). As opposed to brazing, no melting takes place, but the filler material (e.g. Ag) diffuses into the workpiece.

Innovative short braze-free accelerating cavities joined with EBW and TIG processes have been designed and vacuum tested [71]. INFN is studying the possibility to register a patent about this technology. High-power tests on hard-copper TIG welded structures have been performed, showing the possibility to reach gradients about 145 MV/m at a breakdown rate of 10^{-3} bpp/m with 150 ns flat pulse [72]. Temperature has been monitored during TIG welding procedure showing a peak

temperature of ∼300 °C with a current of 140 A [73].

Accelerating structures are usually manufactured by precision turning of individual cells, and combined with precision milling for complex parts such as rf power couplers. These multiple parts are brazed into a complete structure. An alternative approach is the use of precision milling to cut cells into metal blocks that comprise either halves or quarters of the complete structure [74, 75]. A 11.994 GHz traveling-wave accelerating structure prototype for the Compact Linear Collider has been designed and fabricated, using the novel technique of assembling the structure from milled halves [76]. During high-power testing, the structure, assembled with brazing, reached a gradient of 100 MV/m at an rf breakdown rate of less than 1.5×10^{-5} bpp/m with a 200 ns pulse. A traveling wave open structure, joined with EBW, will be fabricated and high-power tested in the next months.

Cryogenic copper

One possible method to increase sustained electric fields in copper cavities is to cool them to temperatures below 77 K, where the rf surface resistance and coefficient of thermal expansion decrease, while the yield strength (which correlates with hardness) and thermal conductivity increase, all of which can affect the limits of sustained surface fields. X-band normal conducting standing wave structures working at cryogenic temperature (45 K) have been able to reach ∼250 MV/m at 10^{-3} bpp/m with a 150 ns pulse. For the same breakdown rate, the accelerating gradient is larger than that of room temperature structures of the same geometry [77].

Chapter 2

Traveling wave accelerating structures for electron linacs

A *traveling wave (TW) accelerating structure* is one of the best options to increase the kinetic energy of relativistic electrons [78]. Schematically, it is a circular waveguide with irises to slow down the phase velocity of the accelerating mode to the speed of light. The distance between the irises determines the phase advance per cell. In this kind of structures there is only the propagating wave, while in standing wave (SW) structures there is a superposition of counter-propagating waves that gives a standing wave.

In this chapter, the main parameters of a general accelerating structure are described together with the main concepts about the design of traveling structures, with or without the use of pulse compressor schemes.

2.1 Main design parameters

The *shunt impedance per unit length* r is the parameter that quantify the rf efficiency of an accelerating cell. It is defined as follows [79]:

$$r = -\frac{E^2(z)}{dP(z)/dz} = \frac{E_{acc}^2}{p_{diss}}, \tag{2.1}$$

where E is the *electric field amplitude of the fundamental synchronous space harmonic*, $dP(z)/dz$ is the *rf power loss per unit length*, E_{acc} is the *average axial accelerating field* and p_{diss} is the *average dissipated power per unit length.* It is defined as:

$$p_{diss} = \frac{P_{diss}}{d}, \tag{2.2}$$

where P_{diss} is the *total dissipated power in the cell* and d is the *cell length*. The higher is the shunt impedance, the higher is the rf efficiency of the cell, since the loss is lower and one needs less power to obtain the desired accelerating gradient. r is proportional to $f_{rf}^{1/2}$, where f_{rf} is the *frequency of the rf power* feeding the structure. Thus, from the efficiency point of view, a high operating frequency is desirable. The limit is due, from one side, to the fact that the higher is the frequency, the lower is the average power of commercially available sources. On the other side, higher frequency means also smaller cavity dimensions, this can be a problem for the beam stability along the accelerator and requirements for the tolerances of fabrication.

The *quality factor* (Q-factor) Q is defined as follows:

$$Q = -2\pi f_{rf} \frac{w_c}{dP/dz} = \omega_{rf} \frac{w_c}{p_{diss}}, \tag{2.3}$$

where w_c is the *stored energy per unit length* and ω_{rf} is the *angular frequency of the rf power*. Q is proportional to $f_{rf}^{-1/2}$.

ρ is a geometrical parameter that qualifies cavities. It is defined as:

$$\rho = \frac{r}{Q} = \frac{E^2}{\omega_{rf} w_c}, \tag{2.4}$$

It is proportional to f_{rf} and it does not depend on the kind of material the cavity is made up of.

The *phase velocity* v_{ph} of a wave is the velocity at which the phase of the wave propagates in time. It is defined as:

$$v_{ph} = \frac{\omega}{k_z}, \tag{2.5}$$

where k_z is the *waveguide propagation constant along z*.

The *group velocity* v_g is the speed at which the rf energy flows through the cavity. Its definition is:

$$v_g = \left. \frac{d\omega}{dk_z} \right|_{\omega=\omega_{rf}} = \frac{P}{w_c}, \tag{2.6}$$

where P is the *rf power that flows into the structure*. The group velocity depends on phase advance per cell, iris thickness, iris tip shape.

The *filling time* t_f is the time for the energy to propagate at the group velocity from the input to the output end of the structure. Its definition is:

$$t_f = \int_0^{L_s} \frac{dz}{v_g(z)}, \tag{2.7}$$

where L_s is the *length of the structure*. A high group velocity (i.e. large iris radius)

gives a small filling time.

In periodic structures, loss-free wave propagation can only occur if the wavelength is an integer multiple of the iris separation d. Hence, the irises only allow certain wavelengths, characterized by the number n, to travel in the longitudinal direction. These fixed wave configurations are called *operating modes* [80]. Every operating mode is characterized by its *phase advance per cell* ϕ_0, the phase shift introduced by each cell of the structure. It is defined as:

$$\phi_0 = \frac{2\pi}{n} = k_z d = \frac{\omega}{v_{ph}} d = \frac{\omega}{c} d, \tag{2.8}$$

where n is the *number of disks per guide wavelength*, v_{ph} is the phase velocity that, in TW structures accelerating ultra-relativistic bunches, is equal to the speed of light c. A value of $n = 3$ (i.e. $\phi_0 = 2\pi/3$) is close to optimum for accelerating structures having practical geometries [78].

From Eqs. (2.1)-(2.6), we obtain the energy conservation including wall losses and the interaction with the beam [81]:

$$\frac{dP}{dz} = -\frac{W\omega}{Q} - GI \tag{2.9}$$

and

$$\frac{dG}{dz} = -G(z)\alpha'(z) - \beta(z), \tag{2.10}$$

$$\alpha'(z) = \frac{1}{2}\left[\frac{1}{v_g}\frac{dv_g}{dz} - \frac{1}{\rho}\frac{d\rho}{dz} + \frac{\omega}{v_g Q}\right], \tag{2.11}$$

$$\beta(z) = I\frac{\omega\rho}{2v_g}, \tag{2.12}$$

where G is the *structure accelerating gradient* and I is the *beam current.*

$\alpha(z)$ is the *attenuation in nepers per unit length* and it is defined as:

$$\alpha(z) = \frac{1}{2}\frac{\omega}{v_g(z)Q(z)}. \tag{2.13}$$

The solution of Eq. (2.10) with $\beta(z) = 0$ (negligible beam loading, unloaded gradient) is:

$$G(z) = G_0 g(z), \tag{2.14}$$

where $G_0 = G(z = 0)$ is the *gradient at the beginning of the accelerating structure* and it is defined as:

$$G_0 = \sqrt{\frac{\omega\rho(0)P(0)}{v_g(0)}}, \tag{2.15}$$

and $g(z)$ is the *accelerating gradient profile*

$$g(z) = e^{-\int_0^z \alpha'(z')dz'} = \sqrt{\frac{v_g(0)}{v_g(z)}}\sqrt{\frac{\rho(z)}{\rho(0)}}e^{-\frac{1}{2}\int_0^z \frac{\omega}{v_g(z')Q(z')}dz'}. \tag{2.16}$$

From Eqs. (2.15) and (2.16) we obtain:

$$G(z) = G_z e^{-\frac{1}{2}\int_0^z \alpha(z')dz'}, \tag{2.17}$$

with

$$G_z = \sqrt{\frac{\omega\rho(z)P(0)}{v_g(z)}}. \tag{2.18}$$

Neglecting also the terms dv_g/dz and $d\rho/dz$, we have $\alpha'(z) = \alpha(z)$. Thus, the variation of the amplitude of the electric field along the structure is given by

$$dG/dz = -\alpha G, \tag{2.19}$$

while the rf power flow is given by

$$dP/dz = -2\alpha P. \tag{2.20}$$

From Eqs. (2.19) and (2.20), it follows that, in a certain position z, we have:

$$G(z) = G_0 e^{-\int_0^z \alpha(z')dz'}, \tag{2.21}$$

and

$$P(z) = P_0 e^{-2\int_0^z \alpha(z')dz'}, \tag{2.22}$$

where G_0 and P_0 are the values of the *electric field and power at the section input* (z=0).

When the beam loading is not negligible, one can use the approaches described in Refs. [81–83] for the design of accelerating structures.

The *section attenuation* τ_s is defined as the following:

$$\tau_s = \int_0^{L_s} \alpha(z)dz. \tag{2.23}$$

From Eqs. (2.22) and (2.23) we obtain:

$$P_{diss} = P_0 - P_{L_s} = P_0(1 - e^{-2\tau_s}), \tag{2.24}$$

with

$$\frac{P_{L_s}}{P_0} = \frac{P_{out}}{P_{in}} = e^{-2\tau_s}. \tag{2.25}$$

2.2 Constant impedance structures

Constant impedance (CI) structures have all cells of the same dimensions. This means that parameters like shunt impedance, Q-factor and group velocity are constant along itself. Considering Eq. (2.13), we have:

$$\alpha = \frac{1}{2}\frac{\omega}{v_g Q}. \tag{2.26}$$

Thus, Eq. (2.20) becomes:

$$dP/dz = -\frac{\omega P}{v_g Q}. \tag{2.27}$$

Solutions of Eqs. (2.21) and (2.22) are:

$$G(z) = G_0 e^{-\frac{1}{2}\frac{\omega}{v_g Q}z} \tag{2.28}$$

and

$$P(z) = P_0 e^{-\frac{\omega}{v_g Q}z}, \tag{2.29}$$

where, combining Eqs. (2.1) and (2.27), we have

$$G_0 = \sqrt{r_0 \frac{\omega P}{v_g Q}}. \tag{2.30}$$

The *energy gained by an electron* situated at a phase ϕ with respect to the crest[1] of the traveling wave is:

$$W = eV = e\cos\phi \int_0^{L_s} G(z)dz, \tag{2.31}$$

where V is the *voltage gain*. For a constant impedance structure we obtain:

$$V = G_0 L_s \left[\left(1 - e^{-\tau_s}\right)/\tau_s\right] cos\phi = (2\tau_s)^{\frac{1}{2}} \left[\left(1 - e^{-\tau_s}\right)/\tau_s\right] (P_0 r_0 L_s)^{\frac{1}{2}}\, cos\phi, \tag{2.32}$$

where

$$\tau_s = \alpha L_s = \frac{\omega L_s}{2 v_g Q}, \tag{2.33}$$

is the total attenuation in nepers in the accelerating structure.

The condition for maximum energy gain is $\tau_s = \frac{1}{2}\left(e^{\tau_s} - 1\right)$, which is satisfied for $\tau_s = 1.26$. With this optimum value of τ_s, the maximum energy gain is $V_{max} \approx 0.903\,(P_0 r_0 L_s)^{\frac{1}{2}} \cos\phi$.

[1] ϕ=0° is the on crest rf phase.

From Eq. (2.33), the filling time is:

$$t_f = \frac{L_s}{v_g} = \frac{2Q\tau_s}{\omega}. \tag{2.34}$$

For an accelerator optimized for the maximum energy gain, $t_f \approx 2.52Q/\omega$.

2.3 Constant gradient structures

In a constant gradient (CG) structure, the profile of the accelerating electric field along the structure itself is constant, while, in a constant impedance structure, it decays exponentially with z. In Fig. 2.1 [78], an example of the electric field profile in both the structures is shown.

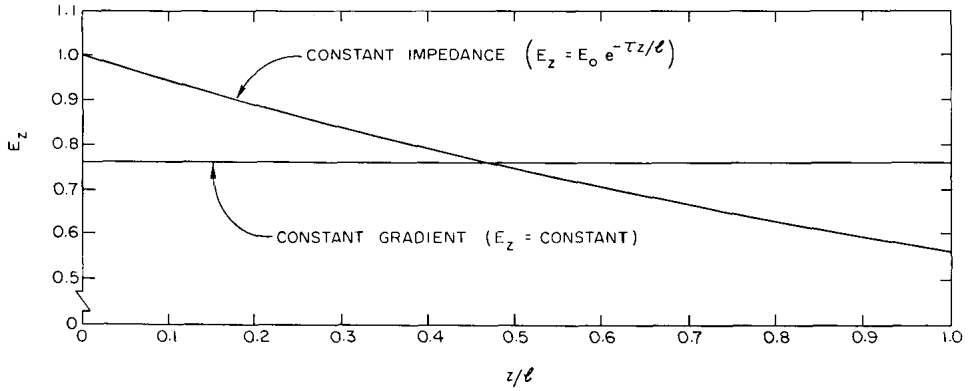

Figure 2.1. Example of electric field profile in constant impedance and constant gradient accelerator structures [78].

To have a closed solution of the problem, it is assumed that r and Q are constant along z (equal to the average values of the structure). Then, we still have:

$$\alpha = \frac{1}{2}\frac{\omega}{v_g Q}, \tag{2.35}$$

and

$$\tau_s = \alpha L_s = \frac{\omega L_s}{v_g Q}. \tag{2.36}$$

Thus, from Eq. (2.1), in order to have $G(z)$ constant, we must have:

$$dP/dz = constant. \tag{2.37}$$

The linear profile of $P(z)$ must be given by:

$$P(z) = P_0 - (P_0 - P_{L_s})\frac{z}{L_s} = P_0\left[1 - \frac{z}{L_s}\left(1 - e^{-2\tau_s}\right)\right]. \tag{2.38}$$

Eq. (2.38) gives:

$$dP/dz = -P_0\left(1 - e^{-2\tau_s}\right). \tag{2.39}$$

Combining Eq. (2.38) with (2.39), (2.1) and (2.3), we have:

$$v_g(z) = \frac{\omega L_s}{Q}\frac{\left[1 - \frac{z}{L_s}\left(1 - e^{-2\tau_s}\right)\right]}{\left(1 - e^{-2\tau_s}\right)}. \tag{2.40}$$

From Eq. (2.7) we obtain

$$t_f = \frac{2Q\tau_s}{\omega}. \tag{2.41}$$

The axial field strength can be obtained combining Eqs. (2.1) and (2.38):

$$G(z) = G_0 = \left[\frac{\left(1 - e^{-2\tau_s}\right)P_0 r_0}{L_s}\right]^{\frac{1}{2}}. \tag{2.42}$$

Integrating Eq. (2.42), over the structure length, we have:

$$V = G_0 L_s = \left[\left(1 - e^{-2\tau_s}\right)P_0 r_0 L_s\right]^{\frac{1}{2}}. \tag{2.43}$$

Comparing the energy gain of CI and CG structures as a function of the section attenuation, it can be observed that it is slightly higher for CG structures. An example is reported in Fig. 2.2 [78].

2.4 Time-dependent gradient

The solutions in Sections 2.2 and 2.3 are valid in steady state (flat pulses). Often, pulse compressor schemes like SLEDs [84] or BOCs [85] are used to increase the energy gain at the expense of the pulse length. Downstream these components, the pulse is not rectangular but has an exponential shape. A flat pulse can be still produced by using correction cavities [86] or pulse-shaping with low level rf systems.

The time evolution of the unloaded gradient along the structure is given by [81]:

$$G(z,t) = G_0[t - \tau(z)]g(z)H[t - \tau(z)], \tag{2.44}$$

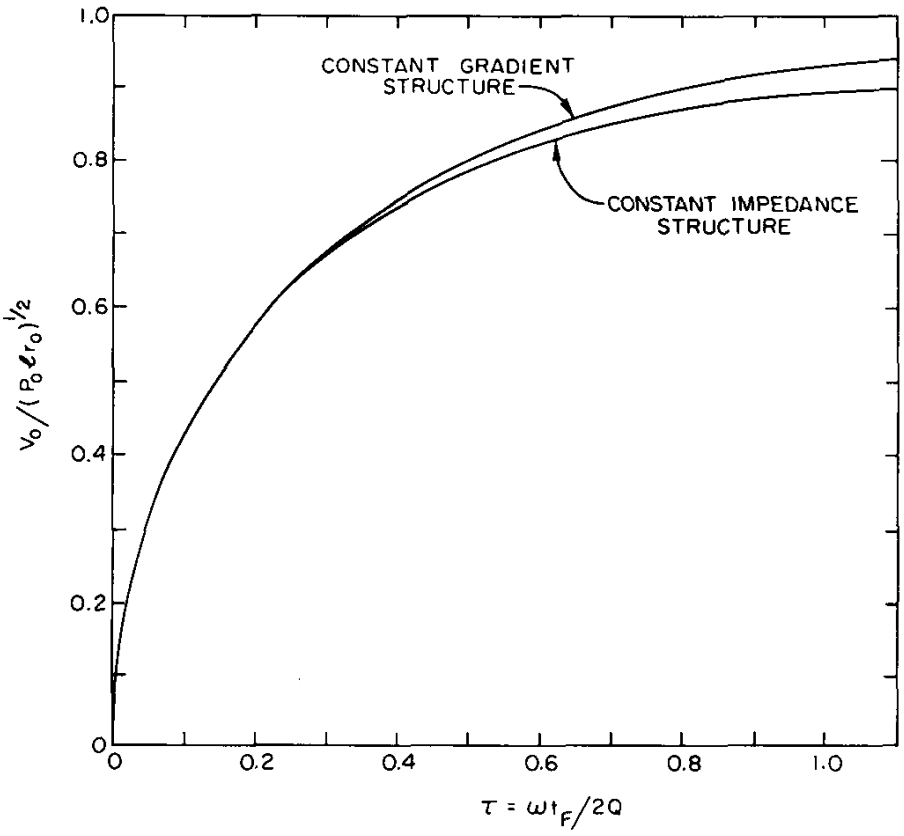

Figure 2.2. Example of energies gained in constant impedance and constant gradient structures as a function of the section attenuation [78].

where $H(t-\tau)$ is the Heaviside step function and

$$\tau(z) = \int_0^z \frac{dz'}{v_g(z')} \tag{2.45}$$

is the *signal time delay.*

Taking into account Eqs. (2.15) and (2.17), Eq. (2.45) can be rewritten as:

$$G(z,t) = \sqrt{P_0[t-\tau(z)]}\sqrt{\frac{\omega\rho(z)}{v_g(z)}}e^{-\frac{1}{2}\int_0^z \frac{\omega}{v_g(z')Q(z')}dz'} H[t-\tau(z)]. \tag{2.46}$$

2.5 SLED

During the years, a lot of effort has been made to increase the rf efficiency of the accelerators. An outstanding scheme has been invented at SLAC by P. Wilson, D. Farkas and H. Hogg. It has been called SLED [84], an acronym for SLAC Energy Doubler. A already mentioned, it allows to increase the peak rf power at the expense of the rf pulse width.

The SLED system, which is shown at the bottom of Fig. 2.3, has two major components: a 180° fast phase shifter on the drive side of the klystron and two high-Q ($Q_0 > 10^5$) cavities on the output side of the tube with a 3 dB coupler connected as shown [79]. During the first part of the pulse, the phase of the rf drive signal is reversed and the rf cavities fill up with energy with that phase. Because of the 3 dB coupler, no energy is reflected to the klystron. The fields emitted by the cavities algebraically add with the fields reflected by the cavity coupling irises, and the power flows towards the accelerator. Considering a single bunch operation, the phase of the drive signal is flipped back by 180° exactly one structure filling time (0.8 µs in the figure) before the end of the pulse. As a result, both cavities discharge their energy into the accelerator. The discharging pulse amplitude is increased by the fact that the klystron pulse adds to it.

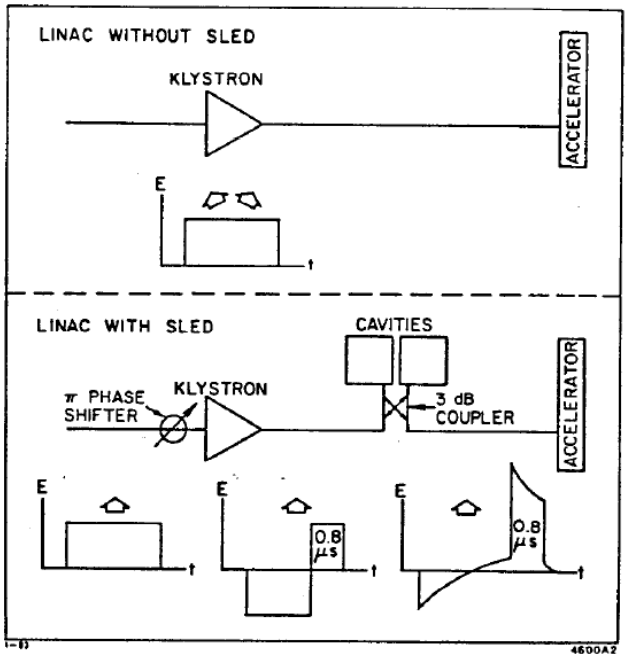

Figure 2.3. The SLED principle [79].

By the conservation of power we have [84]:

$$P_k = P_l + P_c + \frac{dW_c}{dt}, \tag{2.47}$$

where P_k is the incident power, P_l is the net reflected power (power delivered to the load), P_c is the power dissipated in the cavity and W_c is the energy stored in the cavity at time t.

The cavity filling time is

$$T_c = \frac{2Q_l}{\omega} = \frac{2Q_0}{\omega(1+\beta_c)}, \tag{2.48}$$

where

$$\beta_c = \frac{P_e}{P_c} = \frac{Q_0}{Q_e} \tag{2.49}$$

is the *cavity coupling coefficient*, the ratio of the power emitted from the coupling aperture P_e to the power dissipated in the cavity walls P_c and Q_l is the *loaded quality factor*.

Three time intervals can be defined (see Fig. 2.4): before the phase switch at time t_1 (A), between the phase shift and the end of the klystron pulse at time t_2 (B) and after the klystron pulse (C). The emitted fields in the three intervals are:

$$E_e(A) = -\alpha e^{-\tau} + \alpha; \qquad E_{e_1} = E_e(t_1) = -\alpha e^{-\tau_1} + \alpha; \tag{2.50}$$

$$E_e(B) = \gamma e^{-(\tau-\tau_1)} - \alpha; \qquad E_{e_2} = E_e(t_2) = \gamma e^{-(\tau_2-\tau_1)} - \alpha; \tag{2.51}$$

$$E_e(C) = E_{e_2} e^{-(\tau-\tau_2)}, \tag{2.52}$$

where

$$\alpha = \frac{2\beta_c}{(1+\beta_c)} = 2\frac{Q_l}{Q_e}, \tag{2.53}$$

$$\tau = \frac{t}{T_c}, \tag{2.54}$$

$$\gamma = \alpha\left(2 - e^{-\tau_1}\right) = 2\frac{Q_l}{Q_e}\left(2 - e^{-\frac{t_1\omega}{2Q_l}}\right). \tag{2.55}$$

The load fields are:

$$E_L(A) = E_e(A) - 1 = -\alpha e^{-\tau} + (\alpha - 1) \tag{2.56}$$

$$E_L(B) = E_e(B) + 1 = \gamma e^{-(\tau-\tau_1)} - (\alpha - 1) \tag{2.57}$$

$$E_L(C) = E_e(C) = \left[\gamma e^{-(\tau_2-\tau_1)}\right] e^{-(\tau-\tau_2)}. \tag{2.58}$$

The waveforms of direct wave from the klystron E_k, emitted wave from the cavities E_e, net load wave E_L and normalized energy gain as a function of time are shown in Fig. 2.4.

For a constant impedance structure, the maximum normalized energy gain, called *energy multiplication factor* M, is [87]:

$$M = \frac{V_{max}}{V_0}, \tag{2.59}$$

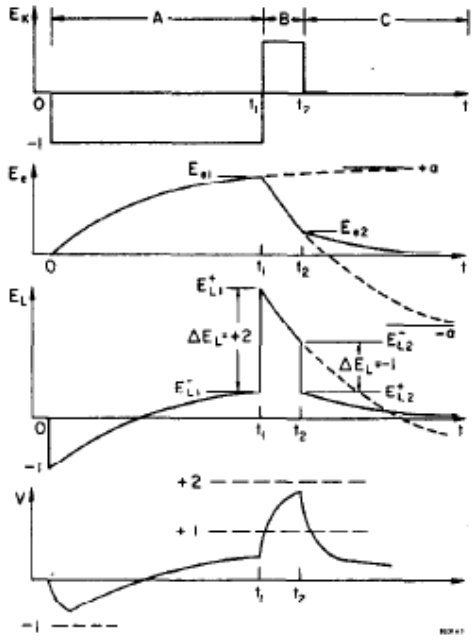

Figure 2.4. Main SLED waveforms [84].

where

$$V_{max} = (\alpha - 1)\frac{T_1}{T_a}\left(e^{-\frac{T_a}{T_1}} - 1\right) + \gamma\frac{T_2}{T_a}\left(e^{-\frac{T_a}{T_1}} - e^{-\frac{T_a}{T_c}}\right), \tag{2.60}$$

$$V_0 = \frac{T_1}{T_a}\left(1 - e^{-\frac{T_a}{T_1}}\right), \tag{2.61}$$

$$\frac{1}{T_1} = \frac{\omega}{2Q}, \tag{2.62}$$

with Q the quality factor of the cells in the structure,

$$\frac{1}{T_2} = \frac{1}{T_c} - \frac{\omega}{2Q}, \tag{2.63}$$

$$T_a = \frac{L_s}{v_g} \tag{2.64}$$

is the filling time of the CI structure.

For a constant gradient structure, the multiplication factor is [84]:

$$M = \gamma e^{-\frac{T_a}{T_c}}\frac{1 - (1-g)^{1+\nu}}{g(1+\nu)} - (\alpha - 1) \tag{2.65}$$

where

$$g = 1 - e^{-2\tau_s}, \tag{2.66}$$

$$T_a = \frac{L_s}{g v_{g0}} \ln\left(\frac{1}{1-g}\right) \tag{2.67}$$

is the filling time of the CG structure with v_{g0} the group velocity in the first accelerating cell and

$$\nu = \frac{T_a}{T_c \ln(1-g)}. \tag{2.68}$$

In both cases, the maximum energy gain is obtained for a compressed pulse length equal to the filling time of the structure.

2.6 Effective shunt impedance

In both Sections 2.2 and 2.3 it is possible to observe that the energy gain can be expressed as a function of the term $(P_0 L_s r_0)^{1/2}$. Thus, it is possible to rewrite the energy gain in terms of an *effective shunt impedance per unit length* r_s such that [82]:

$$V = (P_0 L_s r)^{\frac{1}{2}} = \left(\frac{r_s}{r}\right)^{\frac{1}{2}} (P_0 L_s r)^{\frac{1}{2}}, \tag{2.69}$$

and hence

$$r_s = \frac{V^2}{P_0 L_s} = \frac{V\langle G\rangle}{P_0} = \frac{\langle G\rangle^2 L_s}{P_0}, \tag{2.70}$$

with

$$\langle G\rangle = \frac{V}{L_s}. \tag{2.71}$$

r_s is a parameter that quantifies the rf efficiency of the whole structure, including pulse compressor schemes if considered in the machine layout.

2.7 RF power couplers

An rf power coupler is a crucial component of traveling wave structures. Its purpose is to transfer power from an rf power source to the structure itself [88]. The design of a power coupler is aimed to reduce reflections at the input port, minimize or avoid field distortions and reduce the probability of damages due to high surface magnetic fields. A low value of the reflection coefficient at the input port assures that only a negligible fraction of the rf power flows back to the source. The geometry of the coupler can, moreover, introduce an asymmetry in the electromagnetic field distribution. This can lead to a deterioration of the beam quality. Finally, as it will be described in Section 3.3, the breakdown probability in the coupler and damages of the coupler itself are related to magnetic field and pulsed heating [66, 89–91].

Through the years, many different geometries have been developed. Concerning the coupling based on waveguides, the most important couplers are *slot couplers*

and *mode-converter couplers* [92].

Slot couplers are the most compact ones and the accelerating mode is magnetically coupled to the waveguide one. An example of slot-type coupler is shown in Fig. 2.5 [88]. Coupling via slots introduces distortions in the field distribution and multipole components of the field can appear and affect the beam dynamics. It is possible to develop the magnetic field near the beam axis as follows [88]:

$$B_\theta(r,\theta,z) \cong A_0(z) + \sum_{n=1}^{\infty} A_n(z)\cos(n\theta)r^{n-1}, \tag{2.72}$$

where z is the longitudinal coordinate, r is the radial one and θ is the azimuthal angle. The A_n components are, in general, complex functions and depend on the longitudinal coordinate z. The dipole component corresponds to the term A_1, the quadrupole one to the term A_2 and so forth. With a symmetric feeding or a compensating slot, the odd magnetic fields components (i.e. dipole, sextupole, etc.) are suppressed but the even components (i.e. quadrupole, octupole, etc.) can still appear. A way to minimize the quadrupole field component is to introduce a deformed profile of the cell called *racetrack geometry* (see Fig. 2.6).

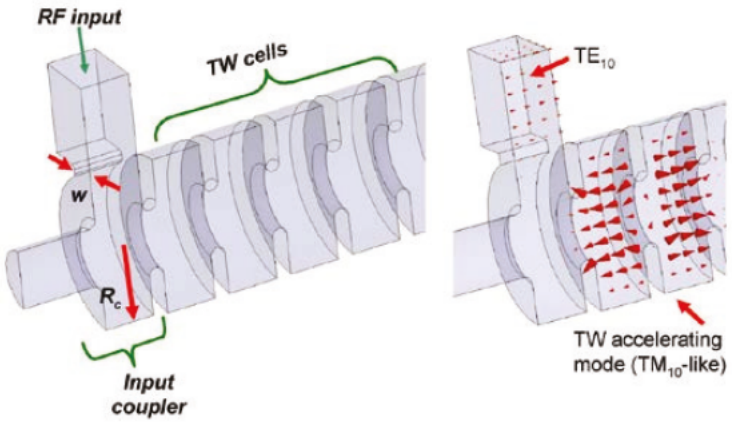

Figure 2.5. Slot-type coupler for a TW structure [88].

In mode-converter couplers, the TE_{01} mode of the waveguide is converted into the accelerating mode of the structure (TM_{01}-like). In *mode-launchers*, the rectangular waveguide is connected to the accelerating sections by means of a circular waveguide (Fig. 2.7(a)) and the TE_{01} mode is first converted into the TM_{01} one of the circular waveguide and then into the TM_{01}-like of the section. In *waveguide couplers*, the rectangular waveguide is directly connected to the accelerating section (Fig. 2.7(b)).

As already mentioned, the slot coupler is more compact but a high magnetic field can occur, leading to breakdowns and damages. On the other hand, mode-converter

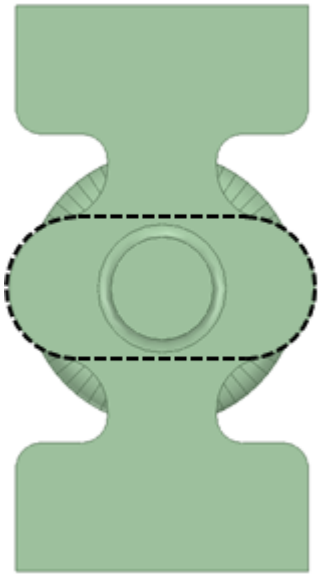

Figure 2.6. Racetrack geometry.

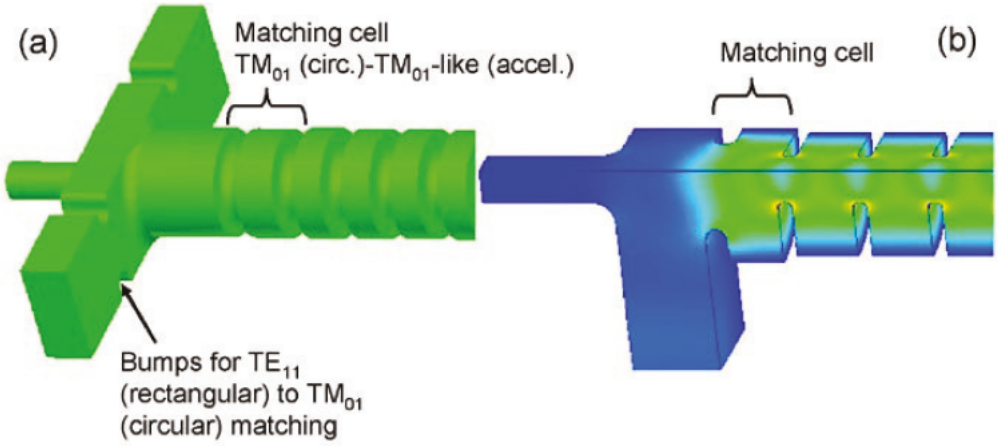

Figure 2.7. Mode-converter couplers: mode-launcher coupler (a) and waveguide coupler (b) [92].

couplers are larger but they completely avoid the problem of pulsed heating. With waveguide couplers, completely avoiding the quadrupole field component can be hard. All these considerations are summarized in Table 2.1.

Table 2.1. Characteristics of the main rf power couplers based on waveguides.

Coupler	**Longitudinal dimensions**	**Multipolar components of EM fields**	**Pulsed heating**
Slot	Only due to the matching cell	Quadrupolar component can be minimized with racetrack geometry	Pulsed heating can be high, it can be decreased increasing the radius of the matching cell
Waveguide	Rectangular waveguide and matching cell	Quadrupolar component can be minimized tapering the rectangular waveguide or inserting bumps, hard to control in both the waveguide and matching cell	Low pulsed heating
Mode-launcher	Rectangular and circular waveguide plus matching cell	Quadrupolar component can be minimized	Low pulsed heating

Chapter 3

Main parameters for vacuum rf breakdown prediction

The main phenomenon that limits the operational gradient in rf linear accelerator structures is the *vacuum rf breakdown*. The rf breakdown abruptly and significantly changes the transmission and reflection of the rf power that is coupled into an accelerating structure [64]. In traveling wave structures and waveguides where breakdown occurs, the transmitted power drops to unmeasurable levels with a decay time of 20–200 ns; up to 80% of the incident rf power is absorbed in the process. For standing wave structures, most of the input rf power is reflected. RF breakdown limits the power that can be coupled into the accelerating structure and produces irreversible surface damage in structures, rf components, and rf sources.

No quantitative theory to date satisfactorily explains and predicts rf beakdown levels in vacuum [68]. For this reason, the high gradient performances are mainly studied in a statistical way. One of the main quantitative parameters is the *breakdown probability*, the number of breakdowns per total number of rf pulses. The *operational gradient* is thus defined as the gradient at which the breakdown rate is below a certain defined limit that is assumed acceptable [64]. By definition, the operational gradient is lower than the maximum achievable gradient.

In this chapter, the main parameters for rf breakdown prediction that have been proposed through the years are described.

3.1 Scaling law of breakdown rate

Thanks to the CERN-SLAC-KEK collaboration for the NLC/GLC linear colliders [54, 55], a significant effort has been made to derive the high gradient limit due to rf breakdown and to collect all available experimental data both at 12 GHz (X-band) and at 30 GHz (K_a-band). In particular, the *breakdown rate (BDR)*, the probability

of a breakdown during an rf pulse, measured at certain gradients and pulse lengths.

Fitting the available data, the following power law has been found [68]:

$$\frac{G^{30}}{BDR} = const, \tag{3.1}$$

where G denotes the gradient at a fixed pulse length t_p. The choice of 30 for the power exponent is based on the analysis of the available experimental data only, and no assumption is made about the underlying physical mechanism. The dependence of gradient on pulse length at a fixed BDR has a well established scaling law which has been observed in multiple tests of travelling wave accelerating structures [62]:

$$G\, t_p^{1/6} = const. \tag{3.2}$$

Combining Eqs. (3.1) and (3.2), we obtain the single scaling law [68]:

$$\frac{G^{30}\, t_p^5}{BDR} = \frac{G^6\, t_p}{BDR^{1/5}} = const. \tag{3.3}$$

This scaling law can be applied to other parameters that will be described in the following Sections.

3.2 Surface electric fields and Kilpatrick's criterion

Kilpatrick's criterion [65] is based on the idea that breakdown happens when regular field emission is enhanced by a cascade of secondary electrons ejected from the surface by ion bombardment. The criterion was constructed putting together several investigators' experiences, data, and theories. It considers the probability of field-emitted electrons, together with a linear dependence of secondary-electron emission upon ion energy. Then there followed:

$$W E_s^2 e^{-\frac{K_1}{E_s}} = K_2, \tag{3.4}$$

where W is the maximum possible ionic energy (dc or rf) in electron volts, and E_s is the *electric surface gradient*. K_1 was established equal to 1.7×10^5 V/cm, and K_2 as 1.8×10^{14}. This criterion includes rf, dc, and pulsed dc, and specifies an upper limit for no vacuum sparking.

The maximum energy of an ion of mass M_0 and charge e, calculated from a relatively large gap of parallel plates and taking into account the transit time, was found to be [93]:

$$W = \frac{0.153 e E^2}{M_0 \pi f^2}, \tag{3.5}$$

from which the Kilpatrick criterion was derived as:

$$f[MHz] = 1.64\,(E_s[MV/m])^2\,e^{-\frac{8.5}{E_s[MV/m]}}. \tag{3.6}$$

The ion is assumed to be hydrogen. inverting Eq. (3.6), we obtain:

$$E_s[MV/m]e^{-\frac{4.25}{E_s[MV/m]}} = 24.7\sqrt{f[GHz]}. \tag{3.7}$$

We note that in derivation of this criterion, there is no concept of the breakdown probability which was introduced into accelerator field during NLC/GLC study [59, 61–63].

Nowadays, the Kilpatrick criterion is viewed as conservative and values of surface field exceeding the maximum allowed from this criterion are often reached.

The peak surface electric field should not exceed 220-250 MV/m in order to have a BDR below 10^{-6} bpp/m at pulse length of 200 ns [69]. The scaling law is then the following [69]:

$$\frac{E_s^6\,t_p}{BDR^{1/5}} = const. \tag{3.8}$$

3.3 RF pulsed heating

RF pulsed heating [94] is a process by which a metal is heated from rf magnetic fields on its surface. When the induced thermal stresses are larger than the elastic limit, microcracks and surface roughening will occur due to cyclic fatigue. Pulsed heating limits the maximum magnetic field on the surface and through it the maximum achievable accelerating gradient in a normal conducting accelerator structure.

RF heating of a metal surface was calculated with a 1D model using calculated *tangential magnetic field* $H_{\|}$ [94]. The *pulse temperature rise* ΔT is given by [66]:

$$\Delta T = \frac{|H_{\|}|^2\sqrt{t_p}}{\sigma\delta\sqrt{\pi\rho' c_\epsilon k}}, \tag{3.9}$$

where t_p is the pulse length, σ is the electrical conductivity, δ is the skin depth, ρ' is the density, c_ϵ is the specific heat, and k is the thermal conductivity of the metal. For copper, it is possible to use the formula:

$$\Delta T[^\circ C] = 127|H_{\|}[MA/m]|^2\sqrt{f_{rf}[GHz]\,t_p[\mu s]}. \tag{3.10}$$

In this simplified model, nonlinearities of the metal's physical properties are neglected.

As a general experimental rule, if this temperature rise exceeds ∼100 °C serious damage to the coupler region has a high probability of occurrence, below 50 °C

damage to the couplers is practically avoided while in the interval 50–100 °C there is some probability of coupler damage [88, 89].

Many experiments demonstrated that the waveguide-to-coupler irises in couplers are prone to breakdowns for low group velocity TW and SW structures [95]. The maximum gradient in all of these structures was limited by breakdowns in couplers. The damage was concentrated in input couplers [90]. Several solutions were successfully introduced [91]: a coupler with increased radius of waveguide-to-coupler-cell iris (to 3 mm from ∼80 µm); a mode-launcher coupler (temperature rise ∼3 °C); and a coupler with an rf choke in the rectangular waveguide.

3.4 Power flow through the structure and iris circumference

After analyzing data from many type of structures in the range of 3 to 30 GHz, another empirical general scaling of the breakdown limit has been derived [67]. The limit appears to be given by the quantity

$$\frac{P t_p^{1/3}}{C}, \tag{3.11}$$

where P is the power flow through the structure, t_p is the pulse length and C is the minimum circumference of the structure.

The ratio P/C should not exceed 2.3-2.9 MW/mm in order to have a BDR below 10^{-6} bpp/m at pulse length of 200 ns [69]. The scaling law is then the following [69]:

$$\frac{(P/C)^3\, t_p}{BDR^{1/5}} = const. \tag{3.12}$$

3.5 Modified Poynting vector

The *modified Poynting vector* is a local field quantity which gives the high gradient performance limit of accelerating structures in the presence of vacuum rf breakdown [68]. This parameter is defined as:

$$S_c = Re\{\bar{S}\} + \frac{1}{6} Im\{\bar{S}\}, \tag{3.13}$$

where $\bar{S}$ is the *Poynting vector in the frequency domain* and 1/6 is the weighting factor that better fits data. Its derivation is obtained considering the field emission of a cylindrical protrusion of height h and radius r surmounted by a hemispherical cap, proposed in Ref. [96]. In a traveling wave structure cell, S_c is dominated by the

reactive power flow from one cell to the next one and is concentrated near the iris tip, while in a standing wave structure cell, it is determined by the reactive power flow oscillating on each cycle. The modified Poynting vector should not exceed 4-5 W/µm^2 in order to have a BDR below 10^{-6} bpp/m at pulse length of 200 ns [69]. The scaling law of Eq. (3.1) can be then expressed as the following [69]:

$$\frac{S_c^3\, t_p}{BDR^{1/5}} = const. \tag{3.14}$$

As a general design criteria, the goal is to keep all these parameters below the thresholds, in order to guarantee good performances of the accelerating structures.

Chapter 4

Wakefields and instabilities in linear accelerators

4.1 Wakefields

When a charged particle travels across the vacuum chamber of an accelerator, it induces electromagnetic fields, which are left mainly behind the generating particle. These electromagnetic fields act back on the beam and influence its motion [97]. Such an interaction of the beam with its surroundings results in beam energy losses, alters the shape of the bunches and shifts the betatron and synchrotron frequencies. At high beam current, the fields can even lead to instabilities, thus limiting the performance of the accelerator in terms of beam quality and current intensity.

4.1.1 Longitudinal and transverse wakefields

The self-induced EM fields acting on a particle inside a beam depend on the whole charge distribution. The EM fields created by a point charge act back on the charge itself, and on any other charge of the beam. Referring to the coordinate system of Fig. 4.1, let us call $q_0(s_0, r_0)$ the source charge, traveling with constant longitudinal velocity $v = c$ (ultrarelativistic limit) along a trajectory parallel to the axis of a given accelerator structure. Let us consider a test charge q, in a position $(s = s_0 - z, r)$, which is moving with the same constant velocity on a parallel trajectory inside the structure.

Let E and B be the electric and magnetic fields generated by q_0 inside the structure. Since the velocity of both charges is along z, the *Lorentz force* acting on q has the following components:

$$F = q[E_z\hat{z} + (E_x - vB_y)\hat{x} + (E_y - vB_x)\hat{y}] = F_{\parallel} + F_{\perp}, \tag{4.1}$$

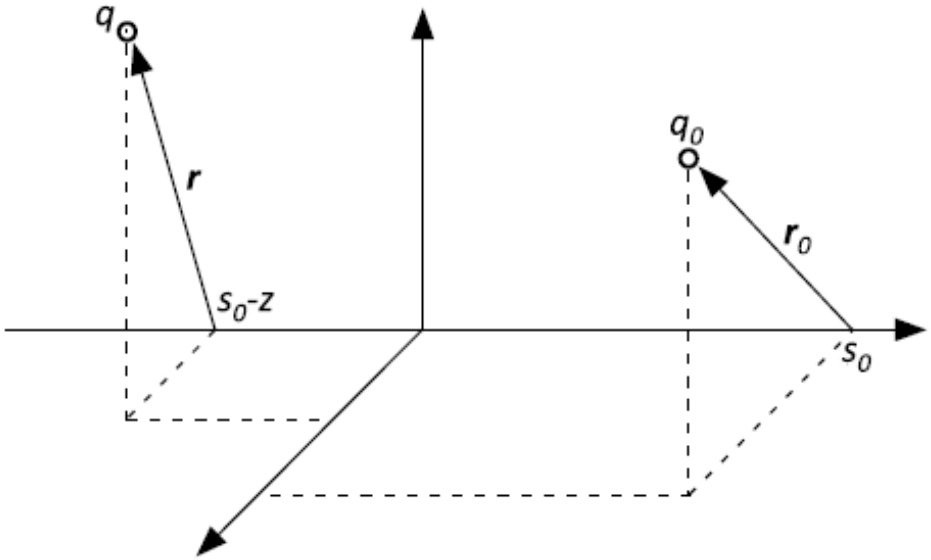

Figure 4.1. Reference coordinate system [97].

From Eq. (4.1), two effects on the test charge can occur: a longitudinal force, which changes its energy, and a transverse force, which deflects its trajectory. If we consider a device of length L, the *energy change* of q, due to this force is given by:

$$U(r, r_0, z) = \int_0^L F_{\parallel} ds \text{ [J]}, \tag{4.2}$$

and the *transverse deflecting kick*, is given by:

$$M(r, r_0, z) = \int_0^L F_{\perp} ds \text{ [Nm]}. \tag{4.3}$$

The quantities given by Eqs. (4.2) and (4.3), normalized to the two charges q_0 and q, are called the *longitudinal and transverse wakefields*, respectively. In many cases, we deal with structures having particular symmetric shapes, generally cylindrical. It is possible to demonstrate that, with a multipole expansion of the wakefields, the dominant term in the longitudinal wakefield only depends on the distance z between the two charges, while the dominant one in the transverse wakefield, although still a function of the distance z, is also linear with the transverse position of the source charge r_0. Dividing the transverse wakefield by r_0, we obtain the *transverse dipole wakefield*, that is the transverse wake per unit of transverse displacement, depending only on z. Thus, we have:

Longitudinal wakefield : $$w_{\parallel}(z) = -\frac{U}{q_0 q} \text{ [V/C]}, \tag{4.4}$$

Transverse wakefield: $$w_\perp(z) = \frac{1}{r_0}\frac{M}{q_0 q}\ [\mathrm{V/C/m}]. \tag{4.5}$$

The minus sign in the definition of the longitudinal wakefield means that the test charge loses energy when the wake is positive. A positive transverse wake means that the transverse force is defocusing. The wakefields are properties of the vacuum chamber and the beam environment, but they are independent of the beam parameters (bunch size, bunch length, etc.).

To study the effect of wakefields on the beam dynamics, it is convenient to distinguish between *short-range wakefields*, which are generated by the particles at the head of the bunch affecting trailing particles in the same bunch, and those that influence the multibunch (or multiturn) beam dynamics, which are generally resonant modes trapped inside a structure, and are called *long-range wakefields*.

The longitudinal and transverse short-range wakefields of a rectangular cell, as shown in Fig. 4.2 [98], have been derived under the hypothesis that the bunch length is much smaller than the pipe radius a. This approach is called *diffraction model* [99] and its expressions can be useful in studying the effects of the short-range wakefields of an accelerating structure in a linac. The model considers each cell

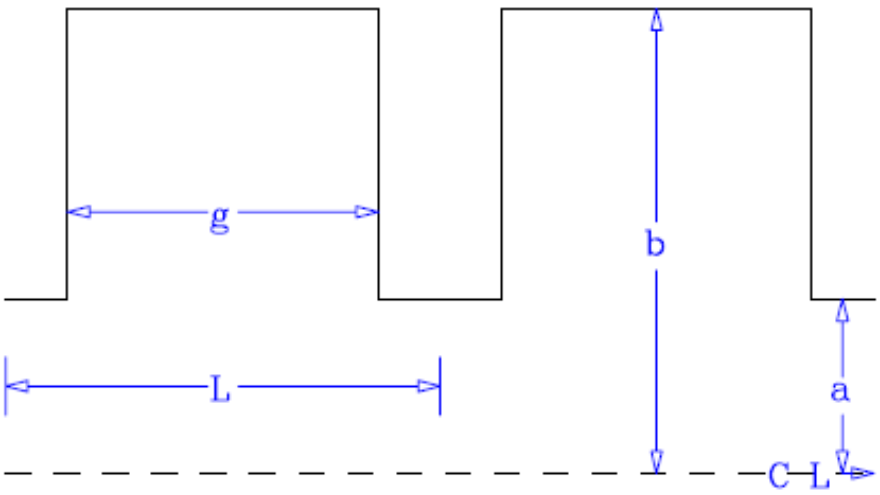

Figure 4.2. Geometry of a single cell of a linac accelerating structure [98].

as a pillbox cavity. When a bunch reaches the edge of the cavity, the EM field it creates is simply the one that would occur when a plane wave passes through a hole; using this hypothesis, it is possible to use the classical diffraction theory of optics to calculate the fields. If the condition $(g + \sigma_z/2)\sigma_z/2 < (b - a)^2$ is satisfied, where g is the cell gap, b is the cell radius, and σ_z is the rms bunch length of a Gaussian

bunch, the longitudinal and transverse wakefields can be written, respectively, as

$$w_{\parallel}(z) = \frac{Z_0 c}{\sqrt{2}\pi^2 a}\sqrt{\frac{g}{z}}, \tag{4.6}$$

$$w_{\perp}(z) = \frac{2^{\frac{3}{2}} Z_0 c}{\pi^2 a^3}\sqrt{gz}, \tag{4.7}$$

where $Z_0 = 120\pi\ \Omega$.

For a collection of cavities, Eqs. (4.6) and (4.7) cannot be used because the wakefields along the cells do not sum in phase and the result would be an overestimation of the effects. An asymptotic wakefield for a periodic collection of cavities of period L, has been numerically obtained at SLAC by K. Bane, for the design of the NLC linac, and then fitted with a simple function. Such wakefields are thus valid after a certain number of cavities given by [100]:

$$N_{cr} = \frac{a^2}{2g\left(\sigma_z + \frac{2a}{\gamma}\right)}. \tag{4.8}$$

Under these assumptions, the wakefields of Eqs. (4.6) and (4.7) are modified to [98, 101]:

$$w_{\parallel}(z) = \frac{Z_0 c}{\pi a^2} e^{-\sqrt{\frac{z}{s_1}}}, \tag{4.9}$$

$$w_{\perp}(z) = \frac{4 Z_0 c s_2}{\pi a^4}\left[1 - \left(1 + \sqrt{\frac{z}{s_2}}\right) e^{-\sqrt{\frac{z}{s_2}}}\right], \tag{4.10}$$

with

$$s_1 = 0.41\frac{a^{1.8} g^{1.6}}{L^{2.4}}, \tag{4.11}$$

$$s_2 = 0.17\frac{a^{1.79} g^{0.38}}{L^{1.17}}. \tag{4.12}$$

The model agrees with numerical results to within a few percent for constant impedance disk-loaded structures over a parameter range of $0.35 \leq a/L \leq 0.70$ and $0.55 \leq g/L \leq 0.90$, for a distance z up to $z/L \approx 0.15$. The model strongly depends on a/L but weakly on g/L. For detuned structures, with cell dimensions that vary within the structure, the structure wake is obtained by averaging the model wakes corresponding to the individual cell geometries.

For periodic structures, $w_{\parallel}(z)$ and $w_{\perp}(z)$ are respectively expressed in V/C/m and V/C/m^2.

4.1.2 Relationship between transverse and longitudinal forces

For ultra-relativistic particles, the differential relationship existing between longitudinal and transverse forces, and the corresponding wakefields, is given by the *Panofsky-Wenzel theorem* [102]:

$$\nabla_\perp F_\parallel = \frac{\partial}{\partial z} F_\perp, \tag{4.13}$$

$$\nabla_\perp w_\parallel = \frac{\partial}{\partial z} w_\perp. \tag{4.14}$$

The transverse gradient of the longitudinal force/wake is equal to the longitudinal gradient of the transverse force/wake.

4.1.3 Wake potentials and energy loss of a bunched distribution

When we have a bunch with total charge q_0 and longitudinal distribution $\lambda(z)$, such that $q_0 = \int_{-\infty}^{\infty} \lambda(z')dz'$, we can obtain the amount of energy lost or gained by a single charge q in the beam by using the superposition principle.

To this end, we calculate the effect on the charge by the whole bunch, as shown in Fig. 4.3, with the superposition principle, which gives the convolution integrals:

$$U(z) = -q \int_{-\infty}^{\infty} w_\parallel(z' - z)\lambda(z')dz'. \tag{4.15}$$

$$M(z) = r_0 q \int_{-\infty}^{\infty} w_\perp(z' - z)\lambda(z')dz'. \tag{4.16}$$

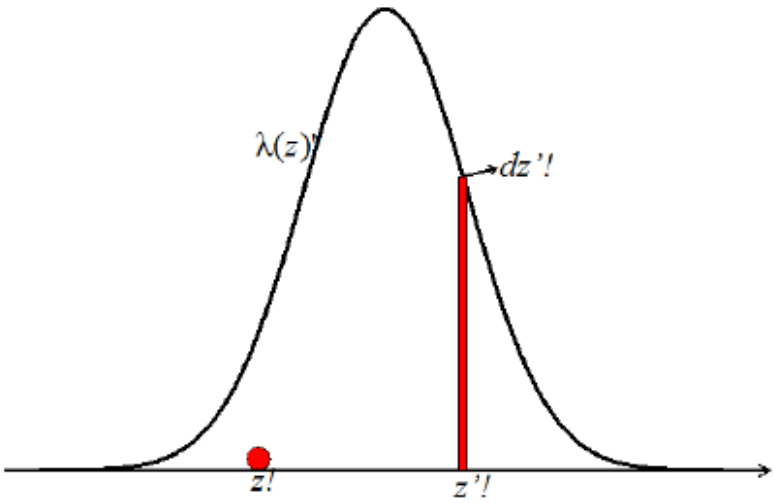

Figure 4.3. Convolution integral for a charge distribution to obtain the energy loss of a particle due to the whole bunch [97].

The *longitudinal wake potential* of a distribution $\lambda(z)$ is then defined as [103]:

$$W_{\parallel}(z) = -\frac{U(z)}{qq_0} = \frac{1}{q_0}\int_{-\infty}^{\infty} w_{\parallel}(z'-z)\lambda(z')dz'. \tag{4.17}$$

The *total energy lost by the bunch* is computed by summing the energy loss of all the particles:

$$U_{bunch} = \frac{1}{q}\int_{-\infty}^{\infty} U(z')\lambda(z')dz' = -q_0\int_{-\infty}^{\infty} W_{\parallel}(z')\lambda(z')dz'. \tag{4.18}$$

The *transverse wake potential* of a distribution $\lambda(z)$ is then defined as [103]:

$$W_{\perp}(z) = \frac{1}{r_0}\frac{M(z)}{qq_0} = \frac{1}{q_0}\int_{-\infty}^{\infty} w_{\perp}(z'-z)\lambda(z')dz'. \tag{4.19}$$

4.2 Single-bunch beam breakup: two-particle model

A beam injected off-centre in a linac, for example due to misalignments of the focusing quadrupoles, executes betatron oscillations. The bunch displacement produces a transverse wakefield in all the devices crossed during the flight, which deflects the trailing charges (*single-bunch beam breakup*), or other bunches following the first one in a multibunch regime (*multibunch beam breakup*). The first observation of beam breakup (BBU) was made at SLAC in 1966 [104].

A simplified treatment of the phenomena leading to the instability and giving us insight into its physics could be done using the so-called *two-particle model* [105]. In the two-particle model, the leading macroparticle, unperturbed by its own transverse wakefield, executes a free betatron oscillation:

$$y_1(s) = \hat{y}\, cos(k_\beta s), \tag{4.20}$$

where s is the distance coordinate along the linac and k_β is the betatron wave number. The trailing macroparticle, at a distance z behind, sees a deflecting wake field left behind by its leading partner. The equation of the transverse motion of the trailing macroparticle is:

$$\begin{aligned} y_2" + k_\beta^2 y_2 &= -\frac{Ne^2 w_{\perp}(z)}{2E} y_1 \\ &= -\frac{Nr_0 w_{\perp}(z)}{2\gamma}\hat{y}\, cos(k_\beta s), \end{aligned} \tag{4.21}$$

where Ne is the bunch charge, $E = \gamma m_0 c^2$ is the beam particle energy, $w_{\perp}(z)$ is the transverse wake function of the periodic structure and r_0 is the classical particle radius. In writing down Eqs. (4.20) and (4.21), it is assumed smooth betatron

focusing (i.e., k_β is independent of s). In Eq. (4.21), the acceleration of the beam energy is also ignored .

Equation (4.21) shows that the mechanism of beam breakup is that particles in the tail of the beam are driven exactly on resonance by the oscillating wake left by the head of the beam. The solution to Eq (4.21) is:

$$y_2(s) = \hat{y}\left[cos(k_\beta s) - \frac{Nr_0 w_\perp(z)}{4k_\beta\gamma} s\, sin(k_\beta s)\right], \tag{4.22}$$

in which the first term describes the free oscillation and the second term is the resonant response to the driving wake force. The amplitude of the second term grows linearly with s.

At the end of the linac, the oscillation amplitude of the bunch tail relative to the bunch head is characterized by the dimensionless *growth parameter* Υ:

$$\Upsilon = -\frac{Nr_0 w_\perp(z) L_t}{4k_\beta\gamma}, \tag{4.23}$$

where L_t is the total linac length. For short bunches, $w_\perp(z) < 0$ and Υ is positive.

For a beam bunch with realistic distribution, the wake field due to the off-axis motion of the bunch head deflects the bunch tail so that the bunch is distorted into a *banana shape*, as sketched in Fig. 4.4 [105].

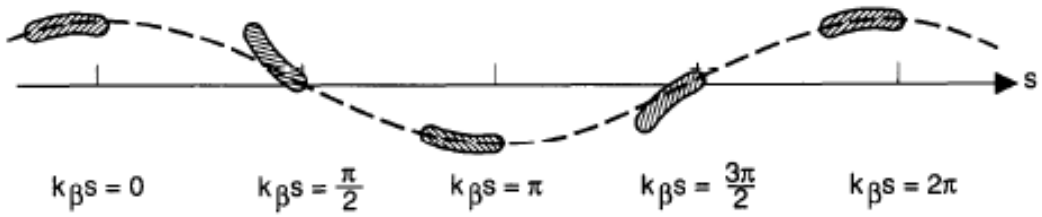

Figure 4.4. Sequence of snapshots of a beam undergoing dipole beam breakup instability in a linac [105].

In the previous calculations, the role of the acceleration has not been considered. It has a stabilizing action on the beam since, increasing the energy, it becomes more rigid and the effect of the wakefields is less. In presence of acceleration, the equation of the free betatron motion for the leading macroparticle is:

$$\frac{d}{ds}\left[\gamma(s)\frac{dy_1}{ds}\right] + k_\beta^2\gamma(s)y_1 = 0, \tag{4.24}$$

where the focusing strength is assumed increased proportionally to the beam energy.

It is also assumed a linear acceleration along the linac, thus the energy increase is:

$$\gamma(s) = \gamma_i(1 + \alpha s), \tag{4.25}$$

where $\gamma_i m_0 c^2$ is the beam energy at the injection. Considering the approximation $\alpha \ll k_\beta$, it is possible to obtain the solution for the trailing particle:

$$y_2(s) \approx \frac{\hat{y}}{\sqrt{1+\alpha s}} \left[cos(k_\beta s) - \frac{N r_0 w_\perp(z)}{4 k_\beta \gamma_i \alpha} \ln(1+\alpha s)\, sin(k_\beta s) \right]. \tag{4.26}$$

At the end of the linac $s = L_t$, the oscillation amplitude of the bunch tail relative to the bunch head is characterized by the growth parameter:

$$\Upsilon = -\frac{N r_0 w_\perp(z) L_t}{4 k_\beta \gamma_f} \ln \frac{\gamma_f}{\gamma_i}, \tag{4.27}$$

where $\gamma_f = \gamma_i(1 + \alpha L_t) \gg \gamma_i$ is the final is the final energy of the particle. The tail growth parameter in Eq. (4.27) can be obtained from Eq. (4.23) by simply replacing the factor L_t/γ by its integral counterpart $\int_0^{L_t} ds/\gamma(s)$. Due to the acceleration, the tail amplitude thus grows logarithmically with s rather than linearly, and the growth parameter is much reduced.

Chapter 5

Work flow of a linac design based on traveling wave structures

5.1 Introduction

There are many steps in the physics design and optimization of a linac based on traveling wave structures. The most important ones are:

- Choose a reference value of the accelerating field;
- Define the rf power sources and pulse compressor characteristics (if foreseen);
- Set the average iris radius of the accelerating structure according to beam dynamics requirements;
- Perform the electromagnetic design and optimization of the regular cell;
- Scan the total length and the iris tapering of the structure in order to find the highest structure effective shunt impedance and then reduce the total number of power sources;
- Verify that the peak value of modified Poynting vector at the nominal gradient is below the specifications;
- Perform wakefield simulations of the accelerating structure in order to calculate the growth parameter of the beam due to beam breakup effects;
- Finalize the electromagnetic design of the structure including input and output couplers verifying that breakdown predictors like pulsed heating have acceptable values;

- Design a realistic rf module with power distribution network;
- Perform termo-mechanical simulations of the structures and design the cooling system.

Several iterations among the steps are generally required.

The first step is to choose the reference accelerating gradient, which determines linac length and operating frequency band. Depending on the frequency band and the required repetition rate, one can choose the rf power source between the ones commercially available.

Another important step is to set the average iris radius of the accelerating sections. It is a crucial point because it affects the performance of the structures in terms of rf efficiency and beam stability. It strongly depends on linac optics and beam characteristics and it also affects the optimal structure length.

The electromagnetic design and optimization of the regular cell allows to find the geometry that maximise the shunt impedance, keeping under control the breakdown probability minimizing local quantities like modified Poynting vector (see Section 3.5) and temperature rise due to pulsed heating (see Section 3.3).

A constant impedance structure (see Section 2.2) has the simplest geometry but is, in general, not the best solution in terms of breakdown probability. Furthermore, the analytical solution of a constant gradient structure (see Section 2.3) is based on the approximation of r and Q constant along the structure itself. The solution gives a constant gradient only in steady state (flat pulses). For these reasons, we have developed a MATLAB code that is able to calculate the gradient profile of a structure and the main structure parameters, directly applying the cell parameters calculated with an electromagnetic solver like ANSYS HFSS or CST. The code is fully described in Subsection 5.2.5. The code is also able to calculate the peak value of modified Poynting vector and surface electric field along the structure at the nominal gradient.

Wakefield simulations allow to confirm if the preliminary estimations, based on approximations, about beam breakup effects were good.

Next step is the design of the couplers. As described in Section 2.7, the goal is to optimize the reflection coefficient at the input port, the multipole components of the magnetic field and the rf pulsed heating. An EM simulation of the whole structure allows to perform a fine tuning of it (mainly the couplers) and have the final geometry. The field maps allow to perform accurate beam dynamics simulations with particle tracking codes.

Once defined the main structure parameters, it is possible to design the rf module, i.e. an interconnection of accelerating structures, power sources, diagnostics, vacuum and optics elements. A sequence of this units allows to reach the desired beam

energy. In this process, the goal is to minimise the total number of klystrons needed to reach the final energy and then maximise the rf efficiency of the system.

Termo-mechanical simulations of the structures allow to understand if the average thermal load is acceptable or not and to design the cooling system.

In the next sections, many of these steps will be described as part of the linac design for two projects: EuPRAXIA@SPARC_LAB and CompactLight.

5.2 EuPRAXIA@SPARC_LAB

EuPRAXIA@SPARC_LAB [52, 106] (also named EuSPARC) is the proposal for the upgrade of the SPARC_LAB test facility [107] at INFN-LNF (Frascati, Italy). The goal is to design and build a new multi-disciplinary user-facility, equipped with a soft X-ray Free Electron Laser (FEL) driven by a $\sim$1 GeV high brightness linac based on plasma accelerator modules. This design study is performed in synergy with the Horizon 2020 Design Study EuPRAXIA (European Plasma Research Accelerator with eXcellence In Applications) [108, 109] which goal is to demonstrate exploitation of plasma accelerators for users. The EuPRAXIA@SPARC_LAB project is intended to put forward the Laboratori Nazionali di Frascati (LNF) in Italy as host of the EuPRAXIA European Facility.

In order to achieve this goal and to meet the EuPRAXIA requirements, some important preparatory actions must be taken at LNF:

- provide LNF with a new infrastructure with the size of about 130m$\times$30m, as the one required to host the EuPRAXIA facility;
- design and build the first-ever 1 GeV X-band rf linac and an upgraded FLAME laser up to the 0.5 PW range;
- design and build a compact FEL source, equipped with user beam line at 4–2 nm wavelength, driven by a high gradient plasma accelerator module.

The EuPRAXIA@SPARC_LAB facility by itself will equip LNF with a unique combination of a high brightness GeV-range electron beam generated in a state-of-the-art linac, and a 0.5 PW-class laser system. Even in the case of LNF not being selected and/or of a failure of plasma acceleration technology, the infrastructure will be of top-class quality, user-oriented and at the forefront of new acceleration technologies.

The EuPRAXIA@SPARC_LAB project requires the construction of a new building to host the linac, the FEL, the experimental room and the support laboratories. The new facility will cover approximately an area of 4000 m^2. The layout of the EuPRAXIA@SPARC_LAB infrastructure is schematically shown in Fig. 5.1. From

left to right one can see a 55 m long tunnel hosting a high brightness 150 MeV S-band rf photoinjector equipped with a hybrid compressor scheme based on both velocity bunching and magnetic chicane. The energy boost from 150 MeV up to a maximum 1 GeV will be provided by a chain of high gradient X-band rf cavities. At the linac exit a 5 m long plasma accelerator section will be installed, which includes the plasma module and the required matching and diagnostics sections. In the downstream tunnel a 40 m long undulator hall is shown, where the undulator chain will be installed. Further downstream, after a 12 m long photon diagnostic section, the users hall is shown. Additional radiation sources as THz and γ-ray Compton sources are foreseen in the other shown beam lines. The upper room is dedicated to host klystrons and modulators. In the lower light-blue room, the existing 300 TW FLAME laser, eventually upgraded up to 500 TW, will be installed. The plasma accelerator module can be driven in this layout either by an electron bunch driver (PWFA scheme) or by the FLAME laser itself (LWFA scheme). A staged configuration of both PWFA and LWFA schemes will be also possible in order to boost the final beam energy beyond 5 GeV. In addition, FLAME is supposed to drive plasma targets in the dark-blue room, in order to drive electron and secondary particle sources that will be available to users in the downstream 30 m long user area.

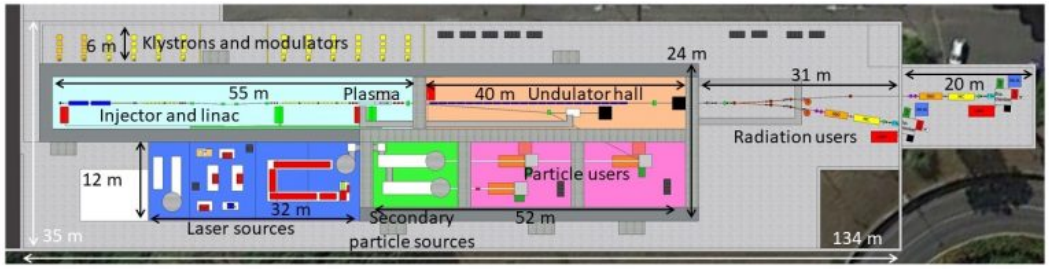

Figure 5.1. The layout of the EuPRAXIA@SPARC_LAB infrastructure.

The experimental activity will be initially focused on the realization of a plasma driven short wavelength FEL with one user beam line, according to the beam parameters reported in Table 5.1. EuPRAXIA@SPARC_LAB will then provide an FEL radiation spectrum in the so called "water window", a region in which water is transparent to soft X-rays (wavelength of 2.3 - 4.4 nm). The first foreseen FEL operational mode is based on the Self Amplification of Spontaneous Radiation (SASE) mechanism with tapered undulators. More advanced schemes like Seeded and Higher Harmonic Generation configurations will be also investigated. The users endstation, called EX-TRIM (Eupraxia X-ray Time Resolved coherent IMaging), will be designed and built to allow performing a wide class of experiments. As specific example of EuPRAXIA@SPARC_LAB applications, it is worth remarking that

the FEL radiation in the soft X-ray spectrum open possibilities for novel imaging methodologies and time-resolved studies in material science, biology and medicine, along with non-linear optics applications. For example:

Table 5.1. EuPRAXIA@SPARC_LAB's beam parameters for plasma and conventional rf linac driven FEL.

Parameter	Units	Full rf	LWFA	PWFA
Electron Energy	GeV	1	1	1
Repetition Rate	Hz	10	10	10
RMS Energy Spread	%	0.05	2.3	1.1
Peak Current	kA	1.79	2.26	2.0
Bunch charge	pC	200	30	200(D)-30(W)
RMS Bunch Length	µm (fs)	16.7 (55.6)	2.14 (7.1)	3.82 (12.7)
RMS normalized Emittance	mm mrad	0.5	0.47	1.1
Slice Length	µm	1.66	0.5	1.2
Slice Charge	pC	6.67	18.7	8
Slice Energy Spread	%	0.02	0.015	0.034
Slice normalized Emittance (x/y)	mm mrad	0.35/0.24	0.45/0.465	0.57/0.615
Undulator Period	mm	15	15	15
Undulator Strength $K(a_w)$		0.978 (0.7)	1.13 (0.8)	1.13 (0.8)
Undulator Length	m	30	30	30
ρ (1D/3D)	$\times 10^{-3}$	1.55/1.38	2/1.68	2.5/1.8
Radiation Wavelength	nm (keV)	2.87 (0.43)	2.8 (0.44)	2.98 (0.42)
Photon Energy	µJ	177	40	6.5
Photon per pulse	$\times 10^{10}$	255	43	10
Photon Bandwidth	%	0.46	0.4	0.9
Photon RMS Transverse Size	µm	200	145	10
Photon Brilliance per shot	$(\mathrm{s\,mm^2\,mrad^2\,bw}(0.1\%))^{-1}$	1.4×10^{27}	1.7×10^{27}	0.8×10^{27}

Coherent Imaging of Biological samples in the water window Exploiting the coherence of the FEL beam and its wavelength falling within the "water window", 2D and 3D images of biological samples in a wet environment can be obtained with high contrast with respect to the surrounding medium. This means that a wide class of biological objects, including protein clusters, viruses and cells can be profitably studied.

Clusters and nanoparticles In particular, great interest arises in the correlations between the geometric structure and electronic properties of variable size clusters, underlying changes in optical, magnetic, chemical and thermodynamic properties. In the spectral range from 3 to 5 nm envisaged for the FEL source, physical processes involving core levels are important.

Laser ablation plasma Laser ablation/desorption techniques are extensively utilized across a diverse range of disciplines, including production of new materials, and both extrinsic and in situ chemical analysis. In the case of ablation the use of ultra-fast laser pulses provides a powerful means of machining a wide variety of materials, including biological tissue. The absence of thermal relaxation of the energy allows unprecedented precision and essentially no associated damage, a fact that has stimulated considerable interest also for industrial processes and applications.

Electronically induced surface reactions in semiconductors, metal/adsorbate systems and multiphase composite materials could be investigated.

Condensed Matter Science Coherent Diffraction Imaging (CDI) experiments tackling many open questions in Condensed Matter physics. For instance, the quest for smaller and faster magnetic storage units is still a challenge of the magnetism. The possibility to study the evolution of magnetic domains with nanometer/femtosecond spatial/temporal resolution will shed light on the elementary magnetization dynamics such as spin–flip processes and their coupling to the electronic system.

Pump and probe experiments As an example, resonant experiments with pulses tuned across electronic excitation will open up the way towards stimulated Raman or four wave mixing spectroscopies.

5.2.1 Layout and main parameters of the linac

The electron beam acceleration schematic layout is reported in Fig. 5.2 [110]. The EuPRAXIA@SPARC_LAB accelerator is approximately 50 m long, the electron beam is generated in a twelve meters long high brightness SPARC-like S-band photoinjector described in Ref. [111]: 1.6 cell S-band rf gun where a Cu photocathode is mounted and driven by a 50 µJ Ti:Sapphire laser with a four coils solenoid for the emittance compensation; three TW SLAC type S-band linac sections follow for a final energy ranging between W = 100–230 MeV depending on the applied rf compression factor as described in [111, 112]. The downstream X-band rf linac can increase the electron beam energy up to W_{max} ≈1 GeV; at the X-band linac exit a Plasma Acceleration Structure (PLAS) is foreseen and after this two separate transfer lines deliver the electron beam to the Undulator and to the Compton Interaction point respectively. A four dipole magnetic chicane, 10 m long, is inserted in the X-band linac between the two sections Linac1 (L_1) and Linac2 (L_2), for longitudinal compression and phase space manipulation of the electron beam. In order to satisfy the requirements of the SASE FEL radiation source foreseen in the EuPRAXIA@SPARC_LAB project a FWHM bunch current of 2–3 kA must be delivered to entrance of the undulator at the energy of 1 GeV, with a very good emittance in the 6D phase space. The 1 GeV energy can be achieved by means of a single stage of plasma acceleration, a few centimeters long, coupled with the rf linac operating at 500 MeV (PWFA and LWFA cases of Table 5.1), or with the conventional operation of the Linac at twice the accelerating gradient in the X-band sections (Full rf case). The goal of the project is to operate plasma acceleration at approximately $10^{16}\,\mathrm{cm}^{-3}$, a plasma density that can be used to produce electric fields of 1–2 GV/m and characterized by a plasma wavelength of $\lambda_p \approx 300\,\mu\mathrm{m}$ that allows for realistic bunch separation with the use of a COMB technique [112, 113].

Such accelerating gradients are tailored for specific envisioned experiment [114, 115], where the foreseen parameters will allow for good beam loading compensation and lower quality depletion. This matches with the chosen plasma input energy of 500 MeV, highly rigid bunch, that limits transverse bunch evolution and the consequent transverse emittance dilution within the plasma.

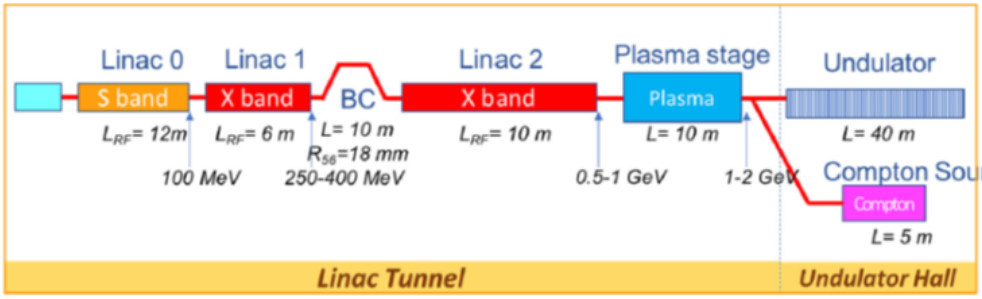

Figure 5.2. EuPRAXIA@SPARC_LAB electron beam acceleration schematic layout. In this lego scheme the main structures lengths are reported together with the rf active length (L_{rf}), and the "Plasma Interaction" box embeds also the injection/extraction beamline [110].

The baseline chosen technology for the EuPRAXIA@SPARC_LAB booster is X-band. The X-band booster design has been driven by the need of a high accelerating gradient required to achieve a high facility compactness, which is one of the main goals of the EuPRAXIA project. The total space allocated for the linac accelerating sections is ∼25 m, corresponding to an active length L_t of ∼16 m taking into account the space required to accommodate beam diagnostics, magnetic elements, vacuum equipment and flanges. Two average accelerating gradient options are foreseen for the X-band linac: 57 MV/m (named Full rf) and 80 MV/m (named Ultimate), corresponding to double the power of the Full rf case. The rf linac layout is based on klystrons with SLEDs that feed several TW accelerating structures. The operating mode is the $2\pi/3$ mode at 11.9942 GHz. The rf power source is the CPI VKX-8311A klystron [116]. Its main parameters are summarized in Table 5.2.

The Full rf linac configuration is meant to provide a 200 pC electron beam able to drive SASE-FEL radiation and/or Compton interaction with the laser pulse. The high charge electron beam coming from the photoinjector is accelerated with the linac and the final longitudinal compression for the SASE-FEL operation occurs in the magnetic chicane, located between L_1 and L_2 linac sections, according to a hybrid scheme of longitudinal compression: velocity bunching in the photoinjector plus magnetic compression in the linac. The X-band linac mainly consists of two sections, L_1 and L_2, located before and after the magnetic chicane respectively. The maximum accelerating gradient applied is $G = 57$ MV/m through all L_1 and

Table 5.2. Main parameters of CPI VKX-8311A klystron.

Parameter	Value
Beam Voltage	410 kV
Beam Current	310 A
Frequency	11.994 GHz
Peak Power	50 MW
Average Power	5 kW
Sat. Gain	48 dB
Efficiency	40 %
Duty	0.009 %

L_2, to reach the required energy and energy spread for the electron beam in the conventional rf operation scheme. An increased power configuration can be also progressively implemented in a machine upgrade plan to provide overhead and flexibility to the operation, and ultimately to reach higher beam energies with the accelerating gradient raised up to 80 MV/m (Ultimate). Between L_1 and L_2, a 10 m long magnetic chicane is foreseen for phase space manipulation and/or longitudinal compression of the bunch; at the same time when the chicane dipoles are switched off, the straight beamline accommodates the middle energy diagnostic station for beam parameters measurement. The two linac sections L_1 and L_2 have been optimized to provide the required beam acceptance, from photo-injector and after the magnetic chicane, for the considered working points. In Table 5.3, the main parameters of L_1 and L_2 are reported.

Table 5.3. EuPRAXIA@SPARC_LAB's main linac parameters.

Beam Parameter	Unit	L1			L2		
		PWFA	LWFA	Full rf	PWFA	LWFA	Full rf
Initial energy W_0	MeV	102	98	171	222	212	502
Final energy W_f	MeV	222	212	502	582	550	1052
Active Linac length	m		6.0			10.0	
Acc. Gradient $\langle G \rangle$	MV/m	20.0	20.0	57.0	36.0	36.0	57.0
RF phase (0 crest)	deg	0	-20.0	-15.0	0	-19.5	+15.0
Initial energy spread	%	0.15	0.27	0.67	0.11	0.15	0.59
Final energy spread	%	0.11	0.15	0.59	0.07	0.07	0.14
Final Bunch length σ_z	µm	6(W)	5	112	7	5	16

5.2.2 Minimum average iris radius of the structure

Once the main linac parameters are defined, it is possible to set the minimum average iris radius of the structure.

Let us consider a linear energy gain along the linac:

$$W(z) = W_0 + e\langle G\rangle z. \tag{5.1}$$

From Eq. (4.27), for a bunch length σ_z we obtain:

$$|\Upsilon| = \frac{Ne w_\perp(\sigma_z)}{4k_\beta\langle G\rangle}\ln\left(\frac{W_f}{W_0}\right), \tag{5.2}$$

where $W_f = W(z = L_t)$. From Eq. (4.10), we can do the following approximation [117]:

$$\frac{dw_\perp(z)}{dz} = \frac{2Z_0c}{\pi a^4}e^{-\sqrt{\frac{z}{s_2}}}. \tag{5.3}$$

Thus, we have:

$$w_\perp(\sigma_z) = \left.\frac{dw_\perp(z)}{dz}\right|_{z=0}\sigma_z = \frac{2Z_0c}{\pi a^4}\sigma_z. \tag{5.4}$$

Inserting Eq. (5.4) in (5.2) and considering $k_\beta \sim 1/\langle\beta_T\rangle$, with β the Twiss betatron function, we finally have:

$$|\Upsilon| = \frac{Z_0c}{2\pi}\frac{Ne\langle\beta\rangle\sigma_z}{a^4G}\ln\left(\frac{W_f}{W_0}\right). \tag{5.5}$$

For EuPRAXIA@SPARC_LAB, values of Υ of a few units are acceptable. For the calculation of the minimum average iris radius, we used Eq. (5.5) with the parameters of Linac1 summarized in Table 5.4 (where D means driver beam in the particle wakefield acceleration). The cases in the table are the worse in terms of beam stability. Indeed, the beta function is higher at the beginning of Linac1, the gradient is lower for the PWFA case and the bunch length is higher for the Full rf case. In both cases, it has been found that the minimum iris radius to have a maximum value of Υ equal to 2 is 3.2 mm (a/λ=0.128). This value has been used as a reference guideline in the design of the structures.

Table 5.4. EuPRAXIA@SPARC_LAB's main parameters of Linac1.

Parameter	Units	PWFA	Full rf
W_0	MeV	102	171
W_{L1}	MeV	222	502
$\langle G\rangle$	MV/m	20	57
Charge	pC	200(D)	200
σ_z	µm	50(D)	112
$\langle\beta\rangle$	m	∼30	∼30
Υ		2	2

It is worth mentioning that this is just a preliminary estimation of the minimum

average iris radius. Once defined the structure geometry, wakefields need to be calculated by means of simulation codes like ABCI [118], ECHO [119–121], Gdfidl [122, 123], CST [124]. These codes calculates the wake potential, thus, in order to obtain the wake function, the Green function needs to be found or, in a simpler way, the Bane's or other formulas for short bunches can be fitted with the simulation, slightly changing their coefficients. Once obtained the wake function, it can be used in particle tracking codes like ELEGANT [125] or GPT [126, 127] or used in analytical calculations as described in Refs. [128, 129].

5.2.3 Design of the cells

Once defined the minimum average iris radius, the design of the regular cell has been performed with ANSYS HFSS. HFSS (High Frequency Structure Simulator) [130] is a finite element method (FEM) solver for electromagnetic structures from ANSYS. It is a 3D electromagnetic simulation software for designing and simulating high-frequency electronic products such as antennas, antenna arrays, rf or microwave components, high-speed interconnects, filters, connectors, integrated circuit packages and printed circuit boards.

A sketch of the cell geometry is shown in Fig. 5.3, where a is the cell iris radius, b the outer radius, t the iris thickness, r_0 the radius of the iris roundings and r_1/r_2 is the aspect ratio of the elliptical profile of the iris. d is the cell length and, according to Eq. (2.8), for a frequency of 11.9942 GHz and the $2\pi/3$ mode, it is equal to 8.332 mm. The iris thickness t has been fixed equal to 2 mm (t/λ=0.080) as a good compromise between rf performance and breakdown rate probability.

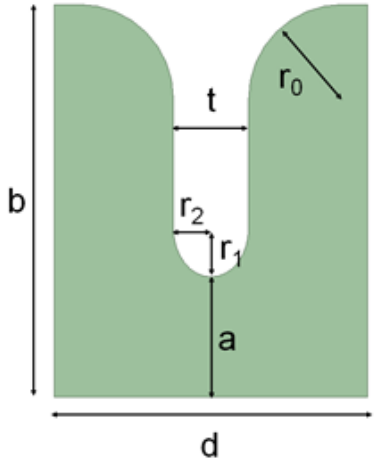

Figure 5.3. Sketch of the single cell with main parametrized dimensions.

The design aimed to minimize the modified Poynting vector normalized to the

average accelerating gradient $S_{c\,max}/E_{acc}^2$ and to calculate the other cell parameters (shunt impedance per unit length r, quality factor Q and group velocity v_g/c) as a function of the iris aperture a. An elliptical shape of the irises has been implemented in order to minimize the peak modified Poynting vector on its surface. The normalized modified Poynting vector $S_{c\,max}/E_{acc}^2$ and shunt impedance r as a function of the iris ellipticity r_1/r_2 have been calculated. The results are shown in Figs. 5.4 and 5.5. The simulated data has been fitted with third order polynomial functions. The minimum value of $S_{c\,max}/E_{acc}^2$ has been obtained for $r_1/r_2 = 1.3$. The reduction in terms of $S_{c\,max}/E_{acc}^2$ between the circular profile of the iris and the best elliptical profile is ∼6% while the reduction in term of effective shunt impedance is ∼1%. The main parameters of the reference cell are summarized in Table 5.5.

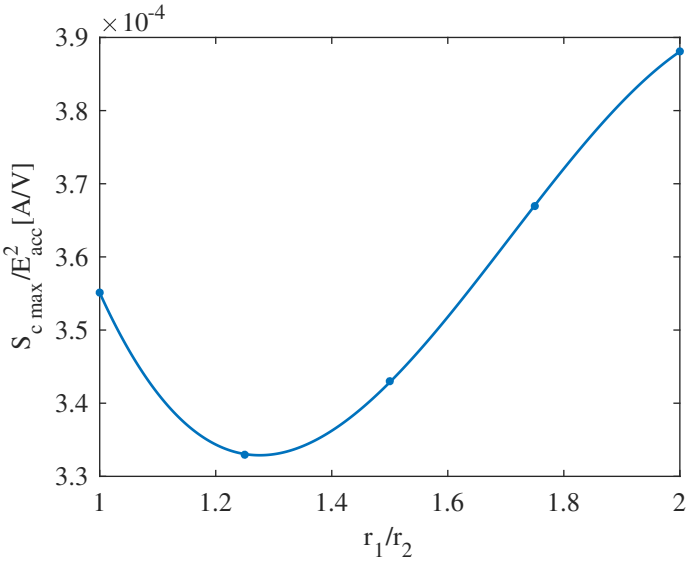

Figure 5.4. Shunt impedance of the regular cell as function of the iris ellipticity.

Table 5.5. EuPRAXIA@SPARC_LAB's main parameters of the regular cell.

Parameter	**Units**	**Value**
Iris radius a	mm	3.2
Iris thickness t	mm	2.0
Iris ellipticity r_1/r_2		1.3
Edge rounding radius r_0	mm	2.5
Outer radius b	mm	10.452
Cell length d	mm	8.332
Shunt impedance r	MΩ/m	117
Quality factor Q		7036
Geometry factor r/Q	kΩ/m	16.6
Group velocity v_g/c	%	1.77
Peak normalized modified Poynting vector $S_{c\,max}/E_{acc}^2$	A/V	3.3×10^{-4}

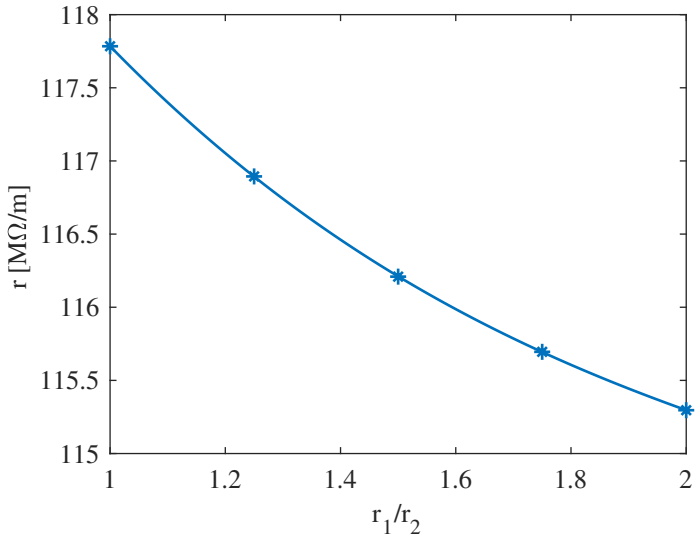

Figure 5.5. Shunt impedance of the regular cell as function of the iris ellipticity.

Once defined the optimal iris profile, the main cell parameters, as a function of the iris radius a, have then been calculated (Figs. 5.6 and 5.7). Also in this case, third order polynomial functions have been used to fit the data obtained with simulations. In the plots, it is possible to observe some properties of TW cells: the variation of the parameters is not linear with the iris radius; a small iris radius is preferable in terms of rf efficiency and breakdown probability.

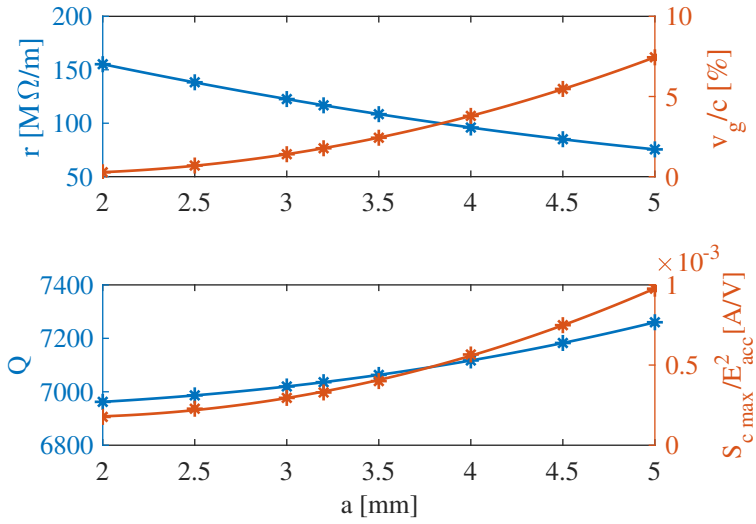

Figure 5.6. Main parameters of the regular cell as function of the iris radius a.

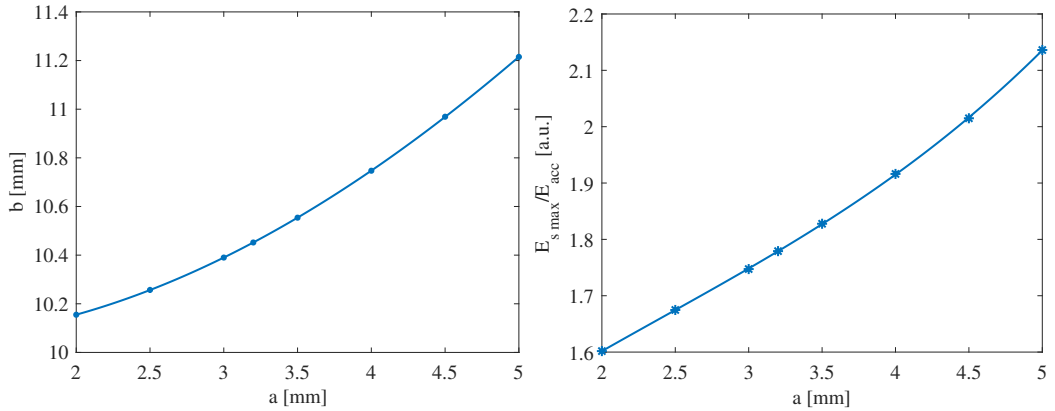

Figure 5.7. Outer radius b and peak surface electric field E_s as function of the iris radius a.

5.2.4 Analytical structure length optimization

Once defined the average iris radius of the structure, the first approach on the design has been to find the optimal structure length of constant impedance and constant gradient structures. Formulas of SLED (Section 2.5), constant impedance (Section 2.2) and constant gradient (Section 2.3) structures have been implemented in a MATLAB code.

MATLAB [131] (MATrix LABoratory) is a multi-paradigm numerical computing environment and proprietary programming language developed by MathWorks. MATLAB allows matrix manipulations, plotting of functions and data, implementation of algorithms, creation of user interfaces, and interfacing with programs written in other languages, including C, C++, C#, Java, Fortran and Python [132].

Constant impedance structure

We define

$$t' = t - t_s, \tag{5.6}$$

where $t_s = t_k - t_f$, equal to the klystron pulse subtracted by the structure filling time, is the moment in which the signal is switched by 180° for the pulse compression. With $0 \leq t' \leq t_f$, it is possible to analyze only the portion of time where the pulse is compressed and has an exponential decay (interval B in Fig. 2.4). Thus, Eq.(2.57) becomes:

$$\begin{aligned} \frac{E_{SLED}}{E_K}(t') &= \gamma e^{-\frac{t'\omega}{2Q_l}} - (\alpha - 1) \\ &= 2\frac{Q_l}{Q_e}\left(2 - e^{-\frac{t_s\omega}{2Q_l}}\right)e^{-\frac{t'\omega}{2Q_l}} - \left(2\frac{Q_l}{Q_e} - 1\right), \end{aligned} \tag{5.7}$$

where E_{SLED}/E_K is the *instantaneous electric field gain factor due to the SLED.*

For a constant impedance structure, the group velocity is constant along z. Thus, the signal time delay is

$$\tau(z) = \int_0^z \frac{dz'}{v_g(z')} = \frac{z}{v_g}. \tag{5.8}$$

Thus, we obtain

$$\begin{aligned} G(z,t') &= \sqrt{\frac{2\tau_s r P_k}{L_s}} \frac{E_{SLED}}{E_K}(t' - \tau(z)) e^{-\tau_s \frac{z}{L_s}} \\ &= \sqrt{\frac{2\tau_s r P_k}{L_s}} \left[\gamma e^{-\left(t' - \frac{z}{v_g}\right)\frac{\omega}{2Q_l}} - (\alpha - 1) \right] e^{-\tau_s \frac{z}{L_s}}, \end{aligned} \tag{5.9}$$

since

$$P_0(t) = P_k \left[\frac{E_{SLED}}{E_K}(t) \right]^2. \tag{5.10}$$

The voltage gain is the following:

$$\begin{aligned} V &= \int_0^{L_s} G(z, t' = t_f) dz \\ &= \sqrt{P_k r L_s} \sqrt{\frac{2}{\tau_s}} \left[\gamma \left(\frac{1}{\frac{Q}{Q_l} - 1} \right) \left(e^{-\tau_s} - e^{-\frac{Q}{Q_l}\tau_s} \right) + (\alpha - 1)\left(e^{-\tau_s} - 1\right) \right] \\ &= \sqrt{P_k r L_s} \sqrt{\frac{r_s}{r}}. \end{aligned} \tag{5.11}$$

Thus, we obtain the normalized effective shunt impedance:

$$\begin{aligned} \frac{r_s}{r} &= \frac{V^2}{P_k r L_s} \\ &= \left\{ \sqrt{\frac{2}{\tau_s}} \left[\gamma \left(\frac{1}{\frac{Q}{Q_l} - 1} \right) \left(e^{-\tau_s} - e^{-\frac{Q}{Q_l}\tau_s} \right) + (\alpha - 1)\left(e^{-\tau_s} - 1\right) \right] \right\}^2. \end{aligned} \tag{5.12}$$

It is possible to notice that the effective shunt impedance is a function of the section attenuation τ_s, the Q-factor of the cell Q, the unloaded Q-factor of the cavities in the SLED Q_0, the SLED external Q-factor Q_e. In our case, Q is given by the cell design and Q_0 has been set equal to 180000, as reported in Ref. [86]. Thus, r_s/r is only a function of Q_e and τ_s. The code implements the formulas above and is able to find the value of Q_e that maximise the effective shunt impedance. The contour plot of r_s/r as function of Q and Q_e is reported in Fig. 5.8, where the black line gives the optimal value of Q_e. In our case, the optimal value of Q_e has been found to be 20500.

Once found the optimal value of Q_e, it is possible to find the optimal value of τ_s

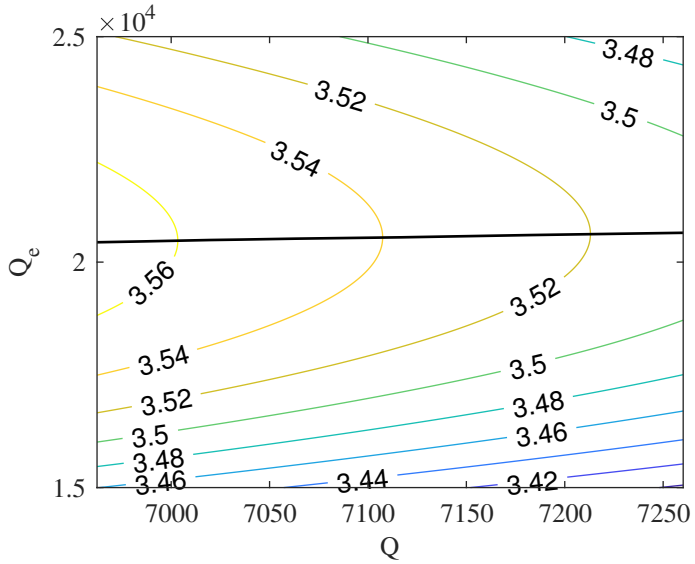

Figure 5.8. Contour plot of r_s/r as function of Q and Q_e for the constant impedance structure.

that maximise r_s/r. In our case, the value has been found to be 0.653, corresponding to an r_s of 415 MΩ/m (Fig. 5.9).

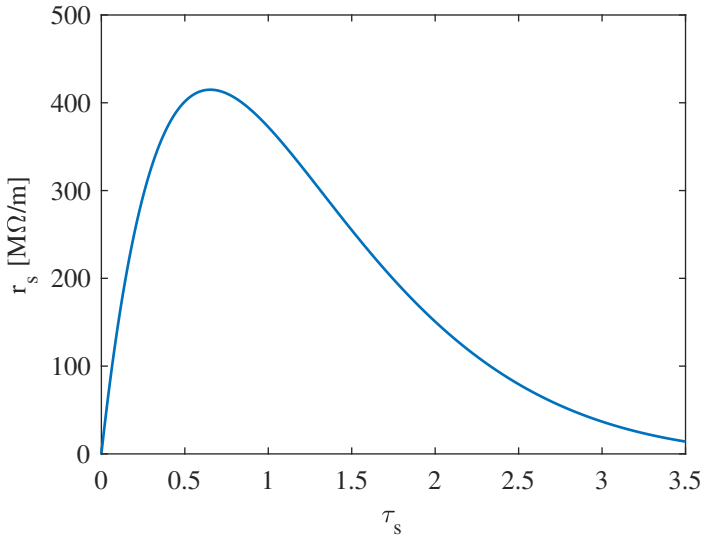

Figure 5.9. r_s as function of τ_s for the constant impedance structure.

According to the definition of τ_s in Eq. (2.33), once defined the optimal τ_s, it is possible to find the related optimal structure length L_s. In Fig. 5.10, the optimal structure length as function of the iris radius a is shown. For an iris radius of 3.2 mm the optimal structure length results to be equal to 0.674 m.

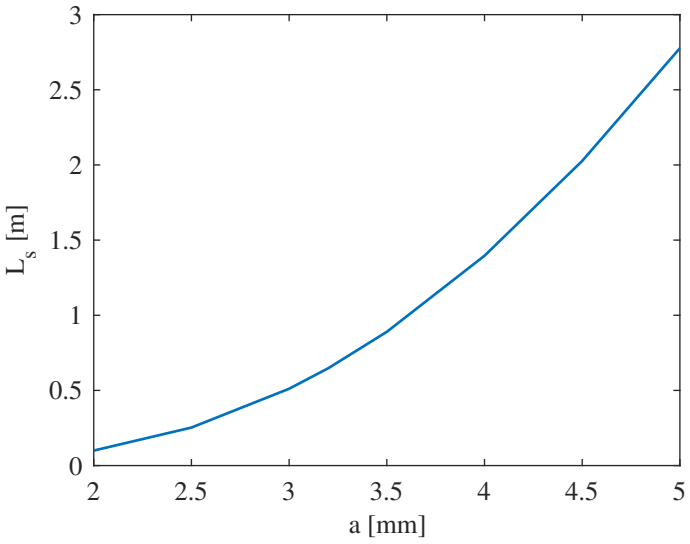

Figure 5.10. Optimal structure length L_s as function of the cell iris radius a for the constant impedance structure.

Constant gradient structure

The same exercise has been repeated for a constant gradient structure. For a CG structure, the group velocity is given by Eq. (2.40). Thus, the signal time delay is

$$\tau(z) = \int_0^z \frac{dz'}{v_g(z')} = -\frac{Q}{\omega} \ln\left[1 - \left(1 - e^{-2\tau_s}\right)\frac{z}{L_s}\right]. \tag{5.13}$$

Thus, we obtain

$$\begin{aligned} G(z,t') &= \sqrt{\frac{r}{L_s} P_k \left(1 - e^{-2\tau_s}\right)} \frac{E_{SLED}}{E_K}(t' - \tau(z)) \\ &= \sqrt{\frac{r}{L_s} P_k \left(1 - e^{-2\tau_s}\right)} \left\{ \gamma e^{-\frac{t'\omega}{2Q_l}} \left[1 - \left(1 - e^{-2\tau_s}\right)\frac{z}{L_s}\right]^{-\frac{Q}{2Q_l}} - (\alpha - 1) \right\}. \end{aligned} \tag{5.14}$$

The accelerating voltage is the following:

$$\begin{aligned} V &= \int_0^{L_s} G(z, t' = t_f) dz \\ &= \sqrt{P_k r L_s \left(1 - e^{-2\tau_s}\right)} \left\{ \gamma e^{-\frac{Q}{Q_l}\tau_s} \left[\frac{1 - \left(e^{-2\tau_s}\right)^{\left(1 - \frac{Q}{2Q_l}\right)}}{\left(1 - \frac{Q}{2Q_l}\right)\left(1 - e^{-2\tau_s}\right)} \right] - (\alpha - 1) \right\} \\ &= \sqrt{P_k r L_s}\sqrt{\frac{r_s}{r}}. \end{aligned} \tag{5.15}$$

Thus, we obtain the normalized effective shunt impedance:

$$\frac{r_s}{r} = \frac{V^2}{P_k r L_s} = \left(1 - e^{-2\tau_s}\right) \left\{ \gamma e^{-\frac{Q}{Q_l}\tau_s} \left[\frac{1 - \left(e^{-2\tau_s}\right)^{\left(1-\frac{Q}{2Q_l}\right)}}{\left(1 - \frac{Q}{2Q_l}\right)\left(1 - e^{-2\tau_s}\right)} \right] - (\alpha - 1) \right\}^2 . \tag{5.16}$$

The contour plot of r_s/r as function of Q and Q_e is reported in Fig. 5.11, the black line gives the optimal value of Q_e. The optimal value of Q_e has been found to be 22100.

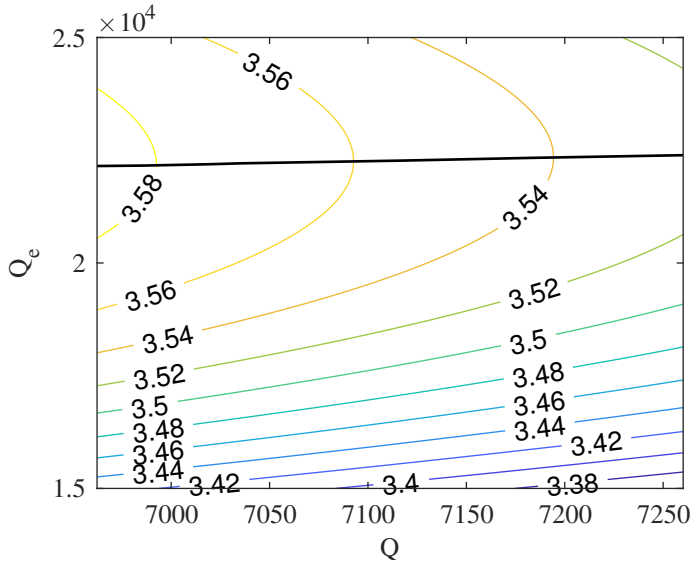

Figure 5.11. Contour plot of r_s/r as function of Q and Q_e for the constant gradient structure.

Once found the optimal value of Q_e, it is possible to find the optimal value of τ_s that maximise r_s/r. In our case the value has been found to be 0.692, corresponding to an r_s of 417 MΩ/m (Fig. 5.12).

In Fig. 5.13, the optimal structure length as function of the average iris radius $\langle a \rangle$ is shown. For an average iris radius of 3.2 mm the optimal structure length results to be equal to 0.594 m.

Comparison of the results

In Figs. 5.14 and 5.15, a comparison between CI and CG structures is shown. Main parameters are summarized in Table 5.6. It is possible to observe that CG structures have slightly better performance and require shorter structures. In addition, the accelerating gradient distributions along the structure are completely different: linear

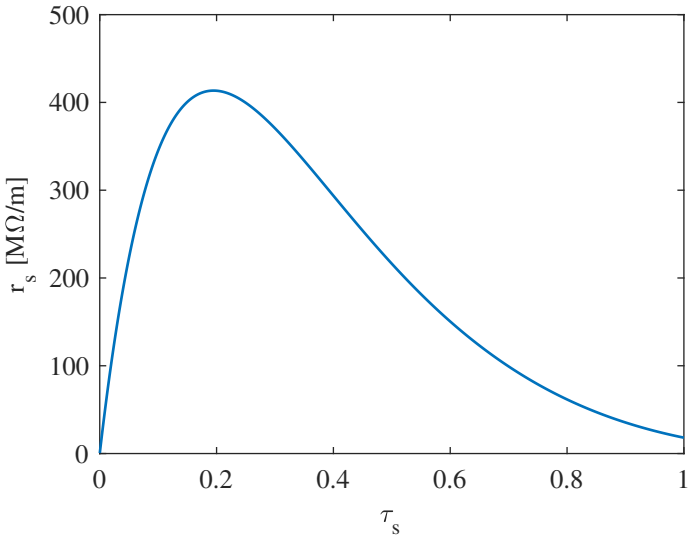

Figure 5.12. r_s as function of τ_s for the constant gradient structure.

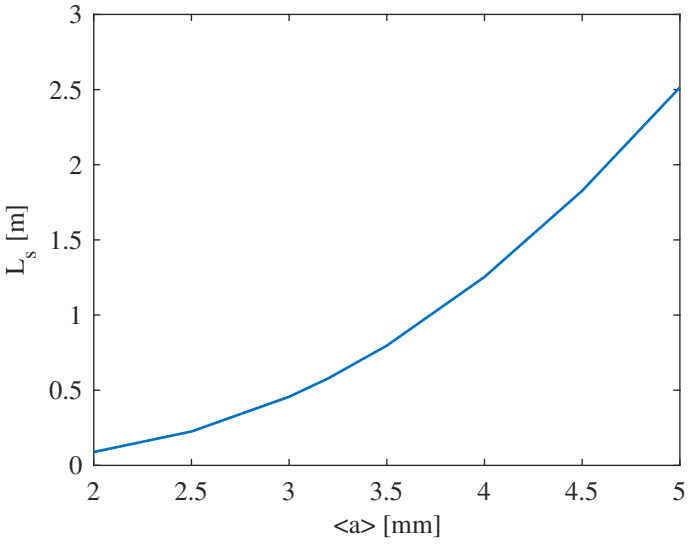

Figure 5.13. Optimal structure length L_s as function of the cell iris radius a for the constant impedance structure.

profile for the CI structure with peak value at beginning of it, non-linear profile with peak value at the end for the CG structure. Thus, as already mentioned, a CG structure with a non-flat pulse in input does not give a constant gradient profile.

The data obtained in this analytical optimization has been used as a guideline for a numerical optimization described in the following section.

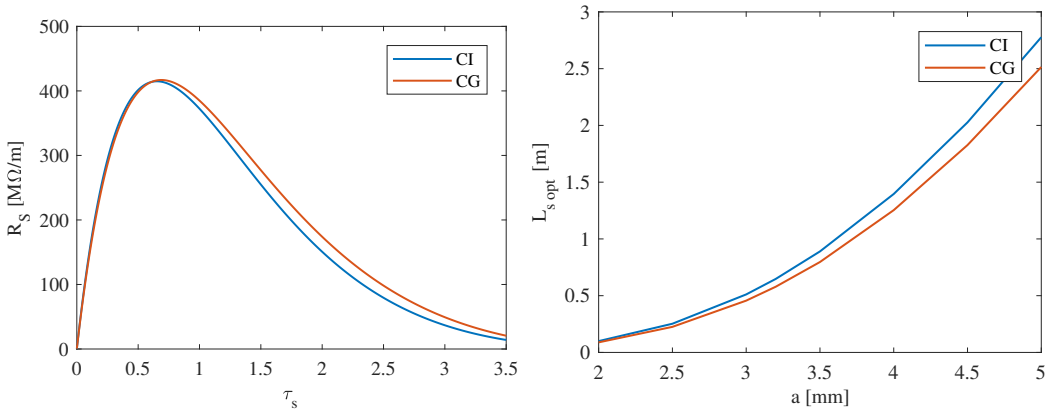

Figure 5.14. Comparison between constant impedance and constant gradient structures.

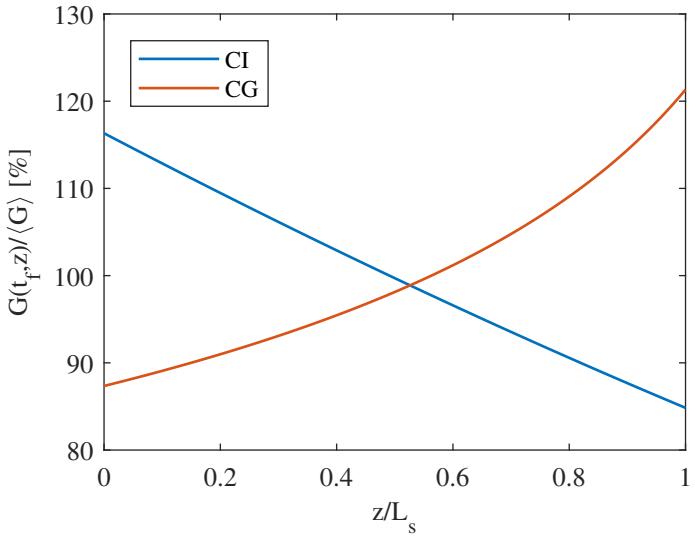

Figure 5.15. Normalized accelerating gradient after one filling time as a function of the normalized position along the structure for constant impedance and constant gradient structures.

Table 5.6. Comparison of the main parameters between constant impedance and constant gradient structures.

Parameter	Units	CI	CG
r_s	MΩ/m	415	417
τ_s		0.653	0.692
L_s	m	0.674	0.594
Q_e		20500	22100

5.2.5 Numerical effective shunt impedance optimization

As described in Section 2.3, the analytical solution of a constant gradient is based on the approximation of r and Q constant along the propagation axis z. In addition,

the electric field profile of a CG structure with pulses that are non flat (e.g. with a SLED) is not constant (see Subsection 5.2.4). Furthermore, CG analytical formulas allow to find the optimal structure length once the iris tapering is fixed but, if there are constraints in terms of available space (like in EuPRAXIA@SPARC_LAB), it could be useful to have a tool that is able to calculate the optimal iris tapering once fixed the structure length. Thus, taking into account the previous considerations, a MATLAB code that is able to calculate all the main structure parameters, once fixed structure length and iris tapering, has been written. The tool does not do any approximation and directly applies to the general main formula of the gradient in a structure (Eq. (2.46)) the data obtained with the scan of the cell parameters as a function of the iris radius (see Subsection 5.2.3). Indeed, once defined the structure length (i.e. the number of cells) and the cell-by-cell irises tapering, the geometry of each cell is known (i.e. the iris radius a and outer radius b) by using the plot in Fig. 5.7.

Linear cell-by-cell irises tapering

The first step is to define a cell-by-cell irises tapering. For the sake of simplicity, we opted for a linear tapering but the code can work with any kind of profile. In Fig. 5.16, it is shown a sketch of the irises profile for a 10 cells structure. L_s is the structure length and θ is the tapering angle. Fixed the average iris radius $\langle a \rangle$ equal

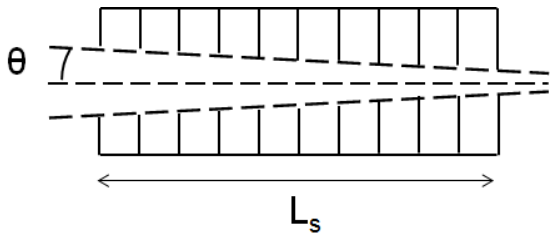

Figure 5.16. Sketch of the linear tapering of the irises in a 10 cells structure.

to 3.2 mm, it is easy to find the value of a as function of z according to

$$a(z) = \langle a \rangle + \left(\frac{L_s}{2} - z \right) \tan(\theta). \tag{5.17}$$

Since in real disks the iris is located in the middle of the cell, we obtain the iris radii of the first and the last cells as the following:

$$a_1(z) = \langle a \rangle + \left(\frac{L_s}{2} - \frac{d}{2} \right) \tan(\theta), \tag{5.18}$$

$$a_N(z) = \langle a \rangle - \left(\frac{L_s}{2} - \frac{d}{2} \right) \tan(\theta), \tag{5.19}$$

where d is the cell length. In Fig. 5.17, the plot of a as a function of z for different values of θ is shown. The range of variation of the tapering angle is between 0° and 0.2°, since the corresponding equivalent tapering angle of the CG structure has been found to be ∼0.1°, while L_s is equal to 0.5 m (60 cells). The same kind of plots has been obtained for the other cell parameters b, r, Q, r/Q, v_g/c and $S_{c\,max}/E_{acc}^2$. They are reported in Figs. 5.18, 5.19 and 5.20.

Optimization for three different rf module configurations

Half meter long structures allow to put 32 structures in 16 m of active length. With 32 structures we can have 4 rf modules with 8 structures each or 8 rf modules of 4 structures each. Having a number of structures per module that can be expressed as power of 2 is preferable since it is possible to design simple binary tree waveguide networks using only 3 dB splitters. Other structure lengths that allow to do this are: 0.667 m (80 cells) and 0.4 m (48 cells). In the first case, it is possible to have 3 rf modules with 8 structures each, while in the second one, it is possible to have 5 rf modules with 8 structures each.

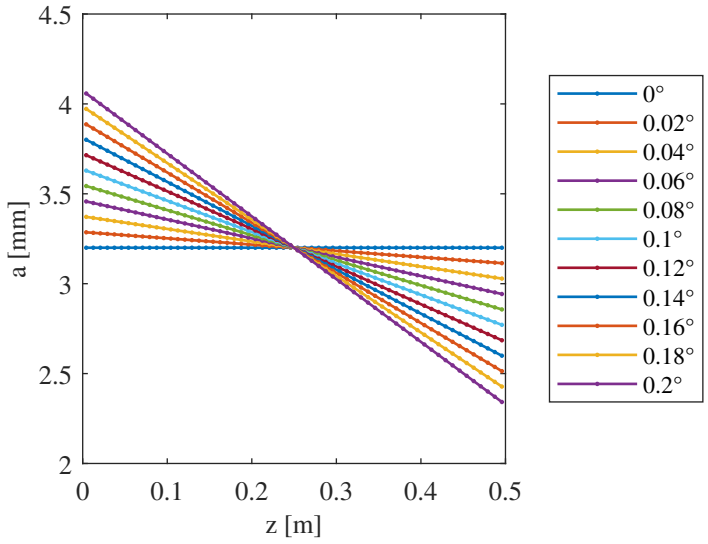

Figure 5.17. a as a function of z for different values of θ with L_s=0.5 m (60 cells).

Eqs. (2.15), (5.10) and (2.16) have also been implemented in the tool. Thus, plots of $G_0(z, t_f)$ normalized to the fraction of klystron power delivered to the structure and $g(z)$ as a function of the position along the structure can be produced. As shown in Fig. 5.21, $G_0/\sqrt{P_0}$ becomes smaller increasing the tapering angle since the iris radius of the first cell becomes higher, while g has different slopes depending on the tapering angle.

Combining Eqs. (2.44) and (5.6), we obtain the gradient distribution at the

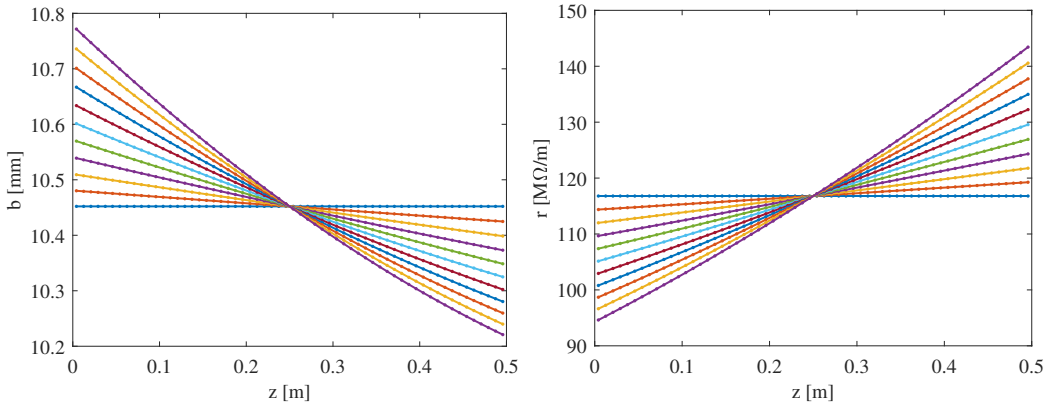

Figure 5.18. Outer radius b and shunt impedance r as a function of z for different values of θ with L_s=0.5 m (60 cells).

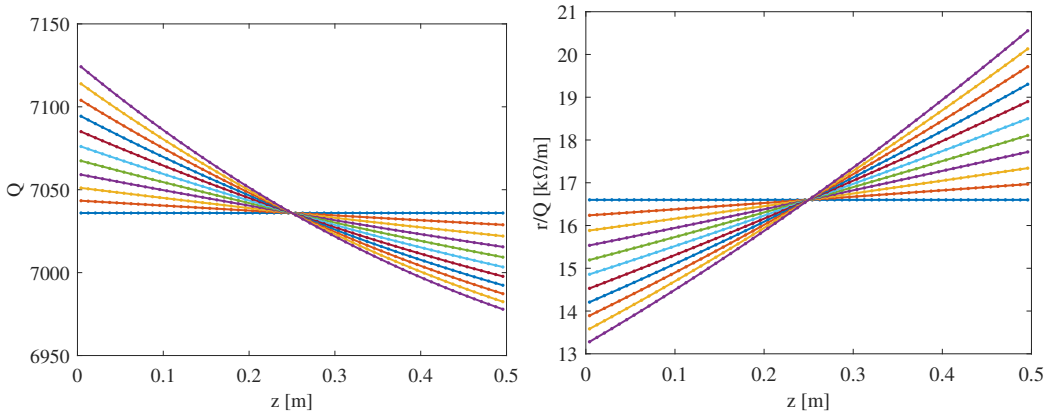

Figure 5.19. Q-factor Q and geometry factor r/Q as a function of z for different values of θ with L_s=0.5 m (60 cells).

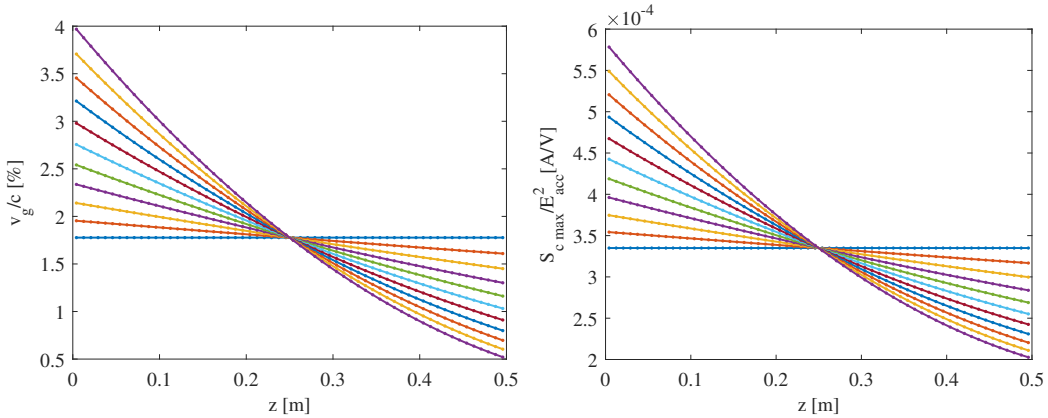

Figure 5.20. Normalized group velocity v_g/c and normalized modified Poynting vector $S_{c\,max}/E_{acc}^2$ as a function of z for different values of θ with L_s=0.5 m (60 cells).

moment of the injection $t' = t_f$:

$$G(z, t_f) = G_0[t_f - \tau(z)]g(z). \tag{5.20}$$

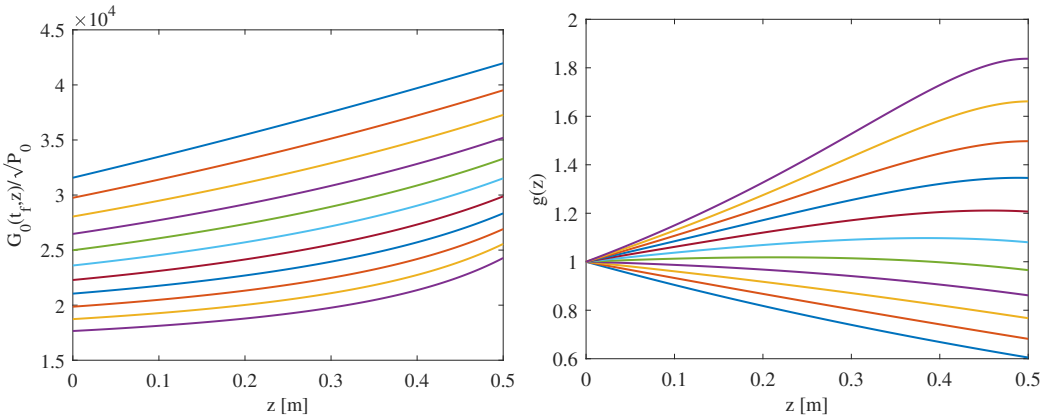

Figure 5.21. $G_0(z, t_f)$ normalized to the fraction of klystron power delivered to the structure and $g(z)$ as a function of z for different values of θ with L_s=0.5 m (60 cells).

Its plot is shown in Fig. 5.22 (Ultimate case, average gradient of 80 MV/m), where, for every tapering angle, the optimum value of the SLED's external Q-factor Q_e has been found. It is possible to observe that, for θ =0°, we obtain the same gradient profile of the constant impedance structure calculated with analytical formulas. For θ =0.04° we have a quasi-constant gradient profile.

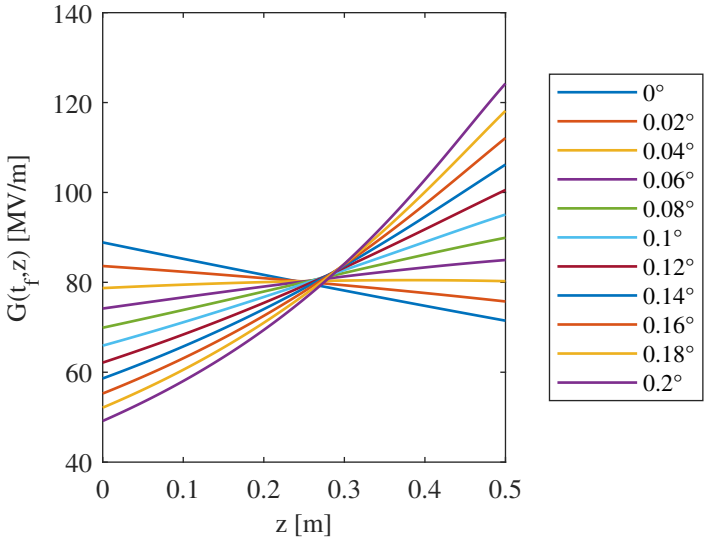

Figure 5.22. Accelerating gradient after one filling time as a function of z for different values of θ with L_s=0.5 m (60 cells).

Once the gradient profile is known, it is possible to obtain the the effective shunt impedance and then, the *fraction of klystron power per structure* P_{ks}. Results are shown in Fig. 5.23. The best result in terms of efficiency is obtained for θ =0.18°, a quite pronounced tapering. In terms of efficiency, the benefit from the tapering is limited since, with respect to the constant impedance case, the maximum gain is

only 2.5% higher.

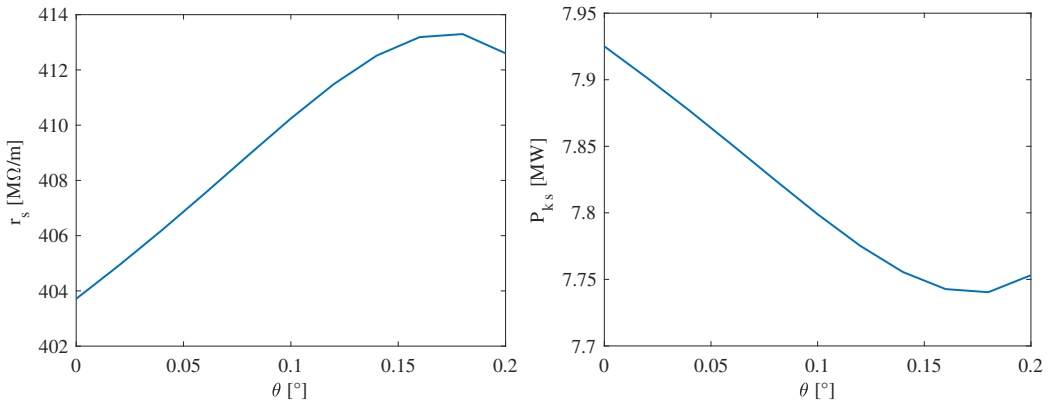

Figure 5.23. Effective shunt impedance and fraction of klystron power per structure as a function of the tapering angle for L_s=0.5 m (60 cells).

The behavior of the modified Poynting vector along the structure has been calculated multiplying the normalized modified Poynting vector computed with HFSS by the square of the peak value of the rf pulse in the structure. It has been done for every tapering angle and results are shown in Fig. 5.24. The profile of modified Poynting vector for the quasi-constant gradient structure is not constant. With the plot of Fig. 5.24, it is possible to find the peak value of modified Poynting

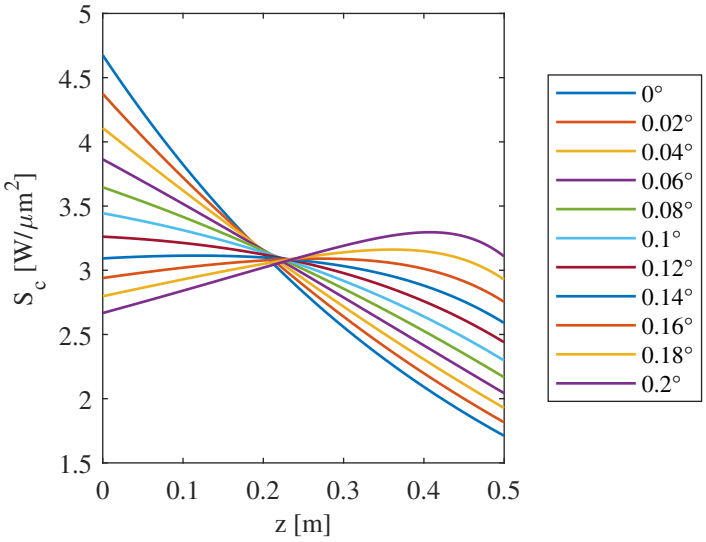

Figure 5.24. Modified Poynting vector as a function of z for different values of θ with L_s=0.5 m (60 cells).

vector along the structure for every slope. The result is reported if Fig. 5.25, where the scaled limit, according to Eq. (3.14), is shown. It has been considered a limit value of $4\,\mathrm{W/\mu m^2}$ with a breakdown rate of 1×10^{-6} bpp/m and it has been scaled, depending on the filling time, according to Eq. (3.14). The same plot can be shown

in a more convenient way, considering the difference between the value and the fixed limit expressed in %. The plot is shown in Fig. 5.25. The tapering angle that gives the lowest breakdown rate probability is 0.14°. With respect to the efficiency, the benefit of the tapering in terms of breakdown probability is bigger. Indeed, in the best case, peak value of modified Poynting vector is ∼35% smaller than the fixed limit while, in the worst case (constant impedance structure), it is ∼10% smaller. In any case, for every tapering angle, the modified Poynting vector is always below the limit.

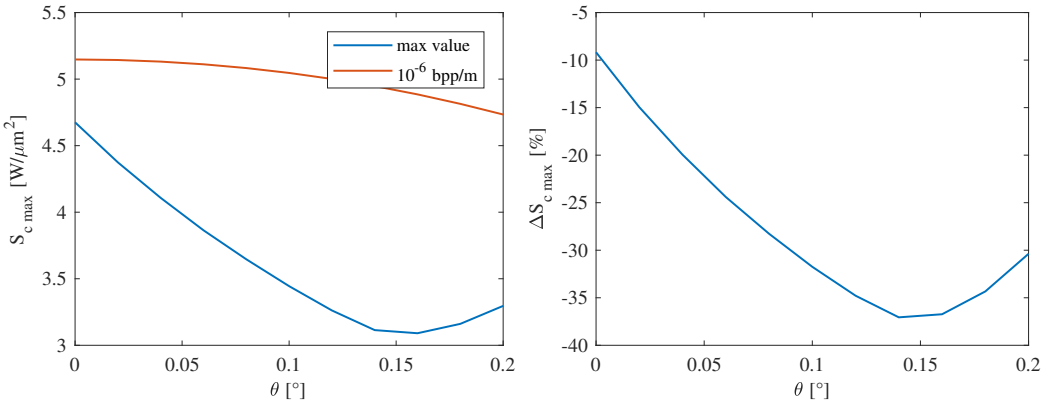

Figure 5.25. Peak value of modified Poynting vector as a function of the tapering angle for L_s=0.5 m (60 cells).

With the same kind of approach, the peak surface electric field in the structure has been calculated for different tapering angles. It has been considered a limit value of 220 MV/m with a breakdown rate of 1×10^{-6} bpp/m and it has been scaled, depending on the filling time, according to Eq (3.8). Results are shown in Fig. 5.26, where it is possible to observe that the minimum value of E_s is ∼170 MV/m for an angle of 0.1° and that, in any case, the surface electric field never exceeds the scaled limit for every angle.

The same calculations have been repeated for the other two mentioned structure lengths: 0.667 m (80 cells) and 0.4 m (48 cells). A comparison of the results for these three options are shown in Fig. 5.27. The best solution in terms of efficiency is the longest one, while, in terms of breakdown probability, the best solution is the shortest one. It can be noticed that the longest solution exceeds the fixed breakdown limit for some values of the tapering angle. As a good compromise between efficiency, breakdown probability, beam breakup instabilities and modularity, we opted for a 0.5 m structure with a tapering angle of 0.1° as a design guideline.

Concerning the transverse beam instabilities, preliminary beam dynamics simulations have been performed with the code ELEGANT, using Bane's wake functions, for a half meter long constant impedance structure [110]. Results satisfy the require-

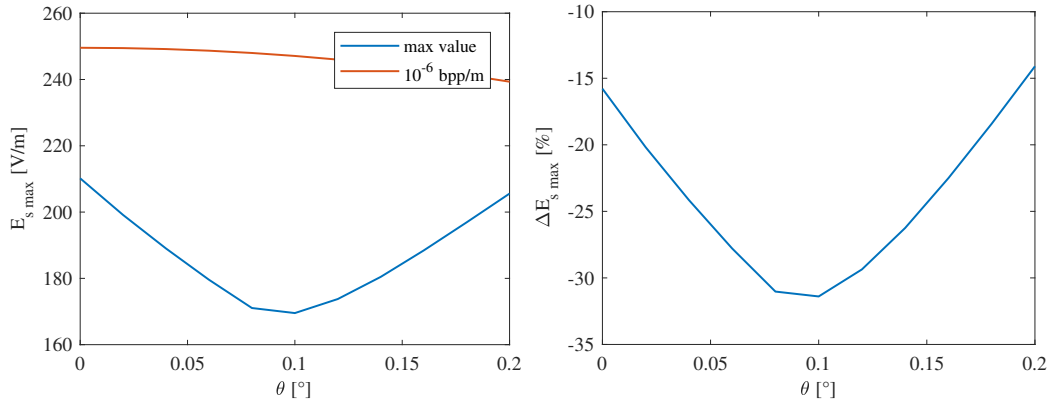

Figure 5.26. Peak value of surface electric field as a function of the tapering angle for L_s=0.5 m (60 cells).

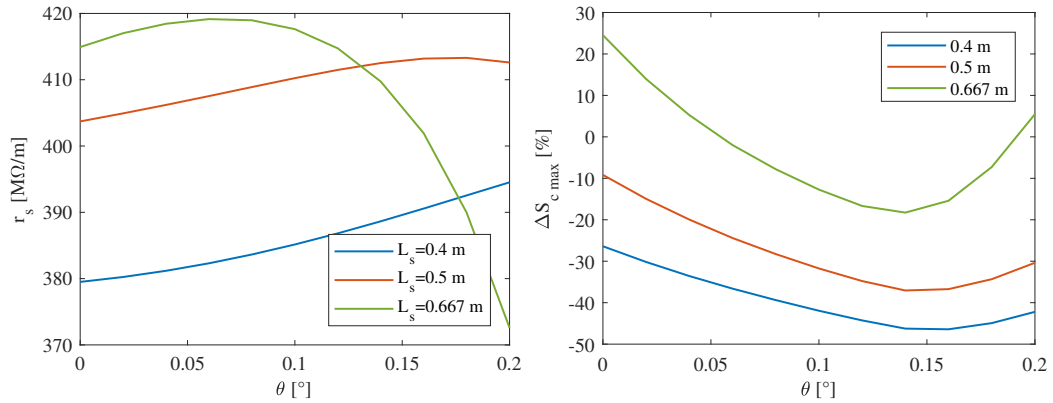

Figure 5.27. Effective shunt impedance and peak value of modified Poynting vector as a function of the tapering angle for three different structure lengths.

ments of the beam quality at linac exit.

Parameters of the linac

The main parameters of the X-band linac, obtained with the numerical tool, are reported in Table 5.7. It has been considered a very conservative total power attenuation of 20% from the klystron to the section input, which gives an available klystron power of ∼40 MW. The total number of klystrons is 4 for the Full rf case and 8 for the Ultimate case. The peak structure input power is 30 and 58 MW, respectively. The optimal external Q-factor of the SLED is 19300.

5.2.6 Layout of the rf module

In Fig. 5.28, a sketch of the rf module is shown. It is made up of a group of 8 TW sections assembled on a single girder and fed by one (for Full rf) or two (for Ultimate) klystrons by means of one pulse compressor system and a waveguide network that

Table 5.7. Main parameters of the EuPRAXIA@SPARC_LAB's X-band linac.

Parameter	**Units**	**Value**	
Available klystron power	MW	∼40	
Klystron pulse length	µs	1.5	
SLED Q_0		180000	
SLED Q_e		19300	
Total active length L_t	m	16	
Number of structures N_s		32	
Number of structures per module N_{sm}		8	
Number of modules N_m		4	
Structure length L_s	m	0.5	
Number of cells N_c		60	
Iris radius first-last cell a	mm	3.629 - 2.771	
Normalized group velocity v_g/c	%	2.76 - 1.03	
Filling time t_f	ns	100	
Section attenuation τ_s		0.534	
Shunt impedance r	MΩ/m	105-130	
Q-factor Q		7076-7003	
r/Q	kΩ/m	14.9-18.9	
Effective shunt impedance r_s	MΩ/m	410	
P_{out}/P_{in}		0.34	
		Full rf	**Ultimate**
Average gradient $\langle G \rangle$	MV/m	57	80
Energy gain W_{gain}	MeV	912	1280
Peak input power	MW	30	58
Input power averaged over the pulse	MW	21	42
Total klystron power	MW	127	250
Total number of klystrons		4	8

transports the rf power to the input couplers of the sections. A circular overmoded waveguide allows to strongly reduce the loss due to the connection between the modulator and linac halls. A preliminary 3D mechanical model of the rf module has been realized with the commercial CAD code Autodesk Inventor [133] and it is illustrated in Fig. 5.29. Due to the compactness of the module, the power attenuation of the waveguide distribution network (including the overmoded waveguide) has been estimated to be ∼11%.

5.2.7 Vacuum system

Concerning the vacuum system, a preliminary design has been performed [134]. Ultra high vacuum in waveguides and accelerating structures is guaranteed by the use of SAES NEXTorr NEG (Non-Evaporable Getter) - ion combined pumps [135]. As shown in Fig. 5.29, these pumps are connected to the beginning and end of the

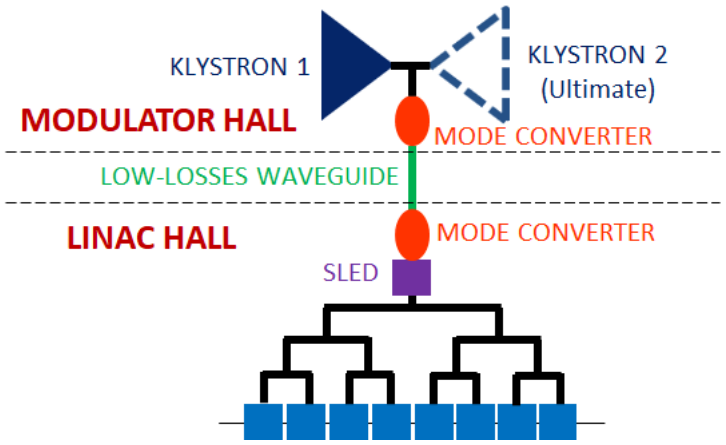

Figure 5.28. Sketch of the EuPRAXIA@SPARC_LAB's rf module.

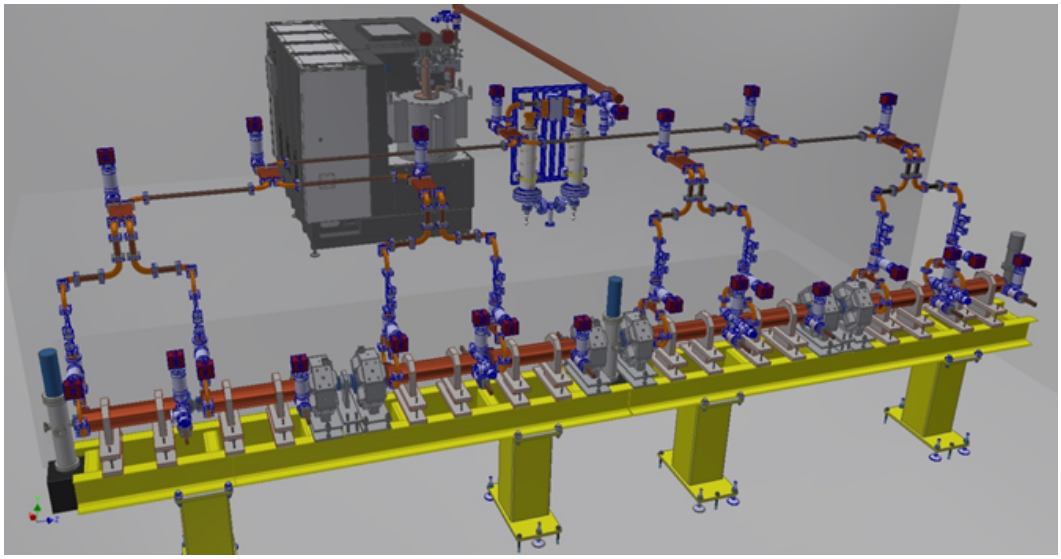

Figure 5.29. 3D model of the EuPRAXIA@SPARC_LAB's X-band linac.

overmoded circular waveguide and the accelerating sections, and to one port of the 3 dB hybrids. Details of the vacuum system are shown in Figs. 5.30 and 5.31.

Vacuum simulations have been performed by the vacuum group at LNF, assuming a surface specific outgassing rate of 10^{-11} mbar L s^{-1} cm^{-2}. Results are shown in Figs. 5.32, 5.33 and 5.34 [136]. The overmoded circular waveguide has a diameter of 40 mm and is 4 m long. The pumping system gives a peak pressure of $\sim 1.7 \times 10^{-8}$ mbar in the middle of the waveguide. The longest branch of the binary tree power distribution system is ~1.65 m long. The peak pressure in the middle of the WR-90 waveguide is $\sim 1.4 \times 10^{-8}$ mbar, while in the middle of the structure is $\sim 3.1 \times 10^{-8}$ mbar.

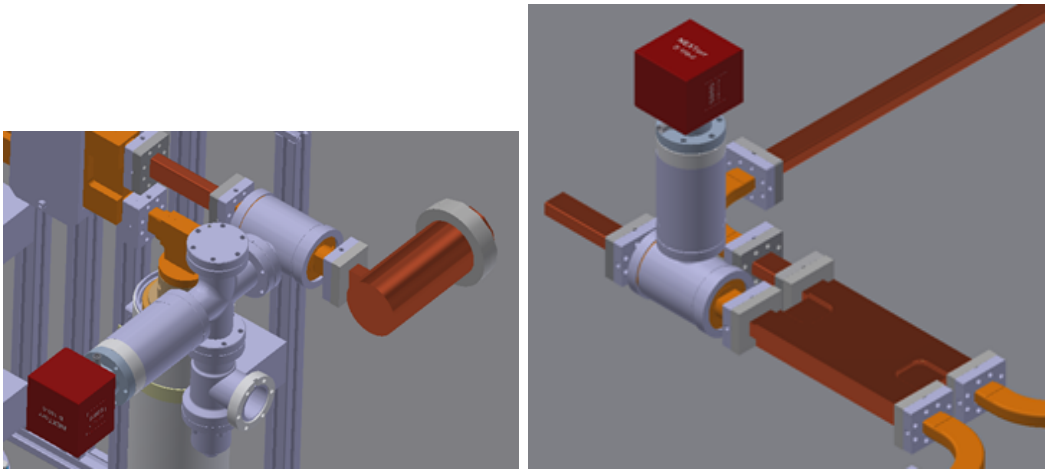

Figure 5.30. Detail of the vacuum system: circular overmoded waveguide (left) and WR-90 waveguides (right).

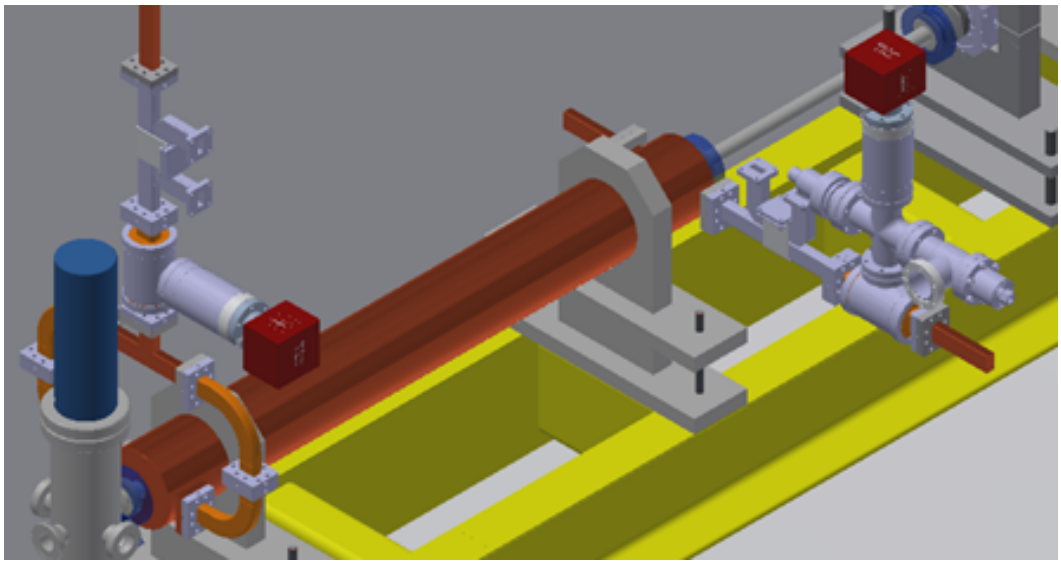

Figure 5.31. Detail of the vacuum system: X-band structure.

5.2.8 Structure sensitivity to mechanical errors

The frequency and phase advance per cell sensitivities, with respect to the cell main geometrical parameters, have been calculated for the first and last cell. With 3D EM codes it is possible to find the resonance frequency shift due to a mechanical error in the cell. But we are interested in finding the phase advance per cell error at the nominal rf frequency. For a mechanical error that does not involve the cell length d, the dispersion curve is vertically shifted of a quantity Δ_f. It can be easily

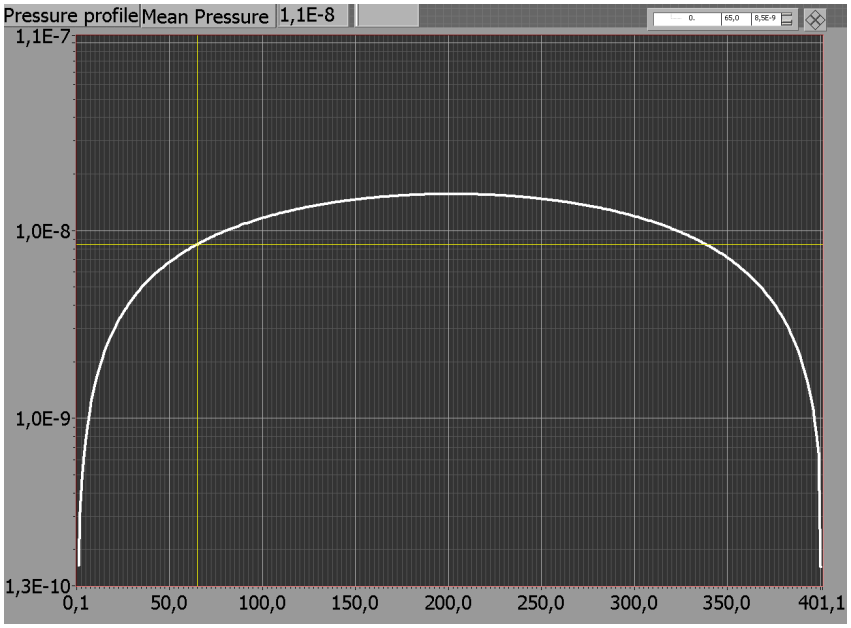

Figure 5.32. Pressure profile along the circular overmoded waveguide.

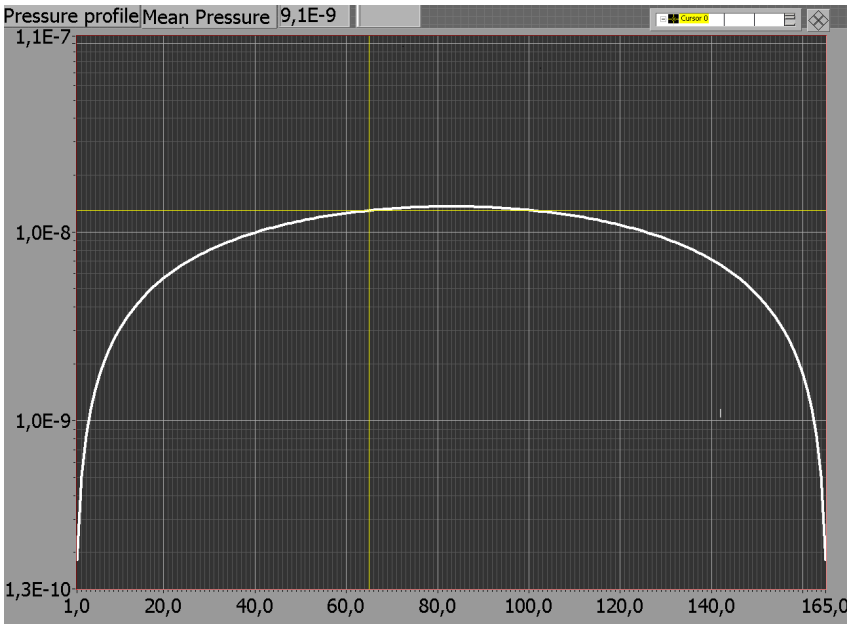

Figure 5.33. Pressure profile along the rectangular waveguide (longest branch).

obtained with the following formula:

$$\Delta\phi_{a,b,t} = -\frac{2\pi d}{v_g}\Delta f_{a,b,t}, \tag{5.21}$$

where $\Delta\phi_{a,b,t}$ is the error in the phase advance per cell introduced by an error in the dimension of the cell parameters a, b and t, $\Delta f_{a,b,t}$ is the correspondent frequency

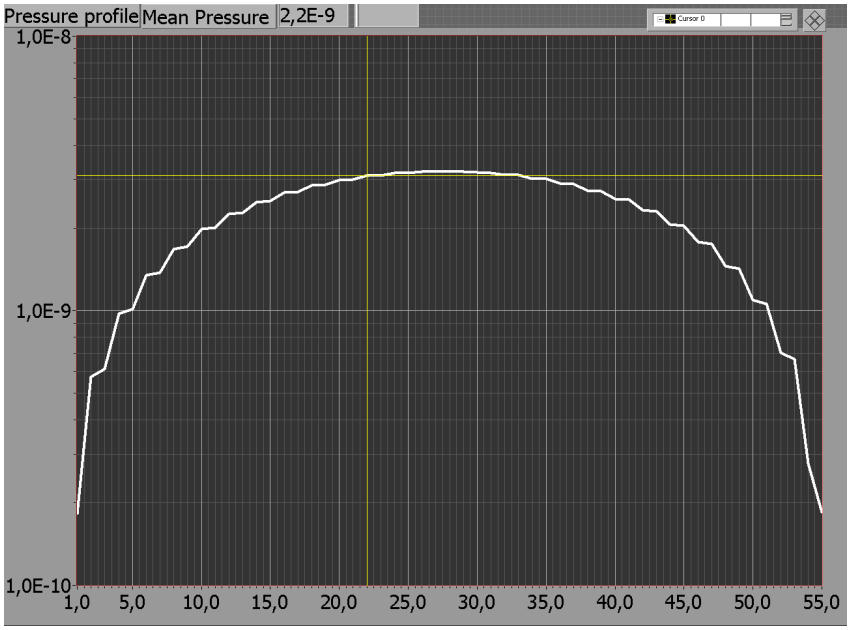

Figure 5.34. Pressure profile along the X-band structure.

error computed with the code keeping the nominal phase advance per cell, d is the nominal cell length and v_g is the nominal group velocity of the cell. For a mechanical error Δd that involves the cell length d, Eq. (5.21) needs an additional term due to the contraction of the new dispersion curve:

$$\Delta\phi_d = -\frac{2\pi d}{v_g}\Delta f_d - \frac{2\pi f_{rf}}{c}\Delta d, \tag{5.22}$$

where f_{rf} is the nominal rf frequency and c is the speed of light.

Results of the calculations are shown in Table 5.8. The shifts of resonance frequency and phase advance per cell are more affected by mechanical errors involving the outer radius of the cell b. The phase advance per cell is more sensible to mechanical errors in the last cells because of their lower group velocity.

Table 5.8. Frequency (df/dx) and phase advance per cell ($d\phi/dx$) sensitivities with respect to the cell main geometrical parameters for the first and last cell.

Parameter	**First cell**		**Last cell**	
	df/dx [kHz/µm]	$d\phi/dx$ [deg/µm]	df/dx [kHz/µm]	$d\phi/dx$ [deg/µm]
Outer radius b	-1300	0.471	-1280	1.243
Iris radius a	483	-0.175	344	-0.334
Iris thickness t	262	-0.095	225	-0.219
Length d	-193	0.070	-148	0.144

In Ref. [137], a statistical evaluation of the tuning efficiency has been performed to determine the required phase advance per cell of the ELI-NP C-Band damped TW accelerating structures [138]. It has been found that, with a uniform phase advance per cell error distribution with a maximum deviation $\Delta\phi < \pm 2°$ and a maximum cumulative phase advance error $\sum \Delta\phi < 5°$, the reduction in terms of accelerating gradient is below 0.5%.

These results have been used to determine the mechanical tolerances of the structure. Considering a maximum error in the phase advance per cell of 2°, the results are reported in Table 5.9. Tolerances lower than 2 µm seem required for the last cells due to the sensitivity to errors involving the outer radius. Since the actual state of the art in terms of mechanical precision of fabrication is 2 µm, the presence of tuners in the the cells appears necessary. It is worth mentioning that tuning of the average phase velocity can be also performed changing the water temperature of the cooling system.

Table 5.9. Requirements in terms of mechanical tolerances with respect to the cell main geometrical parameters for the first and last cell.

Parameter	**Units**	**Mechanical tolerances**	
		First cell	**Last cell**
Outer radius b	µm	±4.244	±1.609
Iris radius a	µm	±11.423	±5.985
Iris thickness t	µm	±21.058	±9.151
Length d	µm	±28.589	±13.912

5.2.9 Design of the rf power couplers

As described in Sections 2.7 and 3.3, the design of rf couplers has a crucial role in the design of a structure.

As a first approach, we opted for a slot coupler because of its compactness. Design geometrical parameters are the radii r_1 and r_2 of the roundings between the waveguide and the slot and between the slot and the matching cell, respectively. These two radii give a geometry called *z-coupling* (Fig. 5.35), a solution successfully adopted at SLAC for the LCLS rf Gun [139]. Increasing the curvature of the coupler slot allows to reduce the surface magnetic field and then the pulsed heating.

The technique used to design and tuning the coupler is the one adopted at CERN (CLIC group) for the design of many structures [140]. It is based on drawing a small structure of a few cells with couplers of the same dimensions and adjusting the *coupler cell radius* R_c and the *slot width* w in order to obtain a small value of the magnitude of S_{11}. The structure needs to be symmetric with respect to the

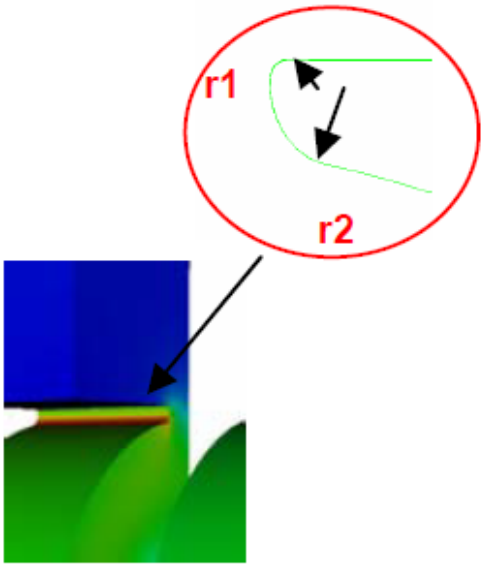

Figure 5.35. Z-coupling [139].

transverse plane, thus the input and output couplers are designed separately. Due to the required symmetry, the cells can be all equal or with the designed structure tapering until the middle of the structure, where it is mirrored. For the sake of simplicity, we opted for all equal cells. The magnitude of S_{11} has been calculated for three structures having respectively 3, 4 and 5 cells. The highest value is assumed as the coupler value. The goal is then to tune R_c and w in order to obtain a value of $|S_{11}|$ below -30 dB for all the three structures. This can be easily performed using the optimizer tool integrated in the HFSS software. This tool allows to automatically optimize defined parameters by changing input variables. In order to not have problems with the tool when the number of cells changes, the conductivity is imposed as ideal (perfect E). Once found the optimal values of R_c and w, the value of $|S_{11}|$ is computed again imposing the conductivity of copper for a 7 cells structure. An example of the 3D model of a 7 cells structure is shown in Fig. 5.36. Due to symmetry considerations, it is sufficient to simulate only one quarter of the structure imposing perfect H boundary conditions on the horizontal and longitudinal planes.

Another goal is to keep the pulsed heating below 50 °C in order to avoid breakdown phenomena. To do this, the radius r_2 has been fixed equal to 4 mm, while r_1 is 2 mm, for both the input and output couplers.

The last goal is to strongly minimize the quadrupolar field component of the

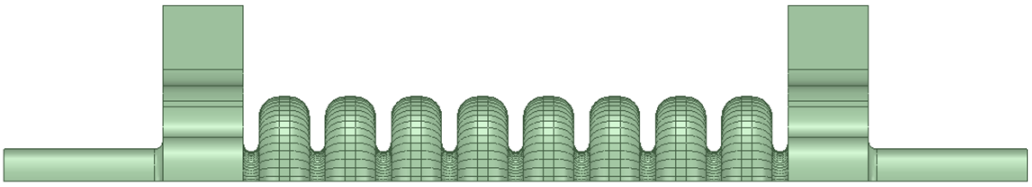

Figure 5.36. 3D model of a 7 cells structure for tuning of an rf coupler.

magnetic field. To do this, a racetrack geometry has been implemented in the design.

In Fig. 5.37, the geometry of the input coupler is shown, where Δx is the distance from the center of the coupler where the centers of the semicircles are placed. In Table 5.10, the main geometrical parameters of input and output couplers are reported.

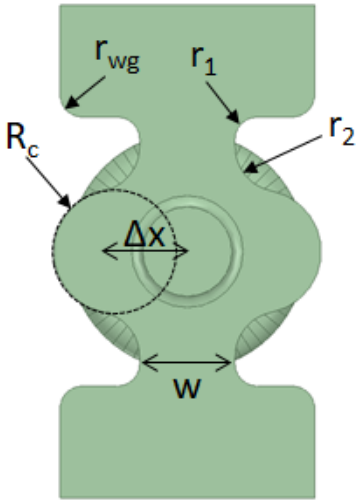

Figure 5.37. Geometry of the EuPRAXIA@SPARC_LAB's rf power input coupler.

Table 5.10. Main geometrical parameters of the EuPRAXIA@SPARC_LAB's rf power couplers.

Parameter	Units	Input coupler	Output coupler
Waveguide rounding r_{wg}	mm	2	
Waveguide-slot rounding r_1	mm	2	
Slot-matching cell rounding r_2	mm	4	
Matching cell radius R_c	mm	5.524	6.325
Off-axis circle center Δx	mm	6.5	4.75
Slot width w	mm	8.545	7.801

The obtained reflection coefficient at the the input port is -42 dB for the input coupler and -33 dB for the output one. In the input coupler, the maximum value of the surface magnetic field is 419.5 kA/m, with an input peak power of 58 MW of

Table 5.7 (Ultimate case). In reality, the power has been divided by 4 since only one quarter of the structure has been simulated. In Fig. 5.38, it is shown the magnitude of the surface H field obtained with HFSS. By using Eq. (3.10) and considering that the filling time is 100 ns, we obtain a pulsed heating of 25 °C. This value can be considered absolutely safe in terms of breakdown rate and damages probabilities.

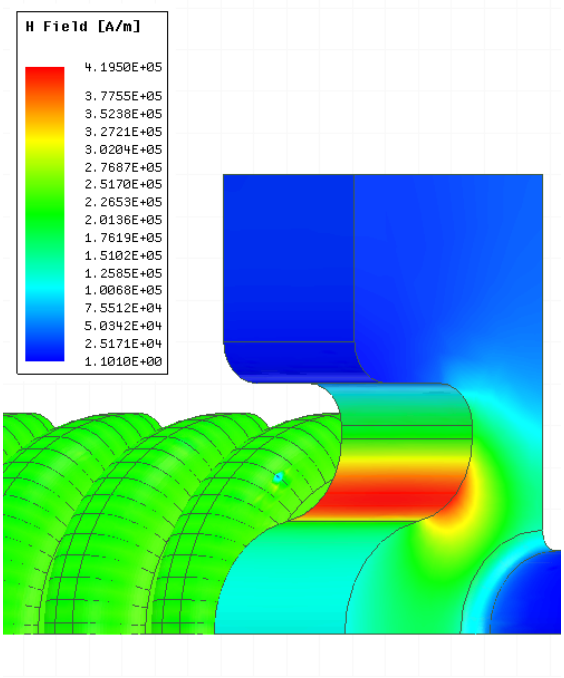

Figure 5.38. Magnitude of the surface H field of the input coupler.

As already mentioned, another aspect to consider is the quadrupole component of the magnetic field. Designing the couplers, it has been found the value of Δx that avoids the difference between the magnitudes of the magnetic field in the center of the matching cell for θ=0° and θ=90° [138]. In Fig. 5.39, a comparison between the couplers, with and without racetrack, is shown . Data has been calculated along an arc placed in the longitudinal coupler center, having a radius of 2 mm. It is possible to observe that the racetrack geometry strongly minimize the quadrupolar component of the magnetic field in both the couplers.

The equivalent quadrupole gradients due to E and B fields can be approximated by [88]:

$$g_B \cong \frac{|B_{y\_line1}| - |B_{x\_line2}|}{2r}, \tag{5.23}$$

$$g_E \cong \frac{|E_{x\_line1}| - |E_{y\_line2}|}{2cr}, \tag{5.24}$$

where the gradients are expressed in T/m and $line1$ and $line2$ are shown in Fig. 5.40. It is an overestimation of the quadrupole kick since based on the magnitudes

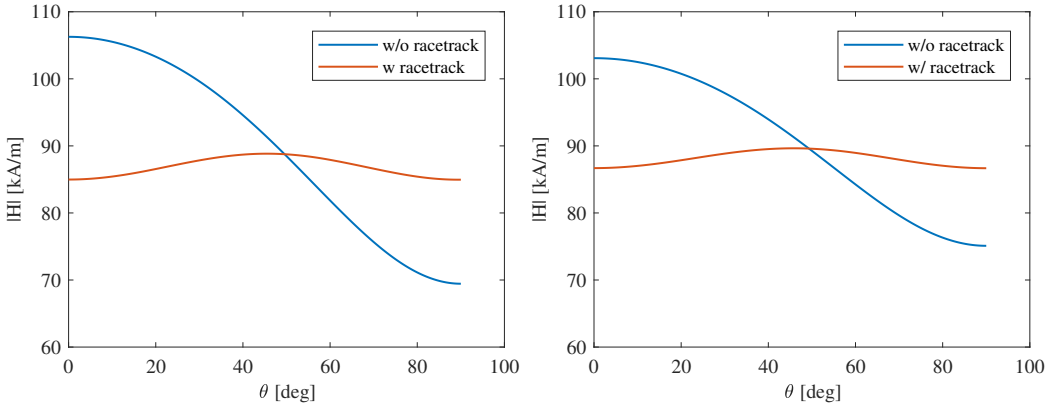

Figure 5.39. Magnitude of the magnetic field in the center of the matching cell in input (left) and output (right) coupler with and without the racetrack (arc with radius of 2 mm in the center of the coupler).

of H and E.

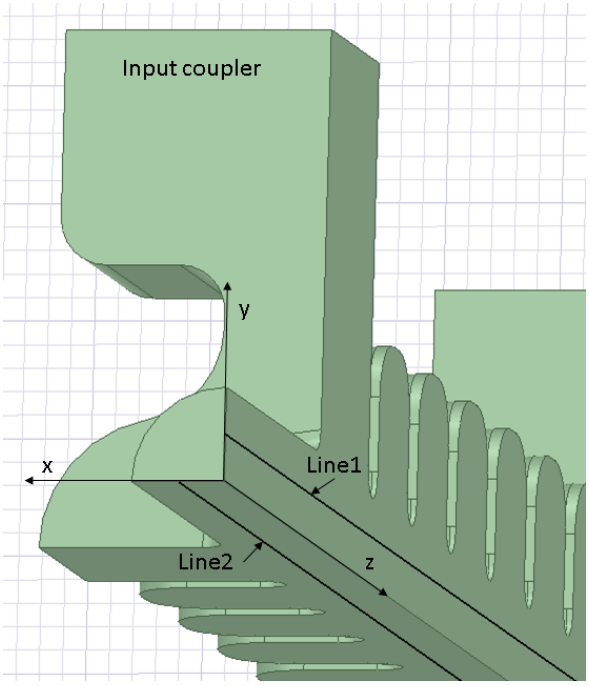

Figure 5.40. Input coupler geometry with lines for transverse field calculations.

A more precise way to determine the quadrupole gradients is applying the previous formula considering the particle injection phase ϕ_{inj}. Eqs. (5.23) and (5.23) lead then to [88]:

$$g'_B \cong \frac{Re\left[\left(|B_{y\_line1}| + |B_{x\_line2}|\right) e^{j\left(\omega_{rf}\frac{z}{c}+\phi_{inj}\right)}\right]}{2r}, \tag{5.25}$$

$$g'_E \cong \frac{Re\left[\left(|E_{x\_line1}| - |E_{y\_line2}|\right) e^{j\left(\omega_{rf}\frac{z}{c}+\phi_{inj}\right)}\right]}{2cr}, \tag{5.26}$$

where the injection phase is the one that maximize the quantity

$$V = \int_{L_c} E_z e^{j\left(\omega_{rf}\frac{z}{c}+\phi\right)} dz, \tag{5.27}$$

where L_c is the length of the coupler. Indeed, the injection phase depends on how long is the portion of waveguide in the HFSS design and it is not related to the one of the real structure. In Fig. 5.41, g'_E and g'_B as a function of the position z of the 7 cells structure are shown (with and without racetrack). It is clear that the racetrack allows to strongly minimize the quadrupolar component of the magnetic field in the coupler, while the electric field remains more or less the same.

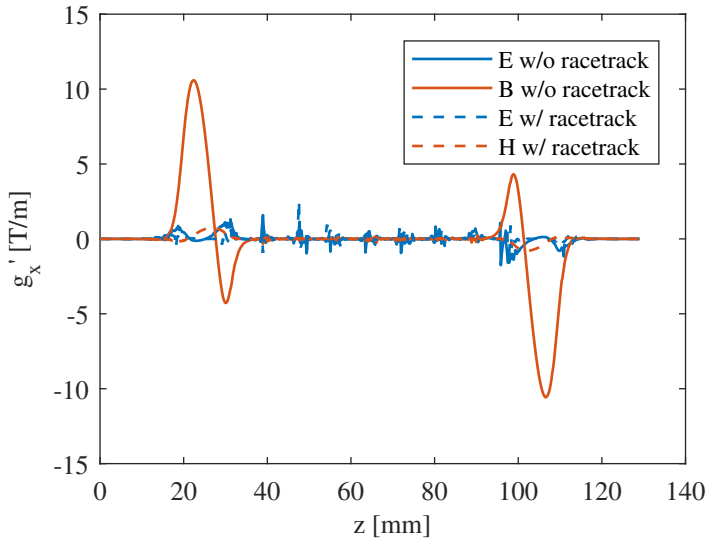

Figure 5.41. Equivalent quadrupole gradients due to the E and B fields along the the 7 cells structure for the design of input coupler.

The integrated gradients are given by the formulas:

$$G'_B = \int_{L_c} g'_E \, dz, \tag{5.28}$$

$$G'_E = \int_{L_c} g'_E \, dz, \tag{5.29}$$

where they are expressed in T. The total contribution is

$$G' = G'_B + G'_E, \tag{5.30}$$

and in our case it is equal to 5 mT, while without racetrack it is 55 mT (more than a factor 10 higher).

Another way to quantify the minimization of the multipolar field components has been presented in Ref. [141]. The quadrupole kick experienced by a relativistic electron beam can be calculated integrating the longitudinal electric field E_z and then calculating its quadrupole component.

Assuming a beam traveling parallel to the propagation axis z, but with an offset r, we have the following voltage:

$$V_{\mp}(r,\theta) = \int_{L_c} E_z(r,\theta,z) e^{\mp i k_0 z} dz, \tag{5.31}$$

where k_0 is the wavenumber of the input rf power, θ is the azimuthal angle and i is the imaginary unit. The minus sign refers to electron counterpropagating with the rf power, while plus refers to beam copropagating with the rf power.

The quadrupole component is determined calculating the discrete Fourier transform versus θ_j of $V_{\mp}(r,\theta)$:

$$M_{\mp,s}(r) = \frac{1}{\sqrt{n}} \sum_{j=1}^{n} V_{\mp}(r,\theta_j) e^{2\pi i (j-1)s/n}, \tag{5.32}$$

where j is the index of sampled azimuthal angles, n is the number of azimuthal variations and $M_{\mp,s}$ is the mode being calculated with index s. $M_{\mp,0}$ is the monopole component, $M_{\mp,1}$ is the dipole component and $M_{\mp,2}$ is the quadrupole component. Fig. 5.42 shows the reduction of the multipole modes of the voltage for counter-propagating electrons due to the racetrack geometry for r=2 mm, while Table 5.11 summarizes the obtained results. It is possible to observe that components until the 4th mode are reduced. In particular, the quadrupole component is reduced of a factor greater than 10.

Table 5.11. Discrete Fourier coefficients for counter-propagating particles for r=2 mm.

Coupler type	**Units**	$M_{-,1}$	$M_{-,2}$	$M_{-,4}$
w/o racetrack	kV	5.265	19.58	3.041
w/ racetrack	kV	0.928	1.72	2.654

5.3 CompactLight

The H2020 CompactLight Project [53, 142] aims to design the next generation of compact X-ray Free Electron Lasers, relying on very high gradient accelerating structures (X-band, 12 GHz), the most advanced concepts for high brightness electron photo injectors, and innovative compact short-period undulators.

CompactLight (also named XLS) is an international collaboration, funded by

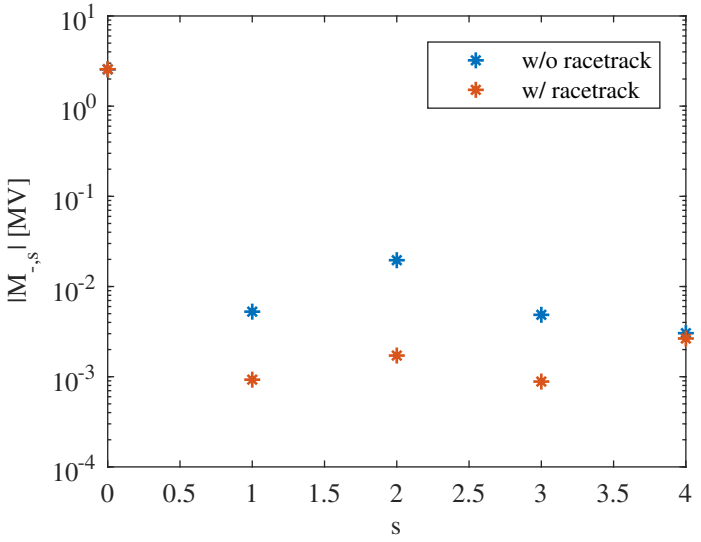

Figure 5.42. Comparison of $M_{-,s}$ in the coupler for r=2 mm.

the European Union, including 24 partners and 5 associated institutes. The main goal of the collaboration is to facilitate the development of X-ray FEL facilities across Europe and beyond, by making them more affordable to construct and operate, through an optimum combination of emerging and innovative accelerator technologies. The three-year design study, funded in the framework of the Horizon 2020 Research and Innovation Programme 2014-2017, has been started in January 2018, and intends to design a hard X-ray FEL facility beyond the state of the art. Compared with existing facilities, the proposed facility will benefit from a lower electron beam energy, due to the enhanced undulator performance; be significantly more compact, as a consequence of the lower beam energy and the high gradient of the X-band structures; be more efficient (less power consumption), as a consequence of the lower energy and the use of high-frequency structures. These ambitious, but realistic aims, will make the design less expensive to build and operate when compared with the existing facilities, making X-ray FELs more affordable. Based on user-driven scientific requirements (i.e. wavelength range, beam structure, pulse duration, synchronisation to external laser, pulse energy, polarisation, etc.), the goal is to provide the design of an ideal X-band driven hard X-ray FEL, including, as well, options for soft X-ray operation.

The user requirements for CompactLight have been established interacting with existing and potential FEL users in a variety of formats. With regard to the tunability, there is a clear demand for photon energies as low as 0.2 keV and as high as 20 keV. The mean photon energy of the desired tunable range is about 4 keV. For pump-probe experiments, most respondents want the synchronization between the FEL and the external laser to be in the order of 10 fs [143]. The photon output

specifications are summarized in Table 5.12.

Table 5.12. Main parameters of the CompactLight FEL.

Parameter	Units	Soft X-ray	Hard X-ray
Photon energy	keV	0.25 - 2.0	2.0 - 16.0
Wavelength	nm	5.0 - 0.6	0.6 - 0.08
Repetition rate	Hz	1000	100
Pulse duration	fs	0.1 - 50	1 - 50
Two-pulse delay	fs	$\pm$100	$\pm$100
Two-colour separation	%	20	10
Laser-FEL synchronization	fs	<10	<10

5.3.1 Layout and main parameters of the linac

A preliminary layout of the CompactLight facility is shown in Fig. 5.43 [53]. Conventionally, only one fundamental resonance wavelength exists in the FEL because of the simple linear structure of the undulator. By operating the FEL using a two section undulator each with different deflection parameters, K_1 and K_2, respectively, it is possible to achieve laser action at two different wavelengths simultaneously. This is the so-called *two-colour mode* [144]. A key request from the user community, which significantly affects the facility layout, is the requirement for large wavelength separation when operating in two-colour mode. This effectively means that two bunches must independently reach saturation in two different undulators. Normally, it would be expected that this would happen in a very long undulator, tuned for two different wavelengths. However, it has been decided to operate in parallel (i.e. the two different wavalengths at the same time) rather than series (i.e. the two wavelength one after the other one), which means that there are two separated FEL lines. This has several additional advantages. First, the total undulator length is approximately the same and so the parallel option is more compact overall; second, the two independent wavelengths could be combined into a single experiment or, if that is not required, two experiments could take place at the same time, doubling the capacity of the facility.

Furthermore, the two FEL lines are planned to operate over the full wavelength range. When running in hard X-ray mode (named HXR) the electron energy will be up to 5.5 GeV at 100 Hz, in soft X-ray mode (named SXR) the energy will be up to 2 GeV and, since the linac gradient will be much reduced, the repetition rate will be able to be increased significantly. A repetition rate of 1000 Hz for the soft-X-ray FEL would be a unique and highly desirable feature of the facility. It is a very challenging target for many systems, and a feasibility study will be performed during the course of the design study. Preliminary results about this aspect are described

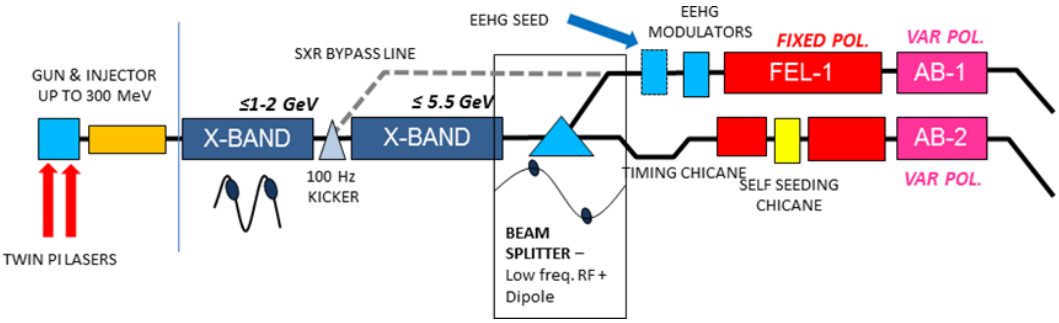

Figure 5.43. Sketch of the entire CompactLight facility in a two-pulse, two-color scheme [53].

in Subsection 5.3.7. Other additional concepts are considered, which include seeding in both FELs and a bypass line at 2 GeV so that one FEL could run in soft X-ray mode and the other in hard X-ray mode, both at 100 Hz.

As shown in Fig. 5.43, the linac layout consists of an injection section, up to 300 MeV, with a high-brightness electron source and a laser heater, to mitigate the micro-bunching instability. A two-stage magnetic compression scheme (BC1 + BC2) is adopted. The first magnetic bunch compressor (BC1) is located at 300 MeV. Two X-band linacs (named Linac1, upstream the kicker, and Linac2, downstream the kicker, respectively), separated with a second bunch compressor (BC2) at an energy between 1 GeV and 2 GeV, will boost the beam energy up to 5.5 GeV. At the exit, the beam is steered to different undulators with a spreader. For the electron source, three photocathode rf guns operated at S-, C-, and X-band are considered. While for the first two options an X-band cavity will be adopted to linearise the beam longitudinal bunch profile, for the X-band option it is under investigation the possibility to use a lineariser operating at 36 GHz (K_a-band) [145]. Moreover, for all the solutions, it is under investigation the possibility to use rf velocity bunchers and, possibly, passive linearisers. For the main linac, the goal is to define a standardised rf unit based on the CLIC technology, which can be used in all the main and sub-design variants. In addition to the accelerating structures, the rf unit will include klystron, rf compressor and waveguide components as well. This choice will greatly simplify the industrialisation process, with a considerable reduction in production costs. Table 5.13 lists the main electron beam and FEL parameters for the 100 Hz repetition rate scenario.

As for EuPRAXIA@SPARC_LAB, the chosen technology of the booster is X-band since, also for CompactLight, one of the goals is an overall small size. In this case, there are no constrains in terms of total length and an average accelerating gradient of 65 MV/m has been chosen. As already described, two main configurations are foreseen: high-gradient/low-repetition rate (100 Hz) and low-gradient/high-

Table 5.13. Main Electron Beam and FEL Parameters.

Parameter	Value
Max energy	5.5 GeV @100 Hz
Peak current	5 kA
Normalised emittance	0.2 mm mrad
Bunch charge	<100 pC
RMS slice energy spread	10^{-4}
Max photon energy	16 keV
FEL energy tuning range at fixed energy	×2
Peak spectral brightness @16 keV	1033 ph/s/mm^2/mrad^2/0.1%bw

repetition rate (250 Hz and above). For the design of the linac, the 100 Hz operating mode has been considered. The total energy gain is 5.2 GeV that gives a total active length of 80 m at 65 MV/m. In Table 5.14, main parameters of the X-band linac are reported. Like EuPRAXIA@SPARC_LAB, the CPI VKX-8311A klystron has

Table 5.14. CompactLight's main linac parameters.

Parameter	Units	Linac1	Linac2
Acc. Gradient $\langle G \rangle$	MV/m	65	
Initial energy W_0	GeV	0.3	2
Final energy W_f	GeV	2	5.5
Energy gain W_{gain}	GeV	1.7	3.5
Active length	m	26.2	53.8

been chosen as the reference rf power source. The structures operate then at 11.9942 GHz with a phase advance per cell of $2\pi/3$. Also in this case, SLEDs systems have been chosen as pulse compressors.

5.3.2 Minimum average iris radius of the structure

For the CompactLight project, the average iris radius of the structure has been fixed equal to 3.5 mm (a/λ=0.140) by the beam dynamics group. Beam parameters are still under discussion but preliminary values at the entrance of Linac1 are reported in Table 5.15.

Inserting the parameters of Table 5.15 into the equations of Subsection 5.2.2, we have obtained a minimum average iris radius of 2.7 mm to have a growth parameter equal to 2. With an average iris radius of 3.5 mm we have obtained a growth parameter equal to 0.73.

Table 5.15. CompactLight's main parameters of Linac1.

Parameter	Units	Value
W_0	MeV	300
W_{L1}	MeV	2000
$\langle G \rangle$	MV/m	65
Charge	pC	75
σ_z	µm	105
$\langle \beta \rangle$	m	∼10

5.3.3 Analytical structure length optimization

For the design of the structure, as for EuPRAXIA@SPARC_LAB, a preliminary study with analytical formulas has been performed. The same cell design and parameters obtained for EuPRAXIA@SPARC_LAB have been used for CompactLight (see Subsection 5.2.3). The effective shunt impedance as a function of the section attenuation is reported in Fig. 5.44 for a CI and a CG structure, while the optimal structure length as function of the structure average iris aperture is reported in Fig. 5.45. For the CI structure, the optimal length is 0.890 m while, for the CG one, it is 0.818 m. Also in this case, these values have been used as a guideline for a numerical optimization.

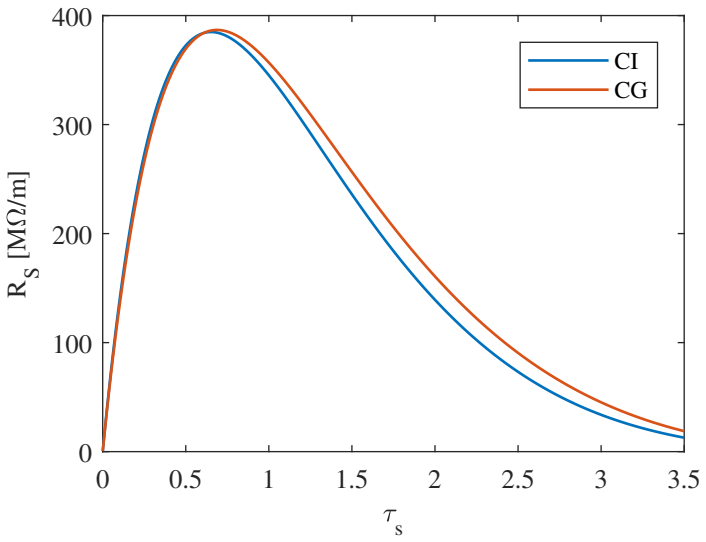

Figure 5.44. Effective shunt impedance as a function of the section attenuation for CI and CG structures.

5.3.4 Numerical effective shunt impedance optimization

Using the results shown in the previous Subsection, the calculation of the structure effective shunt impedance has been performed. Considering again a linear cell-by-cell

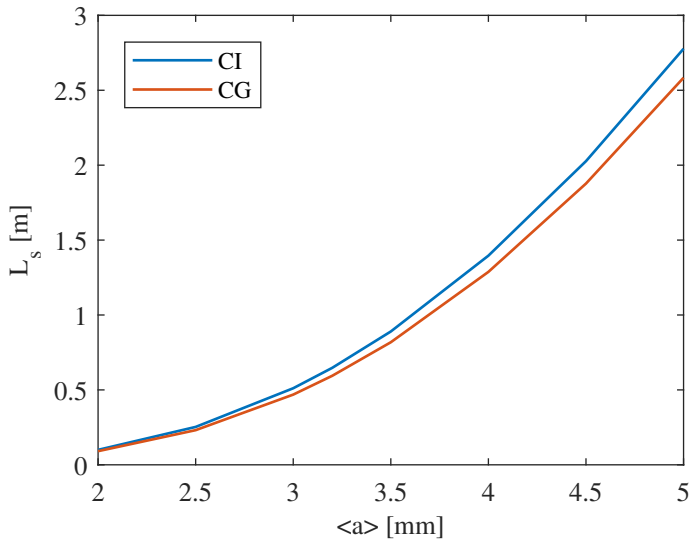

Figure 5.45. Optimal structure length as function of the average iris radius for CI and CG structures.

tapering, a scan from 0 to 0.2° of the tapering angle θ has been performed for three different structure lengths: 0.7, 0.8 and 0.9 m. Main results are reported in Figs. 5.46, 5.47 and 5.48. For a better power distribution we opted for 90 cm long structures with a tapering angle of 0.1°, as a good compromise between rf efficiency and expected breakdown rate.

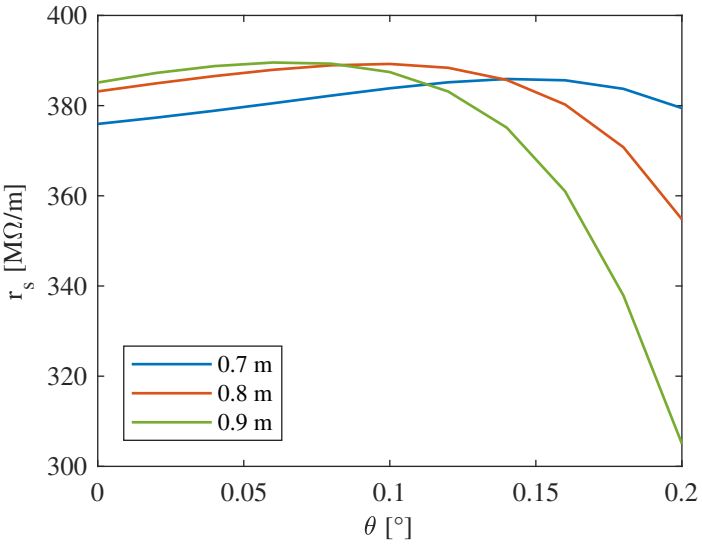

Figure 5.46. Structure effective shunt impedance as function of tapering angle for three different structure lengths.

Structure parameters are summarized in Table 5.16, where a comparison with the 90 cm structure designed for SLAC NLCTA is shown. Indeed, the obtained results

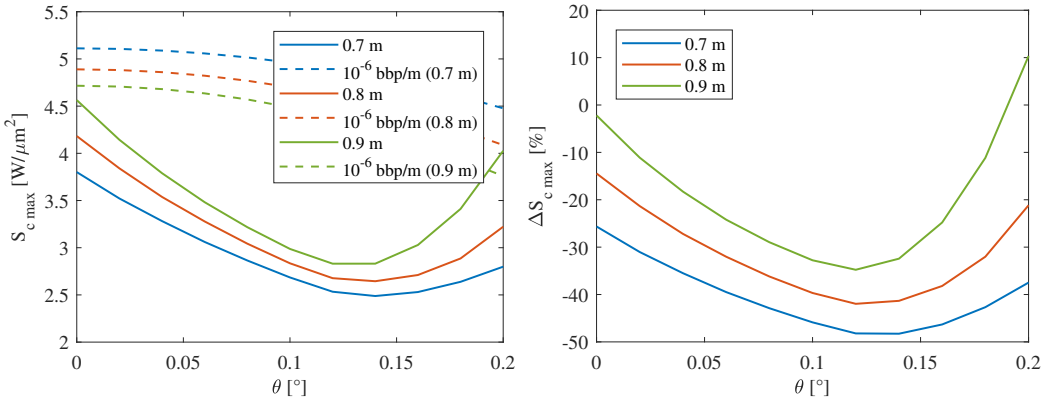

Figure 5.47. Peak value of modified Poynting vector in the structure as function of the tapering angle for three different structure lengths.

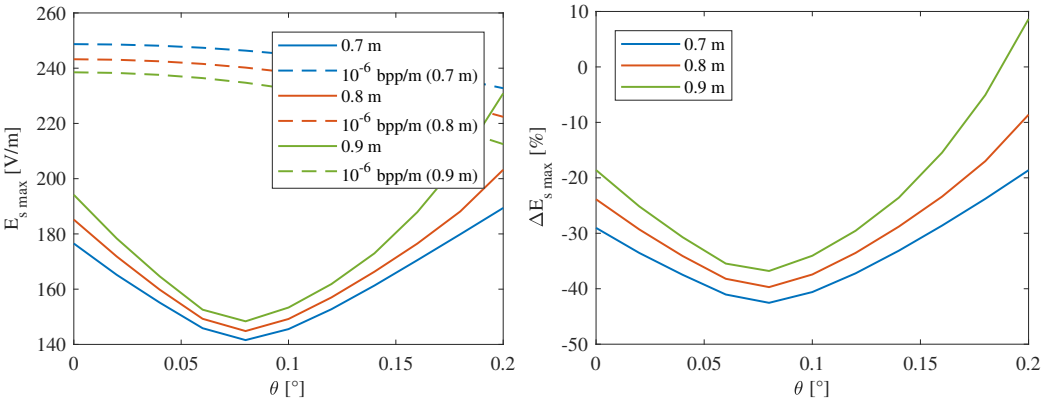

Figure 5.48. Peak value of surface electric field in the structure as function of the tapering angle for three different structure lengths.

are very similar to the ones of NLCTA. The Next Linear Collider Test Accelerator (NLCTA) [146] is an extremely versatile facility that currently hosts programs in accelerator physics, advanced light source R&D and medicine. The 60-150 MeV high-brightness electron beam linear accelerator and extensive infrastructure can be adapted to support a wide range of studies. The facility currently runs programs in free electron laser seeding, dielectric laser acceleration and medical studies. At the beginning, the purpose of NLCTA was to be a test facility to construct and operate an engineered model of a high-gradient linac suitable for the NLC (Next Linear Collider) [147] and test the dynamics of the beam during acceleration [148]. The rf system consisted of a 90 MeV injector and a 540 MeV linac. The main components of the injector were two low-Q single-cavity prebunchers and two 0.9m-long detuned accelerator sections. The linac system consisted of six 1.8m-long detuned and damped detuned accelerator sections powered in pairs. The rf power generation, compression, delivery, distribution and measurement systems consist of klystrons,

SLED-II energy compression systems [149], rectangular waveguides, magic-T's, and directional couplers [150, 151]. With respect to NLCTA, XLS structures have a smaller average iris radius and then a smaller group velocity, higher filling time and shunt impedance.

Table 5.16. Comparison between main parameters of the CompactLight's and NLCTA's X-band structures.

Parameter	**Unit**	**CompactLight**	**NLCTA**
Phase advance per cell		$2\pi/3$	
Frequency f_{rf}	GHz	11.994	11.424
Structure length L_s	m	0.9	0.93
Number of cells N_c		108	106
Iris radius first-last cell a	mm	4.278-2.722	5.715-3.930
Average iris radius $\langle a \rangle / \lambda$		0.140	0.180
Iris thickness t	mm	2.0	1.0-2.0
Shunt impedance r	MΩ/m	90-131	68-88
Q-factor Q		7152-7000	$\sim$7030
Normalized group velocity v_g/c	%	4.7-1.0	11.8-3.0
Filling time t_f	ns	144	52
Section attenuation τ_s		0.767	0.255
Average gradient $\langle G \rangle$	MV/m	65	70

In Table 5.17, the main parameters of the structure are reported and compared with the ones obtained for EuPRAXIA@SPARC_LAB (EuSPARC). Due to the higher average iris radius, the effective shunt impedance of the 90 cm structure is a bit lower with respect to the 50 cm one. For CompactLight, it has been obtained an optimal power distribution in an rf module made up of 4 structures fed by one klystron equipped with a SLED. Indeed, the required klystron power per module is 39 MW while the available klystron power has been estimated equal to 40 MW, having considered a total power attenuation of 20%. In Fig. 5.49, a sketch of the rf module is shown.

Linac1 is made up of 32 structures (8 modules) for a total on-crest enegy gain of 1872 MeV in 28.8 m of active length, while Linac2 is made up of 60 structures (15 modules) for a total on-crest enegy gain of 3510 MeV in 54 m of active length. Main parameters are summarized in Table 5.18.

5.3.5 Design of the rf power couplers

Also for CompactLight, z-type slot rf power couplers have been studied because of their compactness. The technique used for the design and optimization is the same described in Subsection 5.2.9. The main geometrical parameters of input and output couplers are reported in Table 5.19.

Table 5.17. Comparison between main parameters of the CompactLight's and EuPRAXIA@SPARC_LAB's X-band linacs.

Parameter	Units	CompactLight	EuSPARC
Available klystron power	MW	∼40	
Klystron pulse length	µs	1.5	
Repetition rate f_{rep}	Hz	100	
SLED Q_0		180000	
SLED Q_e		23000	19300
Total active length L_t	m	82.8	16
Number of structures N_s		47	32
Structure length L_s	m	0.9	0.5
Number of cells N_c		108	60
Iris radius first-last cell a	mm	4.278-2.722	3.629-2.771
Normalized group velocity v_g/c	%	4.68-0.96	2.76-1.03
Filling time t_f	ns	144	100
Section attenuation τ_s		0.767	0.534
Shunt impedance r	MΩ/m	90-131	105-130
Q-factor Q		7152-7000	7076-7003
r/Q	kΩ/m	12.5-18.7	14.9-18.9
Effective shunt impedance r_s	MΩ/m	387	410
P_{out}/P_{in}		0.22	0.34
Average gradient $\langle G \rangle$	MV/m	65	80
Energy gain W_{gain}	MeV	5382	1280
Peak input power	MW	68	58
Input power averaged over the pulse	MW	44	42
Structures per module		4	8
Total number of modules		23	4
Total number of structures		92	32
Klystron power per module	MW	39	54
Total number of klystrons		23	8

Table 5.18. Main parameters of the CompactLight's Linac1 and Linac2.

Parameter	Units	Linac1	Linac2	Total
Repetition rate	Hz		100	
Average gradient $\langle G \rangle$	MV/m		65	
Energy gain per module	MeV		234	
Number of structures		32	60	92
Number of modules		8	15	23
Number of klystrons		8	15	23
Linac active length	m	28.8	54	83
Maximum Energy gain	MeV	1872	3510	5382

The obtained reflection coefficient at the the input port is -44.9 dB for the input coupler and -37.4 dB for the output one. In the input coupler, the maximum value

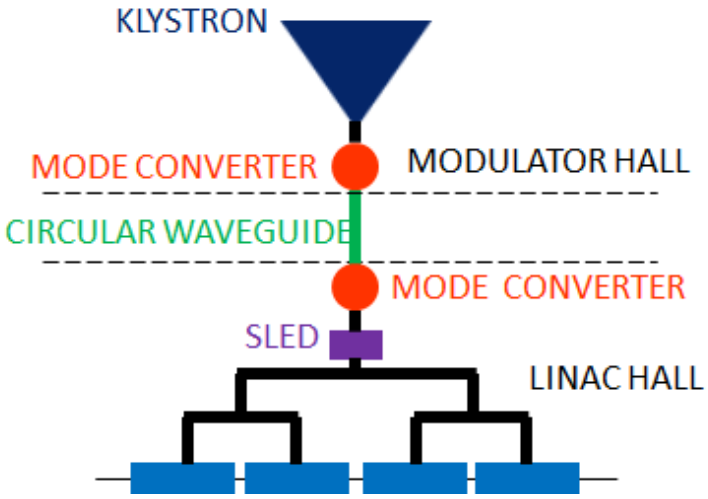

Figure 5.49. Sketch of the CompactLight's rf module.

Table 5.19. Main geometrical parameters of the EuPRAXIA@SPARC_LAB's rf power couplers.

Parameter	Units	Input coupler	Output coupler
Waveguide rounding r_{wg}	mm	2	
Waveguide-slot rounding r_1	mm	2	
Slot-matching cell rounding r_2	mm	4	
Matching cell radius R_c	mm	5.063	6.308
Off-axis circle center Δx	mm	8.359	4.765
Slot width w	mm	9.017	7.819

of the surface magnetic field is 374.8 kA/m, with the peak power of 68 MW of Table 5.17 at the input port (divided by 4 since it is referred to one quarter of the structure). In Fig. 5.38, it is shown the magnitude of the surface H field obtained with HFSS. By using Eq. (3.10) and considering that the filling time is 144 ns, we obtain a pulsed heating of 24 °C. Also in this case, the obtained pulsed heating can be considered absolutely safe in terms of breakdown rate and damages probabilities.

In Fig. 5.51, a comparison between the couplers with and without racetrack is shown. Results are referred to an arc of 2 mm radius placed at the longitudinal center of the coupler. Also in this case, the racetrack geometry strongly minimize the quadrupolar component of the magnetic field.

In Fig. 5.52, g'_E and g'_B as a function of the position z in the 7 cells structure used for the design of the input coupler are shown (with and without racetrack). Also in this case, the racetrack geometry allowed to minimize the quadrupolar component of the magnetic field, while the electric field remains more or less the same.

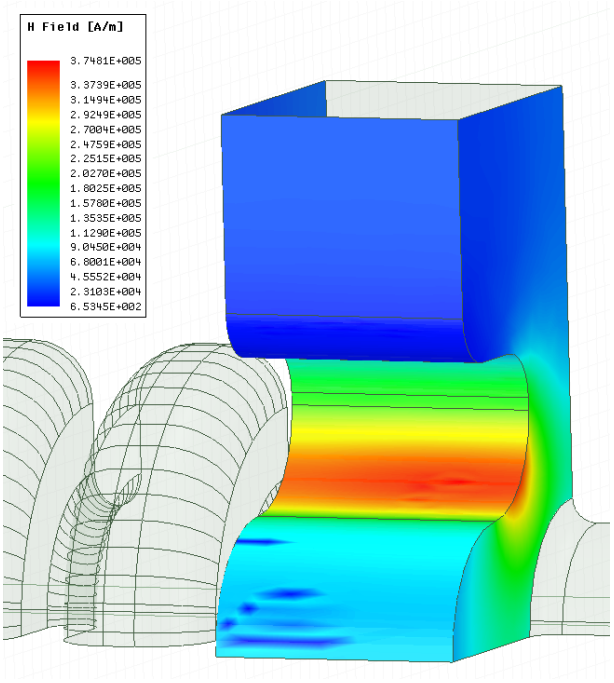

Figure 5.50. Magnitude of the surface H field of the input coupler.

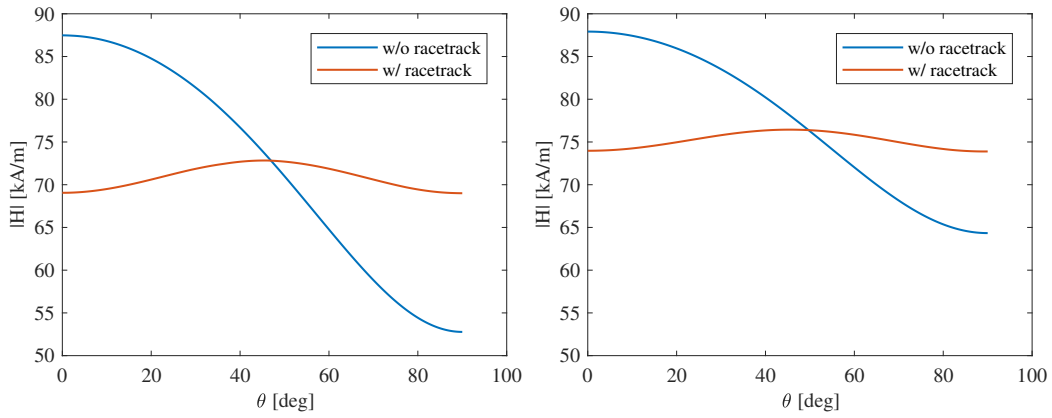

Figure 5.51. Magnitude of the magnetic field in the center of the matching cell in input (left) and output (right) coupler with and without the racetrack (circle radius r of 2 mm).

The integrated equivalent gradient has been minimized to 4 mT, while without racetrack it is 30 mT.

By using Eqs. (5.31) and (5.32), the multipolar components of the kick due to the longitudinal electric field have been calculated. Results are shown in Fig. 5.53 and Table 5.20. Also in this case, the dipolar and the quadrupolar components are minimized thanks to the racetrack geometry. In particular, the quadrupole component is more than one order of magnitude lower with respect to the geometry without racetrack.

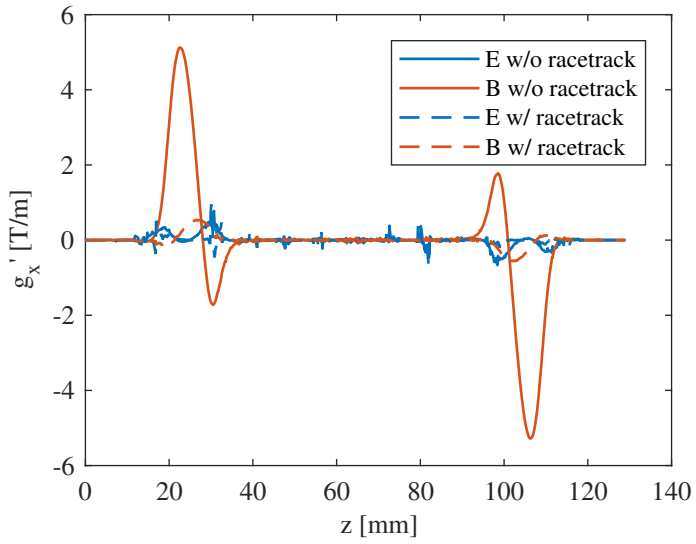

Figure 5.52. Equivalent quadrupole gradients due to the E and B fields along the 7 cells structure used for the design of the input coupler.

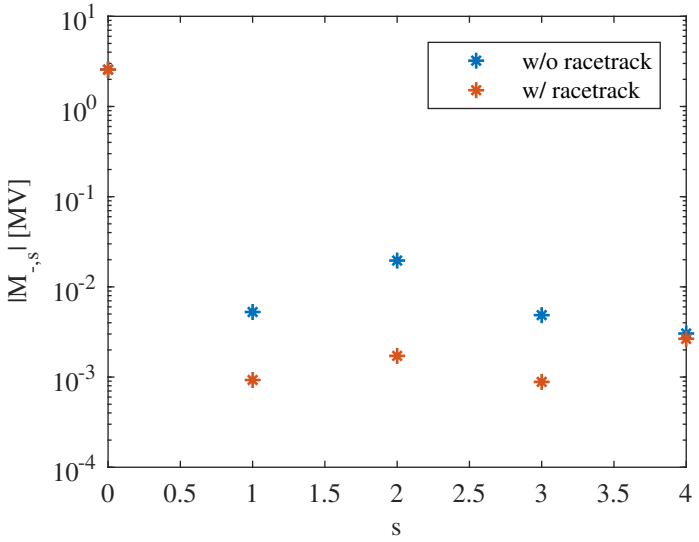

Figure 5.53. Comparison of $M_{-,s}$ in the coupler for r=2 mm.

Table 5.20. Discrete Fourier coefficients for counter-propagating particles for r=2 mm.

Coupler type	**Units**	$M_{-,1}$	$M_{-,2}$	$M_{-,4}$
w/o racetrack	kV	0.899	2.874	1.127
w/ racetrack	kV	0.157	0.189	1.154

5.3.6 RF module optimization

As shown in Subsections 5.2.5 and 5.3.4, the waveguide network adopted for EuPRAXIA@SPARC_LAB and CompactLight is a simple binary tree with fully

symmetric branches. In order to let the beam always see the on crest phase, the right distances between the structures have been calculated. In Fig. 5.54 [152], a sketch of the CompactLight's rf module including diagnostics, optics and vacuum elements is shown, while in Fig. 5.55, a detail of the waveguide network is shown. The layout has been produced in collaboration with the CompactLight's rf and beam dynamics groups. For the calculations, a total structure length of 103 cm has been considered, including couplers and flanges.

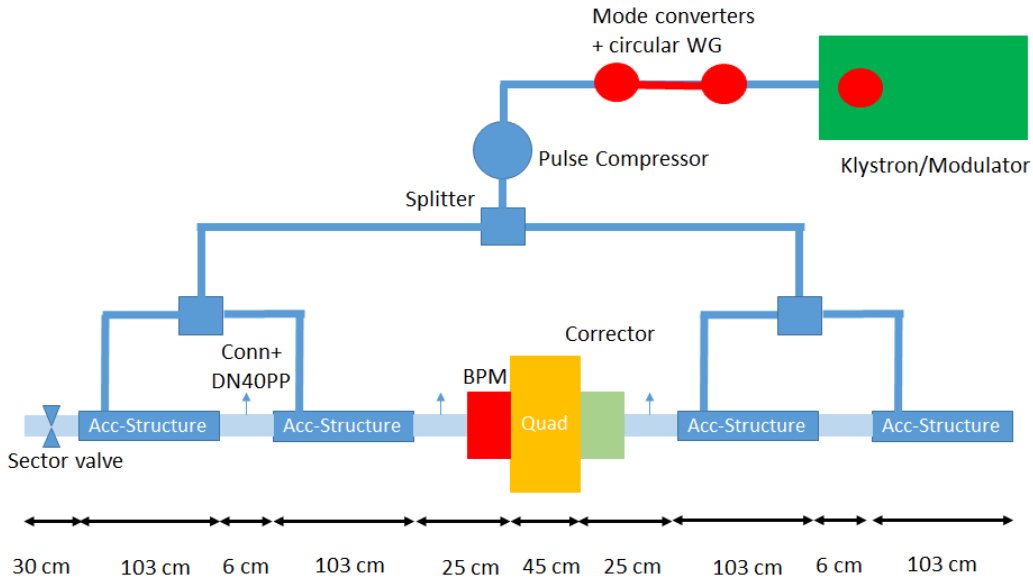

Figure 5.54. Sketch of the CompactLight's rf module with diagnostics, optics and vacuum elements [152].

Due to the delays introduced by the hybrids, the optimal distances between the structures are:

$$L_1 = (N_1 - 1/4)\lambda, \tag{5.33}$$

$$L_2 = (N_2 - 1/4)\lambda, \tag{5.34}$$

$$L_3 = (N_3 + 1/4)\lambda, \tag{5.35}$$

where N_1, N_2 and N_3 are integer values and λ=24.995 mm at 11.9942 GHz. Minimum values of N have been found with the following calculations:

$$N_1 = \frac{L_1}{\lambda} + 1/4 = \frac{1030 + 60}{24.995} + 1/4 = 43.9 \rightarrow 44, \tag{5.36}$$

$$N_2 = \frac{L_2}{\lambda} + 1/4 = \frac{1030 + 250 + 450 + 250}{24.995} + 1/4 = 79.5 \rightarrow 80, \tag{5.37}$$

$$N_2 = \frac{L_3}{\lambda} - 1/4 = \frac{1030 + 60}{24.995} - 1/4 = 43.4 \rightarrow 44. \tag{5.38}$$

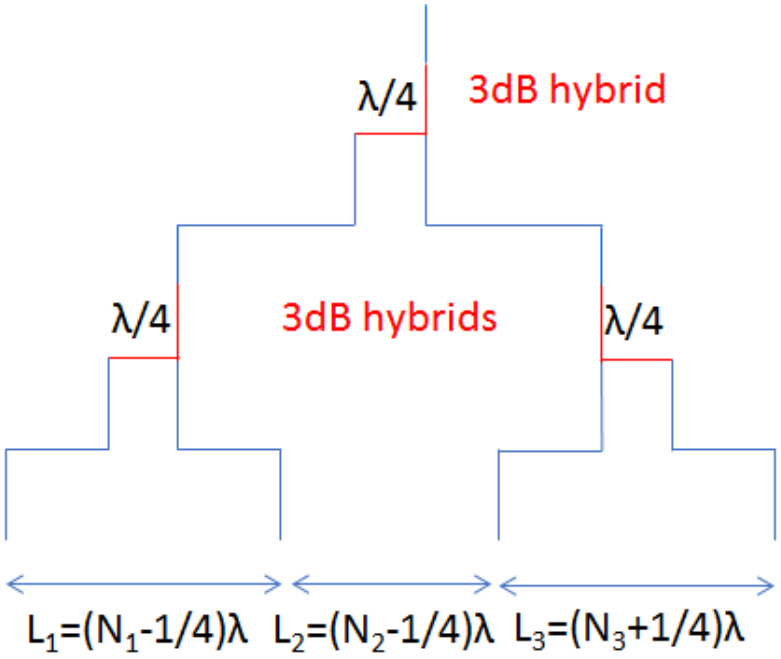

Figure 5.55. Waveguide network of the rf module.

Eqs. (5.36), (5.37) and (5.38) lead to:

$$L_1 = (44 - 1/4) \cdot 24.995 = 1093.531\,\text{mm}, \tag{5.39}$$

$$L_2 = (80 - 1/4) \cdot 24.995 = 1993.351\,\text{mm}, \tag{5.40}$$

$$L_3 = (44 + 1/4) \cdot 24.995 = 1106.029\,\text{mm}. \tag{5.41}$$

The advantage of this type of solution is the simplicity, while the drawback is that if the radiofrequency phase is synchronized with the beam in the first accelerating section, it is not with the other ones in the same module. This happens because the beam travels at the speed of light and takes a few nanoseconds to get the next structure (1 m at c speed corresponds to 3.3 ns). This leads to have a delay between the end of the compressed pulse in the structure and the arrival of the beam. This effect is clear in Fig. 5.56 [153], where the cases of optimal, early and late injection are shown. The higher is the delay (or the advance) with which the beam enters in the structure with respect to the optimal injection, the lower is the equivalent multiplication factor of the SLED seen by beam itself. Thus, the beam sees a lower accelerating field (i.e. a lower SLED multiplication factor). A solution to optimize the rf efficiency of the module is shown in Fig. 5.57 [153]. In these plots, it is reported the SLED multiplication factor M seen by the beam as a function of the injection delay. Distributing the structure injection delays along the slopes of M, it

is possible to obtain an average reduction of 2% in terms of accelerating gradient. The plot has been obtained integrating the SLED compressed pulse in a sliding time window which width is constant and matches the structure filling time (100 ns and 144 ns respectively). For the EuPRAXIA@SPARC_LAB scheme, a module made up of only structures have been considered and then, the real efficiency of a module that includes vacuum, optics and diagnostics elements will be lower.

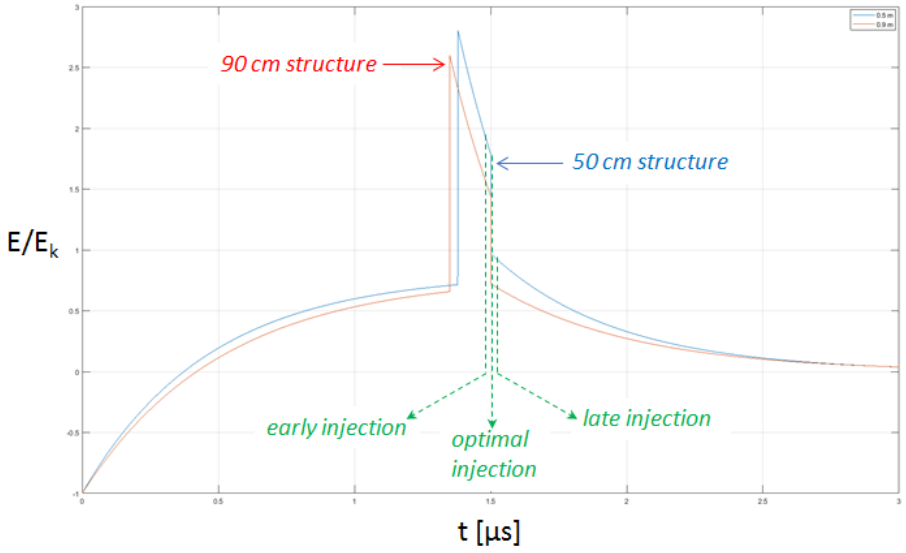

Figure 5.56. Pulses seen by the beam due to different injection times [153].

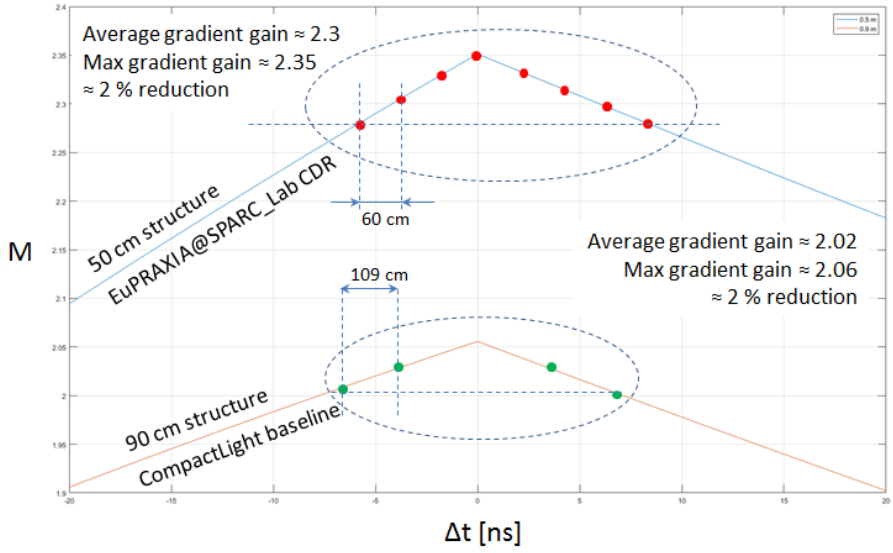

Figure 5.57. RF power delay distribution to optimize the rf efficiency [153].

5.3.7 High repetition rate operations

Nowadays, there is a high demand from light source users of high brightness coherent X-rays capable of producing ultra-short pulses at repetition rates of 1 kHz or higher [50, 53]. These requirements can only be met by light sources powered by high gain-vacuum tubes such as klystrons or Inductive Output Tubes (IOTs), which are driven by pulsed modulators. To date, the high repetition rate requirement has led to the adoption of superconducting technology for such linacs, like the European XFEL and LCLS-II [15, 49], in order to minimise the power dissipation on the structure walls and therefore reduce the rf power required in each pulse. Power efficiency of normal-conducting accelerating structures is much lower and the average power dissipated in klystrons and structures becomes the main issue.

Main limitations

Any klystron model is optimized by design to be operated in a specific working point characterized by 3 parameters:

- Maximum rf power in saturation $P_{rf\ sat}$;
- Pulse duration $t_{ft} + t_t$ (flat top + transient);
- Repetition rate f_{rep}.

The *tube efficiency* is defined as :

$$\eta = \frac{P_{rf\ sat}}{V_k I_k}, \tag{5.42}$$

where V_k and I_k are the klystron voltage and current, respectively. The efficiency is maximum when the tube is operated at the nominal working point.

The klystron operational repetition rate can be increased at expenses of the saturated rf power (by decreasing the tube high voltage) and/or the pulse duration.

The main limitation of the increase of the repetition rate comes from the *power released on the tube collector* P_{coll} which can not exceed a limit value corresponding to the nominal working point (with some margin). It is given by:

$$P_{coll} = W_{coll} f_{rep} = f_{rep} \left[\int_{t_t} V_k(t) I_k(t) dt + \int_{t_{ft}} V_k(t) I_k(t) dt \right] \tag{5.43}$$

$$\approx f_{rep} V_{k0} I_{k0} (t_{ft} + t_t), \tag{5.44}$$

where V_{k0} and I_{k0} are the nominal voltage and current of the klystron. t_t is the rise time needed to reach the 90% of the flat top from the 10% of it and mainly depends on modulator characteristics.

As described at the beginning of this Section, one of the goals of CompactLight is to operate the linac at a frequency higher than 100 Hz (the goal is 1 kHz). Up to now, there are no sources at 12 GHz that natively support 1 kHz. The only klystron that is designed to operate at 400 Hz is the Canon E37113. Its specifications are reported in Table 5.21 [154].

Table 5.21. Specifications of the Canon E37113 klystron.

Parameter	Units	Value
Frequency	MHz	11.994
Output Power	MW	6
Efficiency	%	37
Gain	dB	41
Pulse Length	µs	5
Pulse-Rate	pps	400
Beam Voltage	kV	152
Beam Current	A	96

Klystron collector power limits are conservatively specified by manufacturers assuming transient times longer than those provided by state-of-the-art solid state modulators. Canon (formerly Toshiba) specifies tubes (e.g. E37113 in X-band and E37212 in C-band) assuming $t_t \approx 2.5\,\mu s$. Assuming the same t_t value for the CPI VKX-8311A klystron, we obtain:

$$P_{coll} \approx f_{rep} V_{k0} I_{k0} (t_{ft} + t_t) = f_{rep} \frac{P_{rf\ sat}}{\eta} (t_{ft} + t_t) \tag{5.45}$$

$$= 100Hz \cdot 310kV \cdot 410A \cdot (1.5\,\mu s + 2.5\,\mu s) = 50.8kW. \tag{5.46}$$

Since the limit imposed by P_{coll} can not be overcome, the repetition rate can only be increased at the expenses of the rf saturation power (high voltage working point) and/or the rf pulse duration. The amount of the repetition rate increase, obtainable by reducing the pulse duration, strongly depends on the value of the dead time t_t, which is a characteristic of the modulator. A reasonable value of t_t (based on measurements performed by the rf group at LNF-INFN) can be fixed equal to 1.5 µs [153]. The amount of the repetition rate increase obtainable by reducing the high voltage and the rf saturation power $P_{rf\ sat}$ is limited by the tube efficiency decrease.

Possible klystron and linac configurations

Considering these facts, 3 different possible klystron configurations have been studied to increase the repetition rate of the linac:

- Pulse shortening of the CPI VKX-8311A klystron;

- Peak power reduction of the CPI VKX-8311A klystron;
- Pulse shortening of the Canon E37113 klystron.

In the first configuration, the repetition rate can be increased up to 250 Hz by shortening the pulse of the CPI klystron up to the structure filling time (144 ns). In this configuration, the SLED would be bypassed and, due to this, the maximum average accelerating gradient is reduced to 32 MV/m. The klystron still works at its nominal working point.

In the second one, the repetition rate can be increased up to 250 Hz reducing the high voltage applied to the CPI klystron. With a saturation power of 10 MW (which corresponds to a klystron efficiency of ∼8.5%) and using the SLED, it is possible to obtain a repetition rate of 200 Hz and an average accelerating gradient of 29 MV/m. Instead, with a saturation power of 5 MW (which corresponds to a klystron efficiency of ∼7.5%), using the SLED, it is possible to obtain a repetition rate of 250 Hz and an average accelerating gradient of 20 MV/m. In this case, the klystron would work very far from its nominal working point and the efficiency is worse than the previous option. For these reasons, the peak power reduction configuration will not be considered in a possible layout.

In the last configuration, the repetition rate can be increased up to 1 kHz shortening the pulse duration of the Canon klystron to 1.5 µs. In this configuration, the SLED would still work and the maximum average accelerating gradient would be reduced to 23 MV/m, with 1 klystron per module, and 32 MV/m with two klystrons, combined together, per module. Canon is also developing a new klystron with the same specification of the E37113 model but with an output peak power of 10 MW instead of 6 and a native repetition rate of 1 kHz. With this new klystron (named HRRK by us, High Repetition Rate Klystron) it is possible to reach 30 MV/m with only one klystron per module. Also in this case, the klystrons work at their nominal working point. The operation at 65 MV/m could be assured installing also the CPI VKX-8311A klystron in each module by means of an rf switch. A sketch of this module is shown in Fig. 5.58.

These configurations lead to 3 different possible options for the linac layout operating at high repetition rate:

- *Dual Mode*, where Linac1 and Linac2 are both made up of all equal modules with one CPI VKX-8311A klystron each;
- *Dual Linac*, where Linac1 is made up of modules with one 10 MW 400 Hz Canon klystron (or two Canon E37113 klystrons) each and Linac2 is made up of modules with one CPI VKX-8311A klystron each;

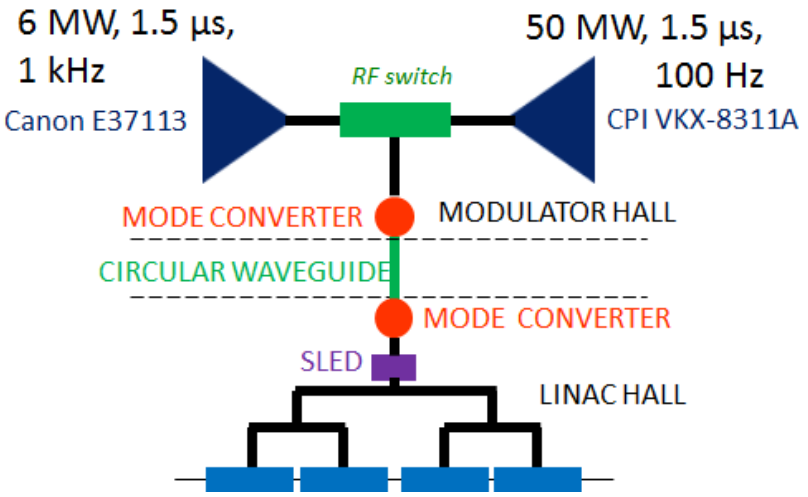

Figure 5.58. Sketch of the rf module equipped with two klystrons for high repetition rate operations.

- *Dual Source*, where Linac1 and Linac2 are both made up of all equal modules with one CPI VKX-8311A klystron and one Canon E37113 klystron each (as shown in Fig. 5.58).

In the Dual Mode option, the linac can operate at a maximum repetition rate of 250 Hz using only CPI klystrons. It is the cheapest option since it requires 23 modules (92 structures) and then 23 klystrons in total. The average accelerating gradient is 65 MV/m at 100 Hz and 32 MV/m at 250 Hz. The required total active length is 83 m. Main parameters are summarized in Table 5.22.

The Dual Linac option is made up of two different linacs with different power sources. Linac1 would operate at a maximum repetition rate of 1 kHz for SXR and Linac2 would operate at 100 Hz for HXR. The SXR (at 900 Hz) and the HXR (at 100 Hz) modes can also run in parallel by means of a 100 Hz kicker located in between. This option foresees 32 modules in total (128 structures), 17 in Linac1 and 15 in Linac2. The average gradient is 30.4 MV/m in Linac1 and 65 MV/m in Linac2. The required total active length is 135 m. Main parameters are summarized in Table 5.23.

The Dual Source option is made up of only one linac placed upstream the kicker with two different power sources per module. It operates at a maximum repetition rate of 1 kHz using Canon klystrons for SXR and at 100 Hz switching to CPI klystrons for HXR. SXR and HXR modes cannot run in parallel in this configuration. This linac option foresees 23 modules in total (92 structures) and is the most expensive one since has 46 klystrons in total. The average gradient is 30.4 MV/m at 1 kHz and 65 MV/m at 100 Hz. The required total active length is 83 m.

Main parameters are summarized in Table 5.24.

Table 5.22. Main linac parameters of the Dual Mode option.

Parameter	Units	Linac1	Linac2	Total
Number of structures	32	60	92	
Number of modules	8	15	23	
Number of klystrons		8 (CPI)	15 (CPI)	23
Linac active length	m	29	54	83
Repetition rate	Hz		100 (250)	
Average gradient $\langle G \rangle$	MV/m		65 (32)	
Energy gain per module	MeV		234 (115)	
Maximum Energy gain	MeV	1872 (921)	3510 (1728)	5382 (2649)

Table 5.23. Main linac parameters of the Dual Linac option.

Parameter	Units	Linac1	Linac2	Total
Number of structures	68	60	128	
Number of modules	17	15	32	
Number of klystrons		17 (HRRK)	15 (CPI)	32
Linac active length	m	61	54	135
Repetition rate	Hz	1000	100	-
Average gradient $\langle G \rangle$	MV/m	30.4	65	-
Energy gain per module	MeV	109	234	-
Maximum Energy gain	MeV	1853	3510	5363

Table 5.24. Main linac parameters of the Dual Source option.

Parameter	Units	HRRK	CPI
Number of structures		92	
Number of modules		23	
Linac active length	m	83	
Number of klystrons		23	23
Repetition rate	Hz	1000	100
Average gradient $\langle G \rangle$	MV/m	30.4	65
Energy gain per module	MeV	109	234
Maximum Energy gain	MeV	2507	5382

All these options have been considered valid by the rf group of the CompactLight collaboration and a definitive decision among them has not been made yet.

5.4 Joining the two projects

The X-band linac baseline shown in the EUPRAXIA@SPARC_LAB Conceptual Design Report is based on four modules hosting eight 50 cm long TW cavities each

(16 m of active length), powered by four or five klystrons in total (first phase). Considering the results obtained for CompactLight, the rf group at LNF proposed to change this baseline for a new one based on five rf modules of the type designed for CompactLight, hosting four 90 cm long TW cavities each (18 m of active length).

The second option presents some advantages:

- A simplified waveguide distribution network (four accelerating sections per module instead of eight);
- An improvement of the filling factor of the linac (i.e. the ratio between active length and real length);
- A potential better beam stay-clear, due to an higher average iris radius (3.5 mm vs 3.2 mm);
- A higher final energy (1170 MeV vs 1102 MeV);
- Being fully synergic with CompactLight, the design of both the projects would be faster.

The only drawback is that a longer active length is required (18 m vs 16 m).

5.4.1 RF module

Final parameters of the rf module with 90 cm structures are summarized in Table 5.25.

EuPRAXIA@SPARC_LAB's 3D layout of the rf module

The 3D layout of the rf module with 90 cm structures for EuPRAXIA@SPARC_LAB is shown in Figs. 5.59 and 5.60. It foresees three beam position monitors, 2 diagnostics/pump stations and three quadrupoles. Two different modules are foreseen: where the beam has a low energy and where the beam has a high energy. The only difference between them is the strength (and the length) of the quadrupoles. The first two modules in the linac are low-energy type, while the last three are high-energy type. The distances between the structures (calculated with formulas of Subsection 5.3.6) are L_1=1518.433 mm, L_2=1693.397 mm, L_3=1530.931 mm for the low-energy module and L_1=1718.392 mm, L_2=1893.355 mm, L_3=1730.889 mm for the high-energy module. Results are summarized in Table 5.26. The total lengths of the two types of modules are 6217.920 mm and 6844.820 mm, respectively. The total power attenuation of the waveguides, including the overmoded circular waveguide, has been estimated equal to 10% and 11%, respectively. The presented layout is still in a preliminary phase and improvements on its design are ongoing. For example, phase shifters for phase adjustments need to be put in it.

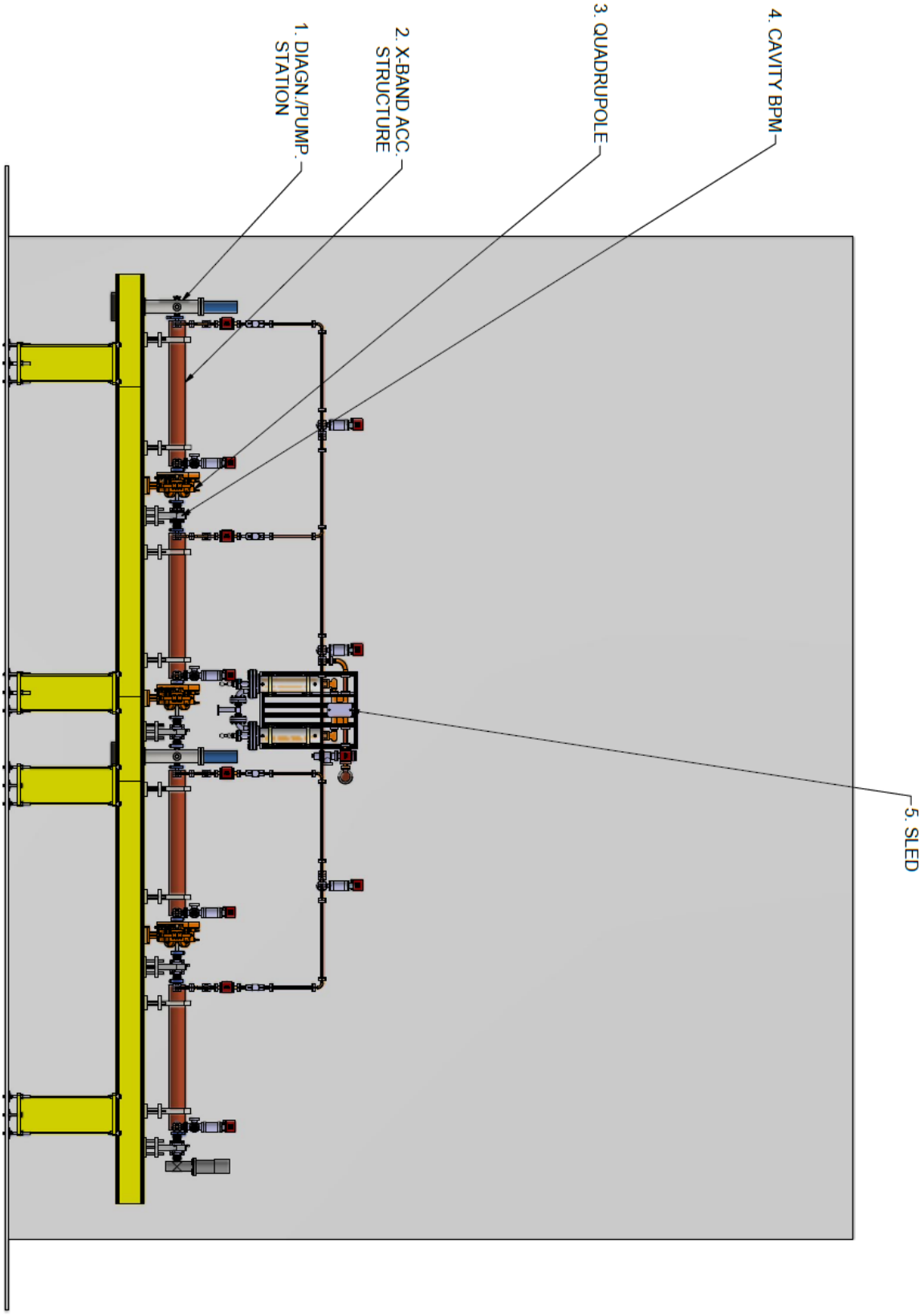

Figure 5.59. 3D layout of the EuPRAXIA@SPARC_LAB's rf module with 90 cm structures.

Table 5.25. Main parameters of the 90 cm structures adopted as baseline for EuPRAXIA@SPARC_LAB's and CompactLight's X-band boosters.

Parameter	Units	Value
Available klystron power	MW	∼40
Klystron pulse length	µs	1.5
Repetition rate f_{rep}	Hz	100
SLED Q_0		180000
SLED Q_e		23000
Structure length L_t	m	0.9
Number of cells N_c		108
Iris radius first-last cell a	mm	4.278-2.722
Normalized group velocity v_g/c	%	4.68-0.96
Filling time t_f	ns	144
Section attenuation τ_s		0.767
Shunt impedance r	MΩ/m	90-131
Q-factor Q		7152-7000
r/Q	kΩ/m	12.5-18.7
Effective shunt impedance r_s	MΩ/m	387
P_{out}/P_{in}		0.22
Average gradient $\langle G \rangle$	MV/m	65
Peak input power	MW	68
Input power averaged over the pulse	MW	44
Structures per module		4
Klystron power per module	MW	39

Table 5.26. Distances between the structures in the 90 cm rf module of EuPRAXIA@SPARC_LAB.

Parameter	Units	Low-energy	High-energy
L_1	mm	1518.433	1718.392
L_2	mm	1693.397	1893.355
L_3	mm	1530.931	1730.889

5.4.2 Wakefields and instabilities

Beam breakup calculations

Since the reference structure has been changed, preliminary beam breakup calculations have been performed for the EuPRAXIA@SPARC_LAB's working points. Using Eq. (5.2), the growth parameter Υ has been then calculated. Results are summarized in Table 5.27. Thanks to a larger average iris aperture and a higher average gradient (for Full rf case), the growth parameter is 1.57 for the PWFA case and 1.48 for the Full rf case. In both cases, it is lower than the half meter structure case, where Υ was 2.

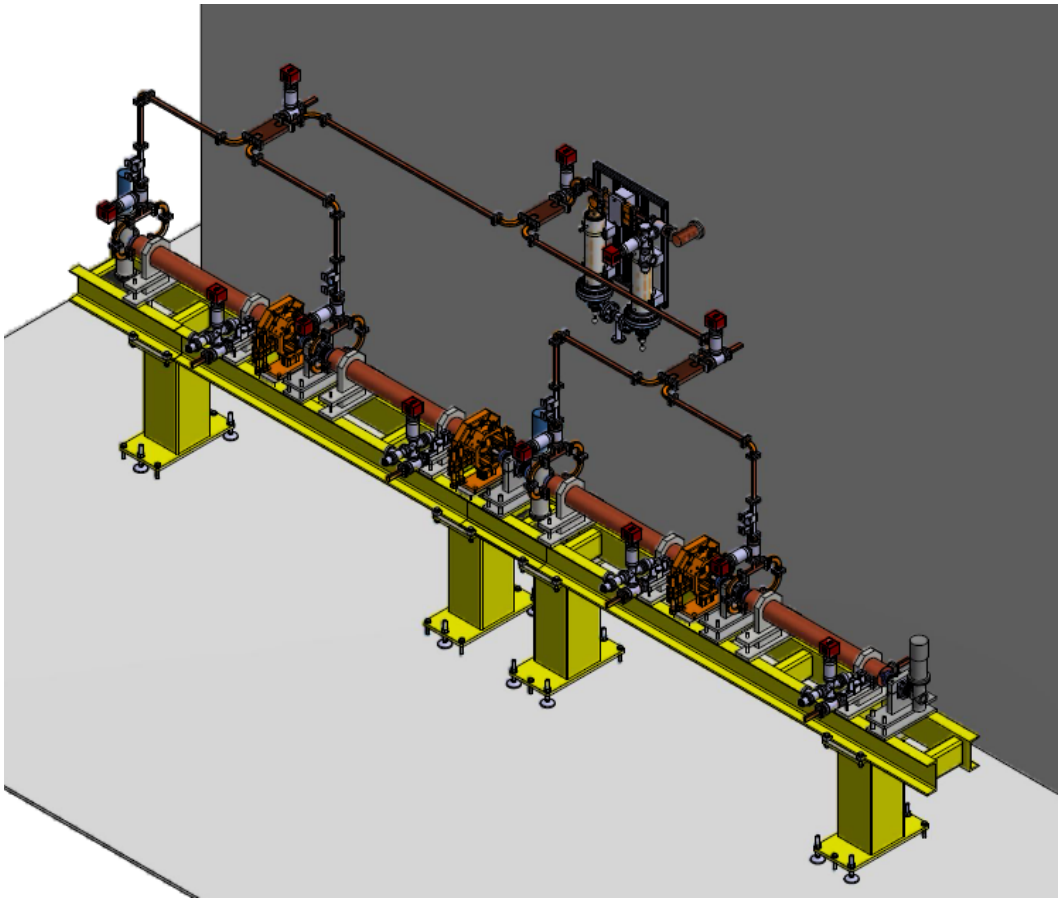

Figure 5.60. Another view of the 3D layout of the EuPRAXIA@SPARC_LAB's rf module with 90 cm structures.

Table 5.27. EuPRAXIA@SPARC_LAB's main parameters of Linac1 with 90 cm long structures.

Parameter	Units	PWFA	Full rf
W_0	MeV	102	171
W_{L1}	MeV	240	560
$\langle G \rangle$	MV/m	20	57
Charge	pC	200(D)	200
σ_z	µm	50(D)	112
$\langle \beta \rangle$	m	∼30	∼30
$\lvert \Upsilon \rvert$		1.57	1.48

Calculation of the wake function for beam dynamics simulations

As described in Subsection 5.2.2, once defined the design of the structure, beam breakup limits need to be found. To do this, the wake function of the structure has been found using the code ECHO [119–121]. ECHO calculates electromagnetic fields of charged bunches in accelerators. It is a collection of the following programs:

- ECHO1D which calculates impedances and wakes of rotationally symmetric and rectangular waveguides;
- ECHOz1, ECHOz2 and ECHO2D for rotationally symmetric and rectangular geometries;
- ECHO3D for arbitrary three dimensional structures.

In particular, code ECHO1D calculates in frequency domain the electromagnetic fields generated by an electron bunch passing through an anisotropic transversally non-homogeneous vacuum chamber of round or rectangular cross-section with translational symmetry in the beam direction.

Code ECHOz1 calculates in time domain the electromagnetic fields generated by an electron bunch passing through rotationally symmetric perfectly conducting structure on axis of symmetry.

Code ECHOz2 calculates in time domain the electromagnetic fields generated by an electron bunch passing through rotationally symmetric conducting structure off axis. The structure can have only metal conductive walls with finite or infinite conductivity.

Code ECHO2D calculates in time domain the electromagnetic fields generated by an electron bunch passing through rotationally symmetric or rectangular structures. The structure can consist of several materials with different permeabilities, permitivities and conductivities. The wall conductivity model for metals is available as well. This code has all possibilities of ECHOz1 and ECHOz2. Additionally, it is able to calculate wakefields in rectangular structures. The bunch form can be arbitrary and the bunch can have finite energy. At the current version there is possibility to do particle tracking for fully rotationally symmetric case.

Code ECHO3D calculates in time domain the electromagnetic fields generated by an electron bunch passing through arbitrary three dimensional chamber. The structure can consist of several materials with different permeabilities and permitivities. The volume and wall conductivity model for metals are not available. The bunch form is a Gaussian pencil bunch. The arbitrary bunch form is possible.

Considering our case, we used code ECHOz2. In Fig. 5.61, the geometry of the 90 cm structure that has been defined in ECHO is shown. The structure is tapered with parameters reported in Table 5.25. For EuPRAXIA@SPARC_LAB, we are interested in calculating the wake functions for the cases reported in Table 5.4: gaussian bunches with σ_z of 50 µm and 112 µm, respectively.

Outputs of this code are wake potentials. In Fig. 5.62, the transverse wake potentials for both the bunches are shown.

The default mesh size in ECHO is $\sigma_z/5$. In Fig. 5.63, a comparison of the

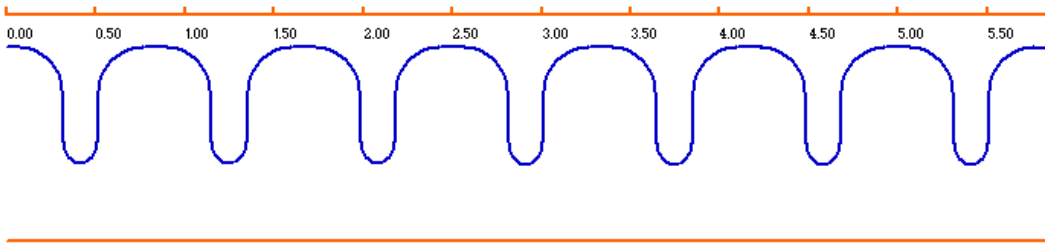

Figure 5.61. Geometry of the 90 cm structure that has been defined in ECHO.

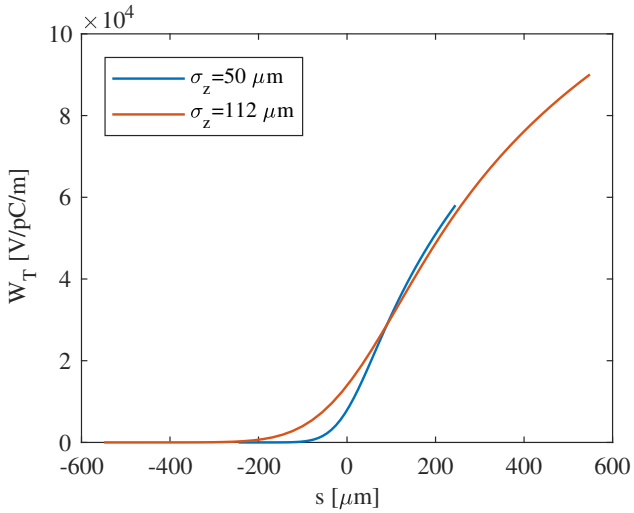

Figure 5.62. Wake potentials calculated with ECHO for two bunch lengths.

transverse wake potentials obtained with the default setting and a mesh size of $\sigma_z/10$ is shown for a short bunch (28 µm). It is possible to observe that the default setting gives excellent results.

Basically, there are two ways to find the wake function: calculating the Green function or fitting the Bane's formulas slightly changing its parameters. We opted for the second option. As described in Ref. [155], the short range transverse wake function can be approximated by the relation:

$$w_\perp(z) = \frac{4Z_0 c s_2 A}{\pi a^4}\left[1 - \left(1 + \sqrt{\frac{z}{s_2}}\right) e^{-\sqrt{\frac{z}{s_2}}}\right], \tag{5.47}$$

where A and s_2 are fit parameters to be defined.

With $A = 1.48$ and s_2 =9.948 $\times 10^{-5}$, it has been found a better agreement with the wake function obtained with ECHO, with respect to the Bane's formula of Eq. (4.10). Results are shown in Fig. 5.64. The fit has a good agreement, especially in the short range where we are interested in.

The obtained wake functions are shown in Fig. 5.65, where they are compared

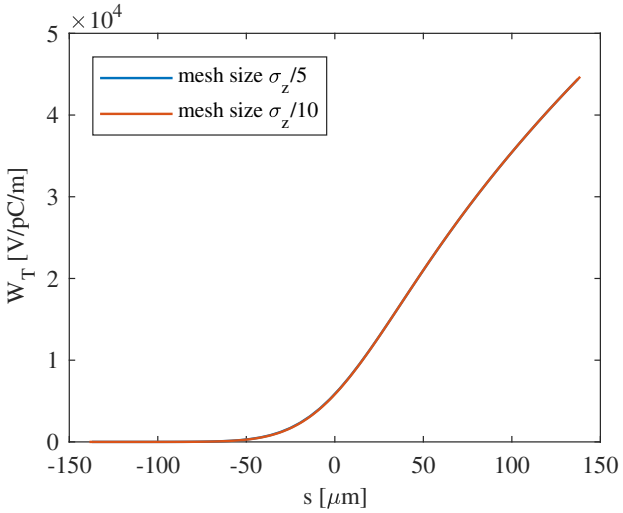

Figure 5.63. Comparison of the transverse wake potentials obtained with the default setting and a mesh size of $\sigma_z/10$ is shown for a short bunch (28 µm).

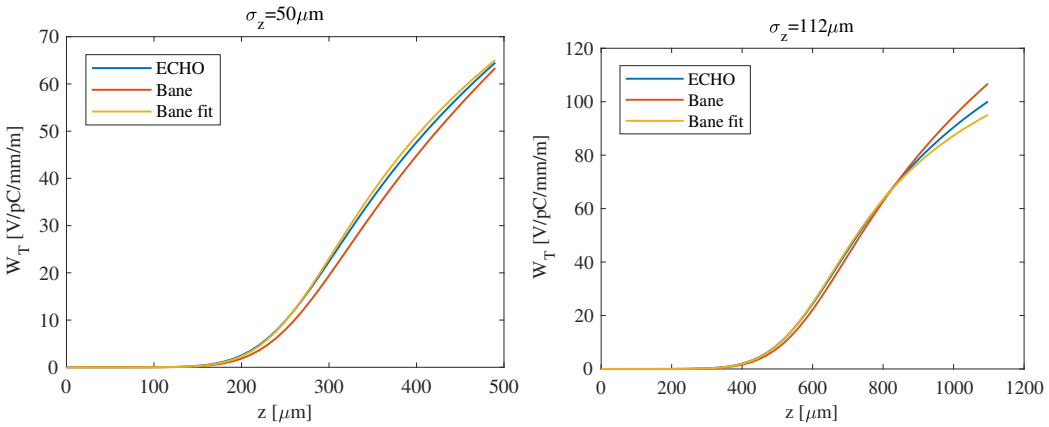

Figure 5.64. Comparison between wake functions obtained with ECHO, Bane's formula and fit for two bunch lengths.

with Bane's formulas. It is possible to observe that, in the short range, the fitted wake function is slightly higher than Bane's formula.

In the next future, the wake function of Eq. (5.47) will be used for beam dynamics simulations using the code ELEGANT.

5.4.3 Thermal analysis and preliminary design of the cooling system

As described in Section 5.1, another important step in the design of an accelerating structure is to perform thermo-mechanical simulations to design the cooling system.

As a first approach, we have calculated the *average dissipated power per structure*. It is defined as the integral of the structure input power $P_{in\,s}$ over the pulse, multiplied

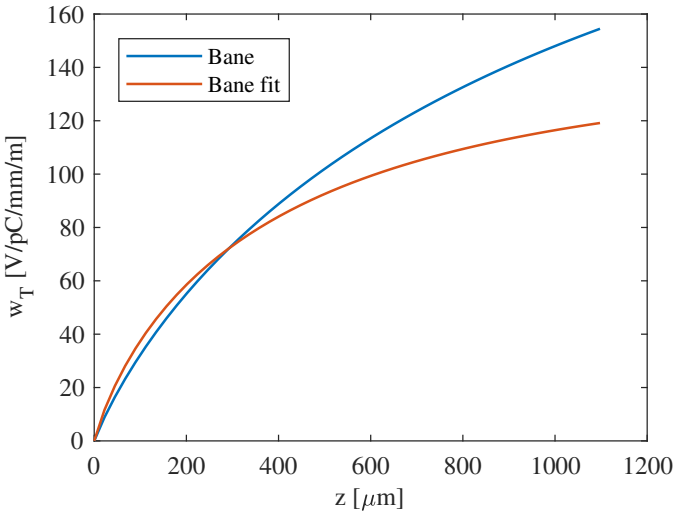

Figure 5.65. Comparison of the transverse wake functions: Bane versus fit from ECHO.

by the klystron repetition rate f_{rep} and the structure attenuation factor $1 - e^{-2\tau_s}$. In formulas:

$$P_{diss\,structure} = (1 - e^{-2\tau_s}) f_{rep} \int_{t_p} P_{in\,s} dt, \tag{5.48}$$

where t_p is the pulse time. The *average dissipated power per meter* is:

$$p_{diss\,structure} = \frac{P_{diss\,structure}}{L_s}, \tag{5.49}$$

where L_s is the structure length. And the *average dissipated power per cell* is:

$$P_{diss\,cell} = \frac{P_{diss\,structure}}{N_c}, \tag{5.50}$$

where N_c is the number of cells in one structure.

In Fig. 5.66, the power at the structure input port as function of time is shown. Thus, considering the plot of Fig. 5.66 and the parameters of Table 5.25, we obtained an average dissipated power per structure of 912 W that corresponds to ∼1 kW/m and an average dissipated power per cell of 8.4 W.

A preliminary design of the cooling system has been performed. It is based on 4 symmetric colling channels distributed around the cells. The cooling channels have a diameter of 8 mm. A 3D mechanical model of the regular cell with the main geometrical dimensions of the cooling channels is shown in Fig. 5.67.

Once defined the preliminary design of the cooling channels, a thermal analysis has been performed with the commercial code CST Studio Suite [124]. CST Studio Suite is a 3D EM analysis software package for designing, analyzing and optimizing electromagnetic components and systems. It integrates multiple electromagnetic

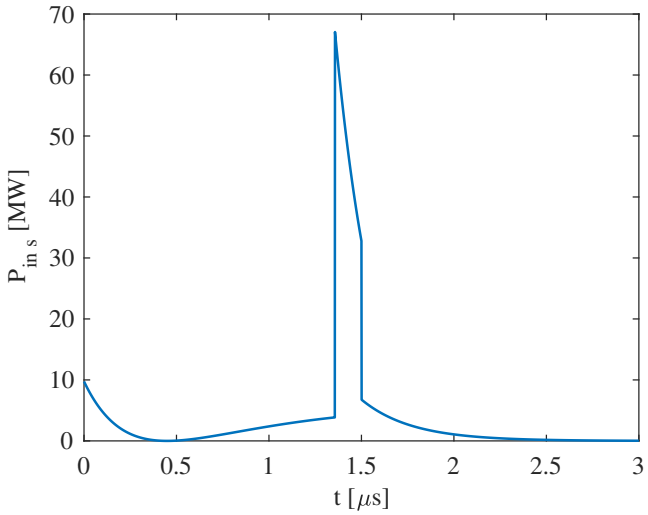

Figure 5.66. Power at the structure input port as function of time.

simulation solvers which use methods such as the finite element method (FEM) the finite integration technique (FIT), and the transmission line matrix method (TLM). In particular, the Conjugate Heat Transfer Solver combines thermal and fluid dynamics simulation methods, and can calculate the heating of a device while taking convection and fan cooling into consideration. Links to the EM and other multiphysics solvers allow the Thermal Transient Solver to be used to calculate electromagnetic heating of devices.

We have performed simulations with a water flux of 6 l/min in the cooling channels [156, 157] and a water temperature of 30°. With these parameters, we obtained a *maximum difference between the water temperature and the cell temperature* ΔT_w of ∼1.6° and a *maximum difference in temperature of the accelerating part of the cell* ΔT_c of ∼0.34°. According to the considerations of Subsection 5.2.8, the cell resonance frequency (and then its phase advance per cell) can be tuned adjusting the water temperature. Thus, as a first approximation, the only parameter that can contribute to the cell detuning is ΔT_c. In Fig. 5.68, the temperature distribution on the cell is shown.

The mechanical errors introduced by a non uniform temperature over the cell can be calculated considering the thermal expansion of solids. The *thermal expansion* is the tendency of matter to change its shape, area, and volume in response to a change in temperature [158]. If the body is free to expand, the expansion or strain resulting from an increase in temperature can be simply calculated by using the applicable coefficient of thermal expansion. Linear expansion means change in one dimension (length) as opposed to change in volume (volumetric expansion). To a first approximation, the change in length measurements of an object due to

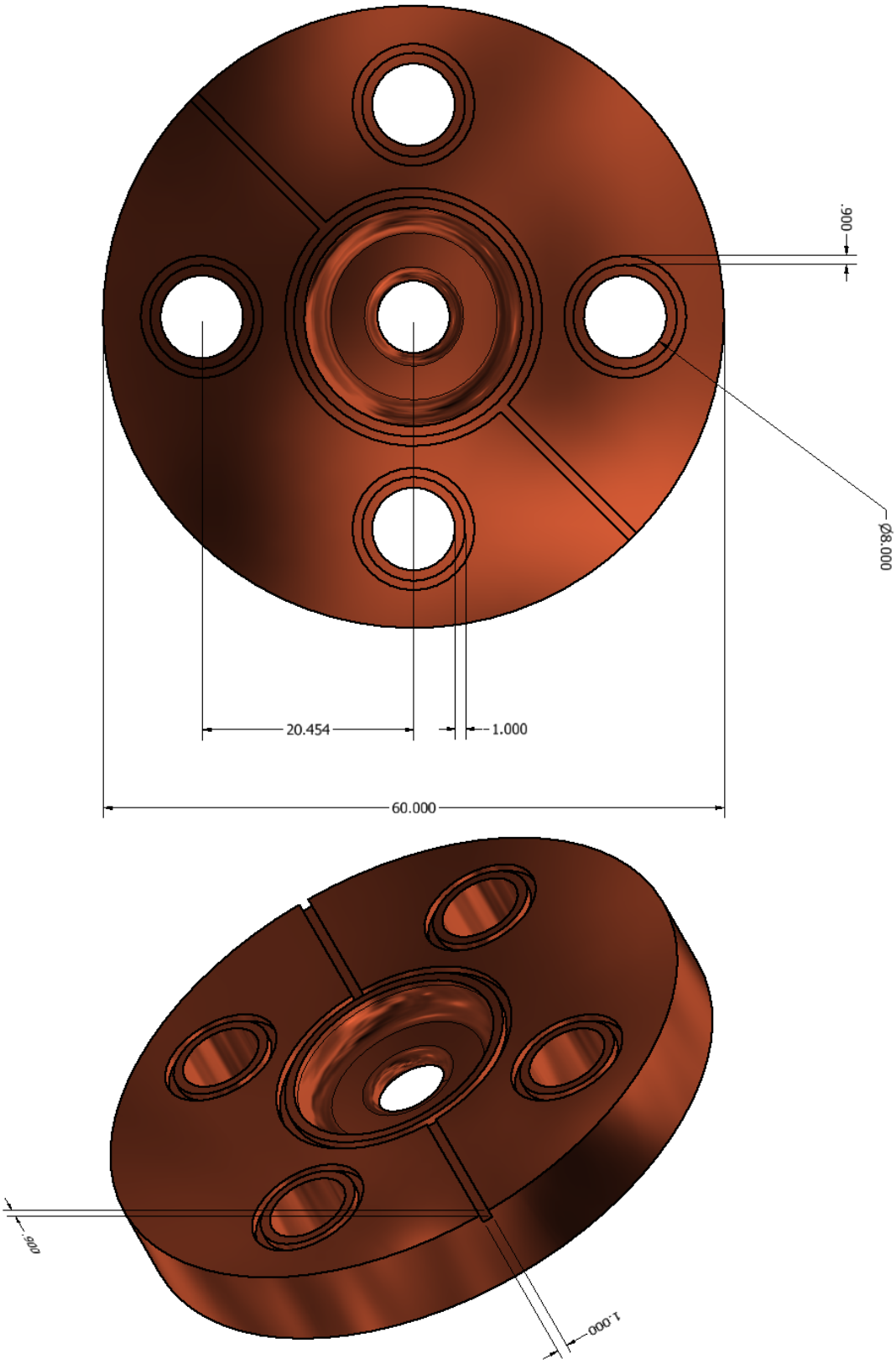

Figure 5.67. 3D mechanical model of the regular cell with the main geometrical dimensions of the cooling channels.

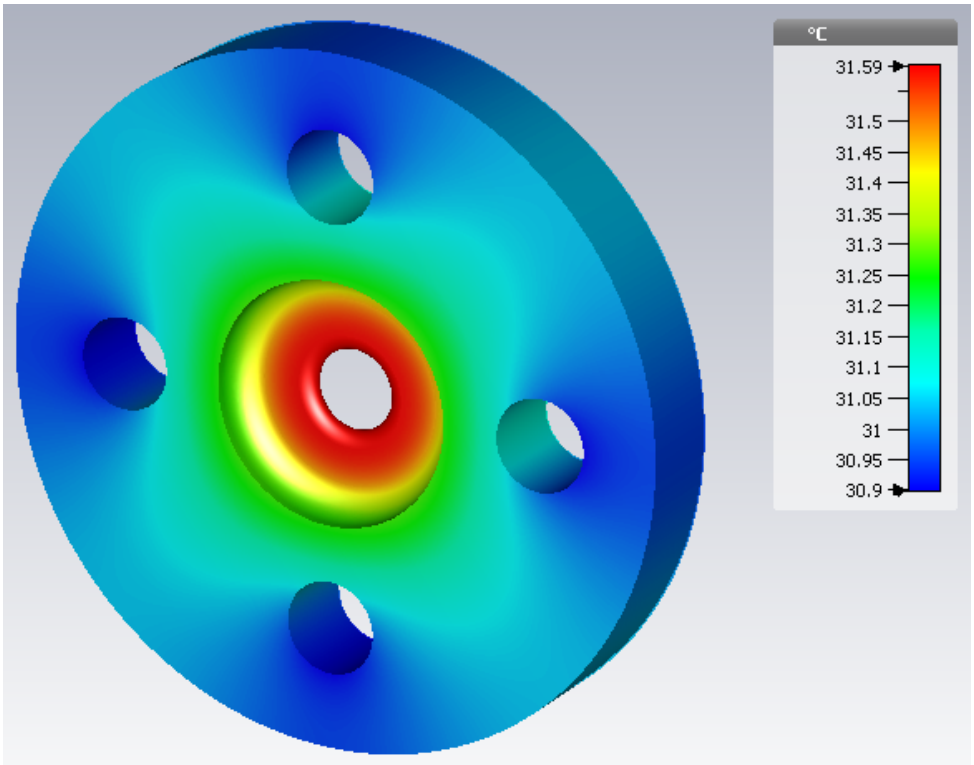

Figure 5.68. Temperature distribution on the cell (100 Hz, four cooling channels).

thermal expansion is related to temperature change by a *coefficient of linear thermal expansion (CLTE)* α_L. It is the fractional change in length per degree of temperature change. Assuming negligible effect of pressure, the change in the linear dimension can be estimated to be:

$$\frac{\Delta L}{L} = \alpha_L \Delta T. \tag{5.51}$$

This estimation works well as long as the linear-expansion coefficient does not change much over the change in temperature ΔT, and the fractional change in length is small $\Delta L/L \ll 1$. If either of these conditions does not hold, the exact differential equation (using dL/dT) must be integrated. For copper, CLTE is $17 \times 10^{-6}\,\mathrm{K}^{-1}$ at 20 °C. Thus, from Eq. (5.51), a change in temperature of 0.3 °C between b and a gives a ΔL of:

$$\Delta L = \alpha_L \Delta T(b-a) = 17 \cdot 10^{-6} \cdot 0.3 \cdot 7.044 \cdot 10^{-3} = 0.036\ \mu\mathrm{m}. \tag{5.52}$$

According to Table 5.8, this value corresponds to a change in the cell phase advance of 0.012°. Thus, this is the average intrinsic detuning of the cell due to a non uniform temperature distribution. Hence, considering the same detuning for each cell, the total detuning of the structure is ∼1.3°.

Furthermore, one has to also take into account the stability of water temperature. Considering a water temperature with a precision of 0.1 °C, we obtain, in the worst case, a detuning of the cell of 0.004° and a total detuning of the structure <0.5°. Adding this value to the 1.3° calculated before, we obtain a total detune of the structure <1.8°, a value more than acceptable, according to the considerations of Subsection 5.2.8.

For the high repetition rate configuration, explained in Subsection 5.3.7, the maximum achievable accelerating gradient is 30.4 MV/m at 1 kHz, requiring a klystron power per module of 8.5 MW. The peak input power per structure is 14.8 MW, which gives an average dissipated power per structure of 1997 W that corresponds to ∼2.2 kW/m and an average dissipated power per cell of 18.5 W, more or less twice the power of the 100 Hz case. With these parameters, a thermal analysis of the cell has been performed keeping the same water flow of the previous case. Results are shown in Fig. 5.69. In this case, we obtained a maximum difference between the water temperature and the cell temperature ΔT_w of ∼3.5 °C and a maximum difference in temperature of the accelerating part of the cell ΔT_c of ∼0.7 °C. Thus, from Eq. (5.51), a change in temperature of 0.7 °C between b and a gives a ΔL of 0.084 µm. According to Table 5.8, this value corresponds to a change in the cell phase advance of 0.028° and a detune of the structure of ∼3°. Considering also the water temperature stability, we obtain a total detune of the structure of ∼3.5°.

In order to reduce the difference between the water temperature and the cell temperature in the 1 kHz operating mode and obtain a more uniform temperature distribution, a new cooling system has been designed. It is made up of eight symmetric cooling channels of 8 mm diameter each. With this geometry, and keeping the same water flow, we obtained the results of Fig. 5.70. The maximum difference between the water temperature and the cell temperature ΔT_w is ∼2.4 °C (∼1 °C lower than the presious geometry) and the maximum difference in temperature of the accelerating part of the cell is still ΔT_c of ∼0.7 °C. Thus, the detuning of the cell, due to the non constant temperature along the iris, is the same. On the other hand, due to the presence of eight cooling channels, the temperature distribution is more uniform. Mechanical drawings of the new solution are shown in Fig. 5.71.

Concluding, the geometry with eight cooling channels seems preferable, with respect to the one with four channels, due to its thermal uniformity. We remark that this mechanical design study has been just started and many different solutions will be studied in the next future.

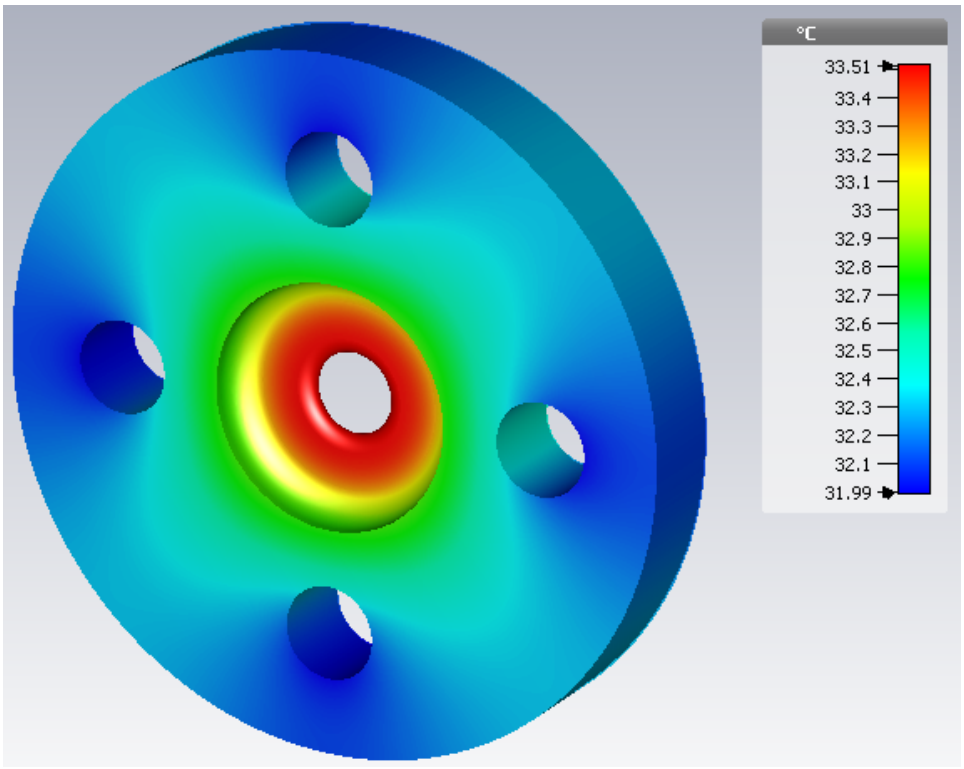

Figure 5.69. Temperature distribution on the cell (1 kHz, four cooling channels).

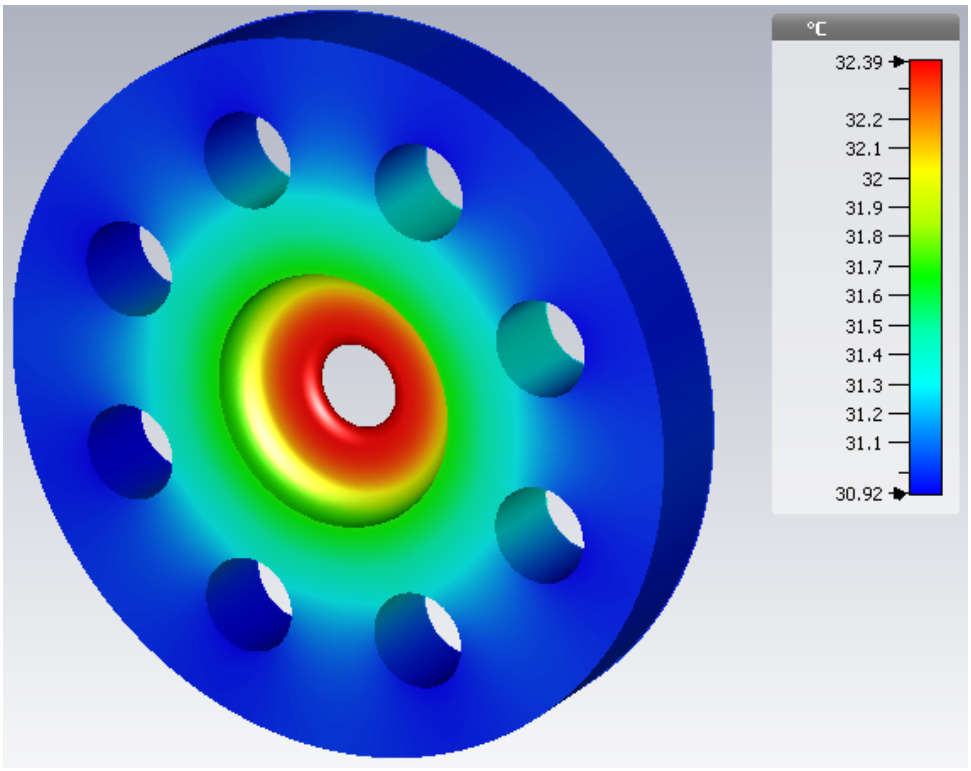

Figure 5.70. Temperature distribution on the cell (1 kHz, eight cooling channels).

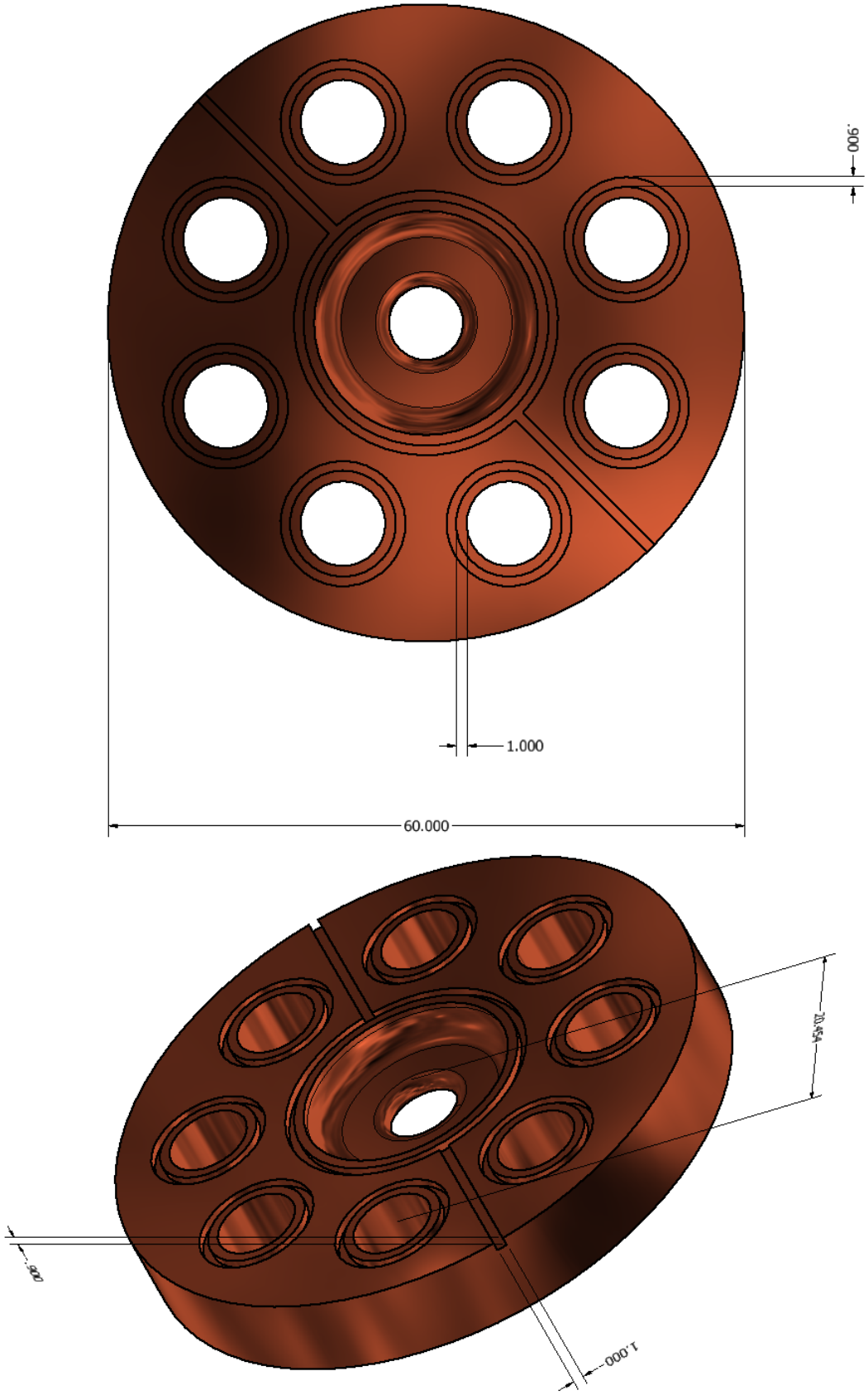

Figure 5.71. 3D mechanical model of the regular cell with eight cooling channels.

Chapter 6

Conclusions and outlook

The design of the linacs for the EuPRAXIA@SPARC_LAB and CompactLight projects has been performed. For both the projects, the goal is to design a compact and cost effective FEL driven by an X-band linac. For EuPRAXIA@SPARC_LAB, the linac has to provide an energy gain of ∼1.2 GeV in 18 m of active length while, for CompactLight, the linac has to provide ∼5.2 GeV in 83 m of active length. The linacs are based on traveling wave structures operating on the $2\pi/3$ mode, fed by klystrons and pulse compressors.

The design of the cells, the couplers and the structures has been done keeping into account all the main parameters that allows to predict the breakdown rate like surface electric field, modified Poynting vector, pulsed heating and having a high rf efficiency. The structures are designed to operate at an accelerating gradient of 65 MV/m with a breakdown rate below 10^{-6} bpp/m.

The design of the structures has been done using analytical formulas and writing a numerical tool able to find the optimal structure length and tapering of the irises in terms of rf efficiency and breakdown probability. The optimal solution has been found to be 90 cm long tapered structures with an average iris radius of 3.5 mm.

Racetrack rf power couplers have been designed giving a low reflection coefficient at the input port and minimizing the multipolar field components up to a factor 10 with respect to a circular geometry.

A preliminary evaluation of the beam breakup instabilities has been performed with the tracking particle code ELEGANT using Bane's formula, giving the result of an optimal beam stay-clear along the linac. Calculation of the wake function has been performed using the ECHO code fitting Bane's formula. The obtained wave function will be used in ELEGANT for more accurate beam dynamics simulations.

The linacs are made up of a repetition of rf modules. Each one has 4 traveling wave structures, 1 SLED and one 50 MW peak power klystron for the 100 Hz configuration.

A preliminary study on the high repetition rate operations with current and future power sources has been also performed. The linacs can operate at 1 kHz lowering the accelerating gradient to ∼23 MV/m using currently available 6 MW peak power 400 Hz klystrons or lowering the gradient to ∼30 MV/m using 10 MW peak power 1 kHz klystrons available in the next future.

A preliminary mechanical design of the cells has then been performed in combination of a thermal analysis. The cells have been designed to have 8 symmetric cooling channels with a diameter of 8 mm, giving an overall thermal uniformity in it.

The waveguide network for power distribution has also been designed. It is a simple binary tree layout. This type of networks reduce the overall rf efficiency due to delays in the structure injections. The rf power delay distribution has been optimized giving as a result only ∼2% of reduction of accelerating gradient.

Once the design of the structures will be finalized, first prototypes will be fabricated and low-power and high-power tests will be performed.

Bibliography

[1] T. P. Wangler, "Introduction to linear accelerators," Los Alamos National Laboratories, Tech. Rep. LA-UR-93-805, 1993.

[2] U. Amaldi, "The importance of particle accelerators," *europhysics news*, vol. 31, no. 6, pp. 5–9, 2000.

[3] W. Utsumi, K.-I. Funakoshi, S. Urakawa, M. Yamakata, K. Tsuji, H. Konishi, and O. Shimomura, "SPring-8 beamlines for high pressure science with multi-anvil apparatus," *The Review of High Pressure Science and Technology*, vol. 7, pp. 1484–1486, 1998.

[4] *SPring-8 website*, `http://www.spring8.or.jp/en/`.

[5] D. Moncton, E. Crosbie, and G. Shenoy, "Overview of the advanced photon source," *Review of Scientific Instruments*, vol. 60, no. 7, pp. 1403–1405, 1989.

[6] *APS website*, `https://www.aps.anl.gov/`.

[7] K. Balewski, R. Rohlsberger, H. Franz, E. Weckert, W. Decking, and W. Brefeld, "Petra iii: A low emittance synchrotron radiation source. technical design report," Tech. Rep., 2004.

[8] *PETRA III website*, `http://photon-science.desy.de/facilities/petra_iii/index_eng.html`.

[9] R. Haensel, "European Synchrotron Radiation Facility (ESRF)," *Review of scientific instruments*, vol. 63, no. 1, pp. 1571–1572, 1992.

[10] *ESRF website*, `https://www.esrf.eu/`.

[11] B. W. Batterman and N. W. Ashcroft, "CHESS: The new synchrotron radiation facility at Cornell," *Science*, vol. 206, no. 4415, pp. 157–161, 1979.

[12] *CHESS website*, `https://www.chess.cornell.edu/`.

[13] J. Arthur, G. Materlik, R. Tatchyn, and H. Winick, "The LCLS: A fourth generation light source using the SLAC linac," *Review of scientific instruments*, vol. 66, no. 2, pp. 1987–1989, 1995.

[14] *LCLS website*, `https://lcls.slac.stanford.edu/`.

[15] M. Altarelli, R. Brinkmann, M. Chergui, W. Decking, B. Dobson, S. Düsterer, G. Grübel, W. Graeff, H. Graafsma, J. Hajdu, *et al.*, "The European x-ray free-electron laser technical design report," Tech. Rep., 2006.

[16] *European XFEL website*, `https://www.xfel.eu/index_eng.html`.

[17] I. Ko, H.-S. Kang, H. Heo, C. Kim, G. Kim, C.-K. Min, H. Yang, S. Baek, H.-J. Choi, G. Mun, *et al.*, "Construction and commissioning of PAL-XFEL facility," *Applied Sciences*, vol. 7, no. 5, p. 479, 2017.

[18] *PAL-XFEL website*, `http://pal.postech.ac.kr/paleng/`.

[19] M. Yabashi, H. Tanaka, and T. Ishikawa, "Overview of the SACLA facility," *Journal of synchrotron radiation*, vol. 22, no. 3, pp. 477–484, 2015.

[20] *SACLA website*, `http://xfel.riken.jp/eng/`.

[21] C. Milne, T. Schietinger, M. Aiba, A. Alarcon, J. Alex, A. Anghel, V. Arsov, C. Beard, P. Beaud, S. Bettoni, *et al.*, "SwissFEL: the Swiss X-ray free electron laser," *Applied Sciences*, vol. 7, no. 7, p. 720, 2017.

[22] *SwissFEL website*, `https://www.psi.ch/de/swissfel`.

[23] Y. Ohnishi, T. Abe, T. Adachi, K. Akai, Y. Arimoto, K. Ebihara, K. Egawa, J. Flanagan, H. Fukuma, Y. Funakoshi, *et al.*, "Accelerator design at SuperKEKB," *Progress of Theoretical and Experimental Physics*, vol. 2013, no. 3, 2013.

[24] *SuperKEKB website*, `http://www-superkekb.kek.jp/`.

[25] Z. Chuang, "BEPC II: construction and commissioning," *Chinese Physics C*, vol. 33, no. S2, p. 60, 2009.

[26] *BEPC II website*, `http://english.ihep.cas.cn/doc/1840.html`.

[27] V. Anashin, O. Anchugov, A. Bondar, A. Dubrovin, P. Durnov, M. Formin, Y. Gluhovchenko, E. Gorniker, A. Kalinin, S. Karnaev, *et al.*, "VEPP-4M collider: Status and plans," in *Proc. of EPAC98*, vol. 98, 1998, p. 400.

[28] V. Kiselev *et al.*, "Particle and Accelerator Physics at the VEPP-4M Collider," 2014.

[29] C. Milardi, D. Alesini, M. Biagini, R. Boni, M. Boscolo, F. Bossi, B. Buonomo, A. Clozza, G. Delle Monache, T. Demma, E. Di Pasquale, G. Di Pirro, A. Drago, A. Gallo, A. Ghigo, S. Guiducci, C. Ligi, F. Marcellini, G. Mazzitelli, F. Murtas, and L. Pellegrino, "Crab Waist Collision at DAFNE," *ICFA Beam Dynamics Newsletter*, vol. 48, pp. 23–33, Nov. 2011.

[30] *DAΦNE website*, `http://w3.lnf.infn.it/accelerators/dafne/?lang=en`.

[31] C. Travier, "Rewiev of microwave guns," *Particle Accelators*, vol. 36, pp. 33–74, 1991.

[32] C. Travier, "Review of electron guns," in *European Particle Accelerator Conference 4 Epac 94*, World Scientific, 1994, pp. 317–321.

[33] J. Power, "Overview of photoinjectors," in *AIP Conference Proceedings*, AIP, vol. 1299, 2010, pp. 20–28.

[34] T. Rao and D. H. Dowell, "An engineering guide to photoinjectors," *arXiv preprint arXiv:1403.7539*, 2014.

[35] M. Ferrario, "Low emittance photoinjectors," *Nuclear Instruments and Methods in Physics Research Section A: Accelerators, Spectrometers, Detectors and Associated Equipment*, vol. 472, no. 1-2, pp. 303–308, 2001.

[36] G. Kube, "Specific diagnostics needs for different machines," in *Proceedings of the CAS-CERN Accelerator School: Beam Diagnostics, Dourdan, France, 28 May - 6 June 2008, CERN-2009-005*, 2009.

[37] T. P. Wangler, *RF Linear Accelerators*. John Wiley & Sons, 2008.

[38] W. Wuensch, "High-gradient breakdown in normal-conducting RF cavities," in *Proceedings of EPAC 2002, Paris, France*, 2002.

[39] D. Dowell, E. Jongewaard, C. Limborg-Deprey, J. Schmerge, Z. Li, L. Xiao, J. Wang, J. Lewandowski, and A. Vlieks, "Results of the SLAC LCLS gun high-power RF tests," in *2007 IEEE Particle Accelerator Conference (PAC)*, IEEE, 2007, pp. 1296–1298.

[40] M. Borland, "Cavity design and beam simulations for the aps rf gun," Argonne National Lab., Tech. Rep., 1991.

[41] M. Satoh *et al.*, "Commissioning Status of SuperKEKB Injector Linac," in *Proc. of International Particle Accelerator Conference (IPAC'16), Busan, Korea, May 8-13, 2016*, (Busan, Korea), ser. International Particle Accelerator Conference, doi:10.18429/JACoW-IPAC2016-THPOY027, Geneva, Switzerland: JACoW, Jun. 2016, pp. 4152–4154, ISBN: 978-3-95450-147-2. DOI: doi:10.18429/JACoW-IPAC2016-THPOY027. [Online]. Available: http://jacow.org/ipac2016/papers/thpoy027.pdf.

[42] J.-Y. Raguin, M. Bopp, A. Citterio, and A. Scherer, "The Swiss FEL RF Gun: RF Design and Thermal Analysis," in *Proceedings, 26th International Linear Accelerator Conference (LINAC12): Tel Aviv, Israel, September 9-14, 2012*, 2013, TUPB010. [Online]. Available: http://accelconf.web.cern.ch/AccelConf/LINAC2012/papers/tupb010.pdf.

[43] L. D. S. Group *et al.*, "LCLS Design Study Report," SLAC, Tech. Rep., 1998.

[44] M. White, N. Arnold, and W. Berg, "Construction, Commissioning and Operational Experience of the Advanced Photon Source (APS) Linear Accelerator," Argonne National Lab., Tech. Rep., 1996.

[45] H. Franz, O. Leupold, R. Röhlsberger, S. Roth, O. Seeck, J. Spengler, J. Strempfer, M. Tischer, J. Viefhaus, E. Weckert, *et al.*, "Technical report: Petra iii: Desy's new high brilliance third generation synchrotron radiation source," *Synchrotron Radiation News*, vol. 19, no. 6, pp. 25–29, 2006.

[46] J. H. Han, H. .-.-S. Kang, and I. S. Ko, "Status of the PAL-XFEL Project," *Conf. Proc.*, vol. C1205201, pp. 1735–1737, 2012.

[47] T. Inagaki, C. Kondo, H. Maesaka, T. Ohshima, Y. Otake, T. Sakurai, K. Shirasawa, and T. Shintake, "High-gradient C-band linac for a compact x-ray free-electron laser facility," *Physical Review Special Topics-Accelerators and Beams*, vol. 17, no. 8, p. 080 702, 2014.

[48] R. Zennaro, J. Alex, A. Citterio, and J.-Y. Raguin, "Measurements and high power test of the first C-band accelerating structure for SwissFEL," in *Proceedings, 27th Linear Accelerator Conference, LINAC2014*, 2014, MOPP119.

[49] J. Galayda, "The Linac Coherent Light Source-II Project," in *Proc. 5th International Particle Accelerator Conference (IPAC'14), Dresden, Germany, June 15-20, 2014*, (Dresden, Germany), ser. International Particle Accelerator Conference, https://doi.org/10.18429/JACoW-IPAC2014-TUOCA01, Geneva, Switzerland: JACoW, Jul. 2014, pp. 935–937, ISBN: 978-3-95450-132-8. DOI: `https://doi.org/10.18429/JACoW-IPAC2014-TUOCA01`. [Online]. Available: `http://jacow.org/ipac2014/papers/tuoca01.pdf`.

[50] C. Christou, ""x-band linac technology for a high repetition rate light source"," *Nuclear Instruments and Methods in Physics Research Section A: Accelerators, Spectrometers, Detectors and Associated Equipment*, vol. 657, no. 1, pp. 13–21, 2011. DOI: `https://doi.org/10.1016/j.nima.2011.06.050`.

[51] D. Broemmelsiek, B. Chase, D. Edstrom, E. Harms, J. Leibfritz, S. Nagaitsev, Y. Pischalnikov, A. Romanov, J. Ruan, W. Schappert, *et al.*, "Record high-gradient srf beam acceleration at fermilab," *New Journal of Physics*, vol. 20, no. 11, p. 113 018, 2018.

[52] M. Ferrario, D. Alesini, M. P. Anania, M. Artioli, A. Bacci, S. Bartocci, R. Bedogni, M. Bellaveglia, A. Biagioni, F. Bisesto, F. Brandi, E. Brentegani, F. Broggi, B. Buonomo, P. L. Campana, G. Campogiani, C. Cannaos, S. Cantarella, F. Cardelli, M. Carpanese, M. Castellano, G. Castorina, N. C. Lasheras, E. Chiadroni, A. Cianchi, R. Cimino, F. Ciocci, D. Cirrincione, G. A. Cirrone, R. Clementi, M. Coreno, R. Corsini, M. Croia, A. Curcio,

G. Costa, C. Curatolo, G. Cuttone, S. Dabagov, G. Dattoli, G. D'Auria, I. Debrot, M. Diomede, A. Drago, D. Di Giovenale, S. D. Mitri, G. Di Pirro, A. Esposito, M. Faiferri, L. Ficcadenti, F. Filippi, O. Frasciello, A. Gallo, A. Ghigo, L. Giannessi, A. Giribono, L. Gizzi, A. Grudiev, S. Guiducci, P. Koester, S. Incremona, F. Iungo, L. Labate, A. Latina, S. Licciardi, V. Lollo, S. Lupi, R. Manca, A. Marcelli, M. Marini, A. Marocchino, M. Marongiu, V. Martinelli, C. Masciovecchio, C. Mastino, A. Michelotti, C. Milardi, V. Minicozzi, F. Mira, S. Morante, A. Mostacci, F. Nguyen, S. Pagnutti, L. Pellegrino, A. Petralia, V. Petrillo, L. Piersanti, S. Pioli, D. Polese, R. Pompili, F. Pusceddu, A. Ricci, R. Ricci, R. Rochow, S. Romeo, J. B. Rosenzweig, M. R. Conti, A. R. Rossi, U. Rotundo, L. Sabbatini, E. Sabia, O. S. Plannell, D. Schulte, J. Scifo, V. Scuderi, L. Serafini, B. Spataro, A. Stecchi, A. Stella, V. Shpakov, F. Stellato, E. Turco, C. Vaccarezza, A. Vacchi, A. Vannozzi, A. Variola, S. Vescovi, F. Villa, W. Wuensch, A. Zigler, and M. Zobov, "EuPRAXIA@SPARC_LAB Design study towards a compact FEL facility at LNF," *Nuclear Instruments and Methods in Physics Research, Section A: Accelerators, Spectrometers, Detectors and Associated Equipment*, 2018, ISSN: 01689002. DOI: 10.1016/j.nima.2018.01.094.

[53] G. D'Auria *et al.*, "The CompactLight Design Study Project," in *Proc. 10th International Partile Accelerator Conference (IPAC'19), Melbourne, Australia, 19-24 May 2019*, (Melbourne, Australia), ser. International Particle Accelerator Conference, Geneva, Switzerland: JACoW Publishing, Jun. 2019, pp. 1756–1759, ISBN: 978-3-95450-208-0. DOI: doi:10.18429/JACoW-IPAC2019-TUPRB032.

[54] "International Study Group Progress Report On Linear Collider Development," Tech. Rep. SLAC-Report-559 and KEK Report 2000-7, 2000.

[55] "GLC Project," High Energy Accelerator Research Organization (KEK), Tsukuba, Japan, Tech. Rep. KEK-Report-2003-7.

[56] J. Wang, "Accelerator structure development for NLC/GLC," Stanford Linear Accelerator Center, Menlo Park, CA (US), Tech. Rep., 2004.

[57] T. Higo, R. Zennaro, C. Adolphsen, L. Laurent, S. Dobert, A. Grudiev, G. Riddone, A. Jensen, J. Wang, S. Tantawi, *et al.*, "Advances in X-band TW Accelerator Structures Operating in the 100 MV/m Regime," in *1st International Particle Accelerator Conference, IPAC'10, May 23 - 28, 2003, Kyoto, Japan*, vol. 100523, 2010, THPEA013.

[58] W. Wuensch, "Advances in high-gradient accelerating structures and in the understanding gradient limits," in *Proceedings of IPAC2017, Copenhagen,*

Denmark, 14-19 May, 2017, (Copenhagen, Denmark), ser. International Particle Accelerator Conference, https://doi.org/10.18429/JACoW-IPAC2017-MOYCA1, Geneva, Switzerland: JACoW, May 2017, pp. 24–29, ISBN: 978-3-95450-182-3. DOI: https://doi.org/10.18429/JACoW-IPAC2017-MOYCA1. [Online]. Available: http://jacow.org/ipac2017/papers/moyca1.pdf.

[59] V. A. Dolgashev, "Progress on high-gradient structures," *AIP Conf. Proc.*, vol. 1507, no. 1, pp. 76–84, 2012. DOI: 10.1063/1.4773679.

[60] V. Dolgashev, "High gradient, X-band and above, metallic RF structures," in *2nd European Advanced Accelerator Concepts Workshop, EAAC 2015, La Biodola, Isola d'Elba, Italy*, 2015. [Online]. Available: https://agenda.infn.it/event/8146/contributions/71603/attachments/51963/61378/Dolgashev_EAAC2012_High_gradient_metallic_structures_final_14Sep2015.pdf.

[61] C. Adolphsen, "Normal-conducting rf structure test facilities and results," in *Proceedings of the 2003 particle accelerator conference*, IEEE, vol. 1, 2003, pp. 668–672.

[62] S. Dobert, C. Adolphsen, G. Bowden, D. Burke, J. Chan, V. Dolgashev, J. Frisch, K. Jobe, R. Jones, J. Lewandowski, *et al.*, "High gradient performance of NLC/GLC X-band accelerating structures," in *Proceedings of the 2005 particle accelerator conference*, IEEE, 2005, pp. 372–374.

[63] J. Wang, "R&d; of accelerator structures at slac," *High Energy Phys. Nucl. Phys.*, vol. 30, no. SLAC-PUB-12293, pp. 11–15, 2006.

[64] E. I. Simakov, V. A. Dolgashev, and S. G. Tantawi, "Advances in high gradient normal conducting accelerator structures," *Nuclear Instruments and Methods in Physics Research Section A: Accelerators, Spectrometers, Detectors and Associated Equipment*, vol. 907, pp. 221–230, 2018. DOI: https://doi.org/10.1016/j.nima.2018.02.085.

[65] W. Kilpatrick, "Criterion for vacuum sparking designed to include both rf and dc," *Review of Scientific Instruments*, vol. 28, no. 10, pp. 824–826, 1957.

[66] V. A. Dolgashev, "High magnetic fields in couplers of X-band accelerating structures," in *Proceedings of the 2003 Particle Accelerator Conference*, IEEE, vol. 2, 2003, pp. 1267–1269.

[67] W. Wuensch, "The scaling of the traveling-wave rf breakdown limit," Tech. Rep. CERN-AB-2006-013, 2006.

[68] A. Grudiev, S. Calatroni, and W. Wuensch, "New local field quantity describing the high gradient limit of accelerating structures," *Physical Review Special Topics-Accelerators and Beams*, vol. 12, no. 10, p. 102 001, 2009.

[69] K. N. Sjobak, A. Grudiev, and E. Adli, "New Criterion for Shape Optimization of Normal-Conducting Accelerator Cells for High-Gradient Applications," in *Proceedings, 27th Linear Accelerator Conference, LINAC2014*, 2014, MOPP028.

[70] E. Jensen, "Fabrication and testing of rf structures," in *Physics And Technology Of Linear Accelerator Systems*, World Scientific, 2004, pp. 130–154.

[71] V. Dolgashev, L. Faillace, B. Spataro, and R. Bonifazi, "Innovative compact braze-free accelerating cavity," *Journal of Instrumentation*, vol. 13, no. 09, P09017–P09017, Sep. 2018. DOI: 10.1088/1748-0221/13/09/p09017. [Online]. Available: https://doi.org/10.1088%2F1748-0221%2F13%2F09%2Fp09017.

[72] V. Dolgashev, "Building and High Power Testing Welded Accelerating Structures," in *12th International Workshop on Breakdown Science and High-Gradient Technology, HG2019, from 10 to 14 June 2019, Chamonix, France*, 2019.

[73] B. Spataro, "Achievements on the X Band technological activity at INFN-LNF," in *12th International Workshop on Breakdown Science and High-Gradient Technology, HG2019, from 10 to 14 June 2019, Chamonix, France*, 2019.

[74] H. Zha, V. Dolgashev, and A. Grudiev, "RF Design of the CLIC Structure Prototype Optimized for Manufacturing from Two Halves," in *Proc. 6th International Particle Accelerator Conference (IPAC'15), Richmond, VA, USA, May 3-8, 2015*, (Richmond, VA, USA), ser. International Particle Accelerator Conference, https://doi.org/10.18429/JACoW-IPAC2015-TUPTY054, Geneva, Switzerland: JACoW, Jun. 2015, pp. 2147–2149, ISBN: 978-3-95450-168-7. DOI: https://doi.org/10.18429/JACoW-IPAC2015-TUPTY054. [Online]. Available: http://jacow.org/ipac2015/papers/tupty054.pdf.

[75] A. Grudiev and W. Wuensch, "A newly designed and optimized CLIC main linac accelerating structure," in *Linear accelerator. Proceedings, 22nd International Conference, Linac 2004, Luebeck, Germany, August 16-20, 2004*, 2004. [Online]. Available: http://weblib.cern.ch/abstract?CERN-AB-2004-041-RF.

[76] T. Argyropoulos, N. Catalan-Lasheras, A. Grudiev, G. Mcmonagle, E. Rodriguez-Castro, I. Syrachev, R. Wegner, B. Woolley, W. Wuensch, H. Zha, V. Dolgashev, G. Bowden, A. Haase, T. G. Lucas, M. Volpi, D. Esperante-Pereira, and R. Rajamäki, "Design, fabrication, and high-gradient testing of an X-band, traveling-wave accelerating structure milled from copper halves," *Phys. Rev. Accel. Beams*, vol. 21, p. 061 001, 6 Jun. 2018. DOI: 10.1103/PhysRevAccelBeams.21.061001. [Online]. Available: https://link.aps.org/doi/10.1103/PhysRevAccelBeams.21.061001.

[77] A. Cahill, J. Rosenzweig, V. Dolgashev, S. Tantawi, and S. Weathersby, "High gradient experiments with X-band cryogenic copper accelerating cavities," *Physical Review Accelerators and Beams*, vol. 21, no. 10, p. 102 002, 2018.

[78] P. M. Lapostolle and A. L. Septier, *Linear Accelerators*. Amsterdam: North-Holland, 1970.

[79] G. A. Loew and R. Talman, "Elementary principles of linear accelerators," in *AIP Conference Proceedings*, AIP, vol. 105, 1983, pp. 1–91.

[80] K. Wille, *The physics of particle accelerators: an introduction*. Clarendon Press, 2000.

[81] A. Lunin, V. Yakovlev, and A. Grudiev, "Analytical solutions for transient and steady state beam loading in arbitrary traveling wave accelerating structures," *Phys. Rev. ST Accel. Beams*, vol. 14, p. 052 001, 5 May 2011. DOI: 10.1103/PhysRevSTAB.14.052001. [Online]. Available: https://link.aps.org/doi/10.1103/PhysRevSTAB.14.052001.

[82] R. B. Neal, "Design of linear electron accelerators with beam loading," *Journal of Applied Physics*, vol. 29, no. 7, pp. 1019–1024, 1958.

[83] B. Spataro, "Studio delle sezioni acceleratrici ad onda viaggiante e gradiente approssimativamente costante," Istituto Nazionale di Fisica Nucleare (Laboratori Nazionali di Frascati), Tech. Rep. L-87, 1986.

[84] Z. D. Farkas, H. A. Hogg, G. A. Loew, and P. B. Wilson, "SLED: A method of doubling SLAC's energy," in *Proc. Of 9th Int. Conf. On High Energy Accelerators, SLAC*, 1974, p. 576.

[85] I. Syrachev, "The Progress of X-Band "Open" Cavity RF Pulse Compression Systems," in *Proceedings of the 4th European Particle Accelerator Conference EPAC94, London, UK*, 1994, pp. 375–379.

[86] P. Wang, H. Chen, J. Shi, I. Syratchev, W. Wuensch, and H. Zha, "The RF Design of a Compact, High Power Pulse Compressor with a Flat Output Pulse," in *Proc. of International Particle Accelerator Conference (IPAC'16), Busan, Korea, May 8-13, 2016*, (Busan, Korea), ser. International Particle Accelerator Conference, doi:10.18429/JACoW-IPAC2016-THPMW022, Geneva, Switzerland: JACoW, Jun. 2016, pp. 3591–3593, ISBN: 978-3-95450-147-2. DOI: doi:10.18429/JACoW-IPAC2016-THPMW022. [Online]. Available: http://jacow.org/ipac2016/papers/thpmw022.pdf.

[87] J. Le Duff, "High-field electron linacs," in *CERN Yellow report CERN-95-06*, 1995.

[88] D. Alesini, "Power coupling," in *Proceedings of the CAS-CERN Accelerator School: Advanced Accelerator Physics, RF for Accelerators, Ebeltoft, Denmark, 8 - 17 Jun 2010, CERN-2011-007*, 2011.

[89] L. Laurent, S. Tantawi, V. Dolgashev, C. Nantista, Y. Higashi, M. Aicheler, S. Heikkinen, and W. Wuensch, "Experimental study of rf pulsed heating," *Physical review special topics-accelerators and beams*, vol. 14, no. 4, p. 041 001, 2011.

[90] C. Adolphsen, W. Baumgartner, K. Jobe, F. Le Pimpec, R. Loewen, D. McCormick, M. Ross, T. Smith, J. Wang, and T. Higo, "Processing Studies of X-band Accelerator Structures at the NLCTA," in *PACS2001. Proceedings of the 2001 Particle Accelerator Conference (Cat. No. 01CH37268)*, IEEE, vol. 1, 2001, pp. 478–480.

[91] J. Wang, "Recent Progress in R& D of Advanced Room Temperature Accelerator Structures," in *Proc. of LINAC2002, Gyeongju, Korea, August 2002*, 2002.

[92] C. Nantista, S. Tantawi, and V. Dolgashev, "Low-field accelerator structure couplers and design techniques," *Physical Review Special Topics-Accelerators and Beams*, vol. 7, no. 7, p. 072 001, 2004.

[93] T. Boyd Jr, "Kilpatrick's criterion," *Los Alamos Group AT-1 report AT-1*, vol. 82, p. 28, 1982.

[94] D. P. Pritzkau, "RF pulsed heating," PhD thesis, Stanford University, 2001.

[95] C. Adolphsen, "Update on structure high gradient development," Tech. Rep. NLC News - Vol. 3, No. 7, July 2002, 2002.

[96] G. E. Vibrans, "Vacuum voltage breakdown as a thermal instability of the emitting protrusion," *Journal of Applied Physics*, vol. 35, no. 10, pp. 2855–2857, 1964.

[97] M. Ferrario, M. Migliorati, and L. Palumbo, "Wakefields and Instabilities in Linear Accelerators," in *Proceedings of the CAS-CERN Accelerator School: Advanced Accelerator Physics, Trondheim, Norway, 19–29 August 2013, CERN-2014-009*, 2014.

[98] K. L. Bane, "Short-range dipole wakefields in accelerating structures for the NLC," Stanford Linear Accelerator Center, Menlo Park, CA (US), Tech. Rep. SLAC-PUB-9663, 2003.

[99] K. Bane and M. Sands, "Wake fields of very short bunches in an accelerating cavity," Tech. Rep. SLAC-PUB-4441, 1987.

[100] R. Palmer, "A qualitative study of wake fields for very short bunches," *Part. Accel.*, vol. 25, no. SLAC-PUB-4433, pp. 97–106, 1987.

[101] K. L. Bane, "Calculation of the short-range longitudinal wakefields in the NLC Linac," Stanford Linear Accelerator Center (SLAC), Menlo Park, CA, Tech. Rep. SLAC-PUB-7862, 1998.

[102] W. Panofsky and W. Wenzel, "Some considerations concerning the transverse deflection of charged particles in radio-frequency fields," *Review of Scientific Instruments*, vol. 27, no. 11, pp. 967–967, 1956.

[103] P. B. Wilson, "Introduction to wakefields and wake potentials," in *AIP Conference Proceedings*, AIP, vol. 184, 1989, pp. 525–564.

[104] O. H. Altenmueller, W. Herrmannsfeldt, Z. Farkas, C. Kruse, G. Loew, R. F. Koontz, E. Farinholt, H. Hoag, and R. H. Miller, "Beam breakup experiments at SLAC," Stanford Linear Accelerator Center, Menlo Park, CA (US), Tech. Rep. SLAC-PUB-224, 1966.

[105] A. W. Chao, *Physics of collective beam instabilities in high energy accelerators*. Wiley, 1993.

[106] "EuPRAXIA@SPARC_LAB Conceptual Design Report," Tech. Rep. INFN - 18-03/LNF, 2018.

[107] M. Ferrario *et al.*, "SPARC_LAB present and future," *Nucl. Instrum. Meth. B*, vol. 309, pp. 183–188, 2013.

[108] P. Walker *et al.*, "HORIZON 2020 EuPRAXIA Design Study," in *Proc. of International Particle Accelerator Conference (IPAC'17), Copenhagen, Denmark, 14-19 May, 2017*, (Copenhagen, Denmark), ser. International Particle Accelerator Conference, Geneva, Switzerland: JACoW, May 2017, pp. 1265–1268, ISBN: 978-3-95450-182-3. DOI: https://doi.org/10.18429/JACoW-IPAC2017-TUOBB3.

[109] *EuPRAXIA website*, http://www.eupraxia-project.eu/.

[110] C. Vaccarezza, D. Alesini, A. Bacci, A. Cianchi, E. Chiadroni, M. Croia, M. Diomede, M. Ferrario, A. Gallo, A. Giribono, A. Latina, A. Marocchino, V. Petrillo, R. Pompili, S. Romeo, M. R. Conti, A. Rossi, L. Serafini, and B. Spataro, "EUPRAXIA@SPARC_LAB: Beam dynamics studies for the X-band Linac," *Nuclear Instruments and Methods in Physics Research Section A: Accelerators, Spectrometers, Detectors and Associated Equipment*, vol. 909, pp. 314–317, 2018, 3rd European Advanced Accelerator Concepts workshop (EAAC2017), ISSN: 0168-9002. DOI: https://doi.org/10.1016/j.nima.2018.01.100. [Online]. Available: http://www.sciencedirect.com/science/article/pii/S0168900218301475.

[111] D. Alesini, S. Bertolucci, M. Biagini, C. Biscari, R. Boni, M. Boscolo, M. Castellano, A. Clozza, G. D. Pirro, A. Drago, A. Esposito, M. Ferrario, V. Fusco, A. Gallo, A. Ghigo, S. Guiducci, M. Incurvati, P. Laurelli, C. Ligi, F. Marcellini, M. Migliorati, C. Milardi, L. Palumbo, L. Pellegrino, M. Preger, P. Raimondi, R. Ricci, C. Sanelli, F. Sgamma, B. Spataro, M. Serio, A. Stecchi, A. Stella, F. Tazzioli, C. Vaccarezza, M. Vescovi, C. Vicario, M. Zobov, E. Acerbi, F. Alessandria, D. Barni, G. Bellomo, I. Boscolo, F. Broggi, S. Cialdi, C. DeMartinis, D. Giove, C. Maroli, V. Petrillo, M. Rome', L. Serafini, E. Chiadroni, G. Felici, D. Levi, M. Mastrucci, M. Mattioli, G. Medici, G. Petrarca, L. Catani, A. Cianchi, A. D'Angelo, R. D. Salvo, A. Fantini, D. Moricciani, C. Schaerf, R. Bartolini, F. Ciocci, G. Dattoli, A. Doria, F. Flora, G. Gallerano, L. Giannessi, E. Giovenale, G. Messina, L. Mezi, P. Ottaviani, L. Picardi, M. Quattromini, A. Renieri, C. Ronsivalle, L. Avaldi, C. Carbone, A. Cricenti, A. Pifferi, P. Perfetti, T. Prosperi, V. Albertini, C. Quaresima, and N. Zema, "The SPARC project: a high-brightness electron beam source at LNF to drive a SASE-FEL experiment," *Nuclear Instruments and Methods in Physics Research Section A: Accelerators, Spectrometers, Detectors and Associated Equipment*, vol. 507, no. 1, pp. 345–349, 2003, Proceedings of the 24th International Free Electron Laser Conference and the 9th Users Workshop., ISSN: 0168-9002. DOI: https://doi.org/10.1016/S0168-9002(03)00943-4. [Online]. Available: http://www.sciencedirect.com/science/article/pii/S0168900203009434.

[112] A. Giribono, A. Bacci, E. Chiadroni, A. Cianchi, M. Croia, M. Ferrario, A. Marocchino, V. Petrillo, R. Pompili, S. Romeo, *et al.*, "Eupraxia@ sparc_lab: The high-brightness rf photo-injector layout proposal," *Nuclear Instruments and Methods in Physics Research Section A: Accelerators, Spectrometers, Detectors and Associated Equipment*, vol. 909, pp. 282–285, 2018.

[113] E. Chiadroni, D. Alesini, M. Anania, A. Bacci, M. Bellaveglia, A. Biagioni, F. Bisesto, F. Cardelli, G. Castorina, A. Cianchi, *et al.*, "Beam manipulation for resonant plasma wakefield acceleration," *Nuclear Instruments and Methods in Physics Research Section A: Accelerators, Spectrometers, Detectors and Associated Equipment*, vol. 865, pp. 139–143, 2017.

[114] A. Marocchino, E. Chiadroni, M. Ferrario, F. Mira, and A. R. Rossi, "Design of high brightness plasma wakefield acceleration experiment at sparc_lab test facility with particle-in-cell simulations," *Nuclear Instruments and Methods in Physics Research Section A: Accelerators, Spectrometers, Detectors and Associated Equipment*, vol. 909, pp. 408–413, 2018.

[115] S. Romeo, E. Chiadroni, M. Croia, M. Ferrario, A. Giribono, A. Marocchino, F. Mira, R. Pompili, A. R. Rossi, and C. Vaccarezza, "Simulation design for forthcoming high quality plasma wakefield acceleration experiment in linear regime at sparc_lab," *Nuclear Instruments and Methods in Physics Research Section A: Accelerators, Spectrometers, Detectors and Associated Equipment*, vol. 909, pp. 71–75, 2018.

[116] *CPI website*, `http://www.cpii.com/`.

[117] A. Grudiev, talk at INFN-LNF, Dec. 2016.

[118] *ABCI website*, `http://abci.kek.jp/abci.htm`.

[119] I. Zagorodnov and T. Weiland, "TE/TM field solver for particle beam simulations without numerical Cherenkov radiation," *Physical Review Special Topics-Accelerators and Beams*, vol. 8, no. 4, p. 042 001, 2005.

[120] I. Zagorodnov, "Indirect methods for wake potential integration," *Physical Review Special Topics-Accelerators and Beams*, vol. 9, no. 10, p. 102 002, 2006.

[121] *ECHO website*, `https://echo4d.de/`.

[122] W. Bruns, "GdfidL: A finite difference program for arbitrarily small perturbations in rectangular geometries," *IEEE transactions on magnetics*, vol. 32, no. 3, pp. 1453–1456, 1996.

[123] *Gdfidl website*, `http://www.gdfidl.de/`.

[124] *CST Studio Suite website*, `https://www.3ds.com/products-services/simulia/products/cst-studio-suite/`.

[125] M. Borland, "Elegant: A flexible SDDS-compliant code for accelerator simulation," Argonne National Lab., IL (US), Tech. Rep., 2000.

[126] M. De Loos and S. Van Der Geer, "General Particle Tracer: A new 3D code for accelerator and beamline design," in *5th European Particle Accelerator Conference*, 1996, p. 1241.

[127] *General Particle Tracer (GPT) website*, http://www.pulsar.nl/gpt/.

[128] D. Schulte, "Multi-Bunch Calculations in the CLIC Main Linac," in *23rd Particle Accelerator Conference, PAC2009, 4 - 8 May 2009, Vancouver, British Columbia, Canada*, 2009.

[129] M. Shumail and V. A. Dolgashev, "Exact solution of multi-bunch instabilities for ultra-relativistic constant energy bunches in particle accelerators," *Physica Scripta*, vol. 94, no. 6, p. 065 208, 2019.

[130] *ANSYS HFSS website*, http://www.ansys.com/products/electronics/ansys-electronics-desktop.

[131] *MATLAB website*, https://www.mathworks.com/products/matlab.html.

[132] *MATLAB in Wikipedia*, https://en.wikipedia.org/wiki/MATLAB.

[133] *Autodesk Inventor website*, https://www.autodesk.com/products/inventor/overview.

[134] "Status of high gradient X-band LINAC design for the EUPRAXIA@SPARC_LAB project and XLS accelerating structures design," in *Eleventh international workshop on high gradient acceleration, HG2018, Shanghai Institute of Applied Physics, Chinese Academy of Sciences (SINAP), June 4-8, 2018*, 2018. [Online]. Available: https://indico.cern.ch/event/675785/contributions/3022074/attachments/1663416/2665749/Alesini_HG2018.pptx.

[135] *SAES website*, https://www.saesgetters.com/.

[136] S. Bini, *Private communication.*

[137] F. Cardelli, "Design realization and commissioning of RF Power system and accelerating structures for a Gamma Source," PhD thesis, Sapienza University of Rome, 2017.

[138] D. Alesini, M. Bellaveglia, S. Bini, A. Gallo, V. Lollo, L. Pellegrino, L. Piersanti, F. Cardelli, M. Migliorati, A. Mostacci, *et al.*, "Design of high gradient, high repetition rate damped C-band rf structures," *Physical Review Accelerators and Beams*, vol. 20, no. 3, p. 32 004, 2017.

[139] L. Xiao, R. Boyce, D. Dowell, Z. Li, C. Limborg-Deprey, and J. Schmerge, "Dual feed RF gun design for the LCLS," in *Proceedings of the 2005 Particle Accelerator Conference*, IEEE, 2005, pp. 3432–3434.

[140] A. Grudiev, *Private communication.*

[141] A. Cahill, M. D. Forno, and V. Dolgashev, "TM01 Mode Launcher for Use in High Brightness Photoguns," in *Proc. of International Particle Accelerator Conference (IPAC'16), Busan, Korea, May 8-13, 2016*, (Busan, Korea), ser. International Particle Accelerator Conference, doi:10.18429/JACoW-IPAC2016-MOPMW039, Geneva, Switzerland: JACoW, Jun. 2016, pp. 491–493, ISBN: 978-3-95450-147-2. DOI: doi:10.18429/JACoW-IPAC2016-MOPMW039. [Online]. Available: http://jacow.org/ipac2016/papers/mopmw039.pdf.

[142] *CompactLight website*, http://www.compactlight.eu.

[143] A. Mak, P. Salen, V. Goryashko, and J. Clarke, "Science Requirements and Performance Specification forthe CompactLight X-Ray Free-Electron Laser," STFC Daresbury Laboratory, Warrington, United Kingdom, Tech. Rep. 2019/01, 2019, p. 18.

[144] D. Jaroszynski, R. Prazeres, F. Glotin, and J. Ortega, "Two-color free-electron laser operation," *Physical review letters*, vol. 72, no. 15, p. 2387, 1994.

[145] A. Castilla *et al.*, "Ka-Band Linearizer Studies for a Compact Light Source," in *Proc. 10th International Partile Accelerator Conference (IPAC'19), Melbourne, Australia, 19-24 May 2019*, (Melbourne, Australia), ser. International Partile Accelerator Conference, https://doi.org/10.18429/JACoW-IPAC2019-WEPRB068, Geneva, Switzerland: JACoW Publishing, Jun. 2019, pp. 2976–2979, ISBN: 978-3-95450-208-0. DOI: doi:10.18429/JACoW-IPAC2019-WEPRB068. [Online]. Available: http://jacow.org/ipac2019/papers/weprb068.pdf.

[146] *NLCTA website*, https://portal.slac.stanford.edu/sites/ard_public/facet/newnav/Pages/tf/nlcta/whatis.aspx.

[147] T. Raubenheimer, "Zeroth-order Design Report for the Next Linear Collider," Stanford Linear Accelerator Center, Menlo Park, CA (US), Tech. Rep. SLAC-R-474, 1997.

[148] R. D. Ruth, C. Adolphsen, K. Bane, R. Boyce, D. Burke, R. Calin, G. Caryotakis, R. Cassel, S. L. Clark, H. Deruyter, *et al.*, "The next linear collider test accelerator," in *Proceedings of International Conference on Particle Accelerators*, IEEE, 1993, pp. 543–545.

[149] P. B. Wilson, Z. D. Farkas, and R. D. Ruth, "SLED II: A new method of RF pulse compression," in *Proceedings of the Linear Accelerator Conference 1990, Albuquerque, New Mexico, USA*, 1990.

[150] J. Wang, C. Adolphsen, R. Atkinson, W. Baumgartner, J. Eichner, R. Fuller, S. Gold, S. Hanna, S. Holmes, R. Koontz, *et al.*, "RF Systems for the NLCTA," in *Proceedings of the 1997 Particle Accelerator Conference (Cat. No. 97CH36167)*, IEEE, vol. 3, 1997, pp. 3042–3044.

[151] J. Wang, C. Adolphsen, K. Bane, G. Bowden, D. Burke, H. Deruyter, J. Cornuelle, Z. Farkas, W. Fowkes, S. Hanna, *et al.*, "Accelerator Structure R&D for Linear Colliders," in *Proceedings of the 1999 Particle Accelerator Conference (Cat. No. 99CH36366)*, IEEE, vol. 5, 1999, pp. 3423–3425.

[152] M. Aicheler, *Private communication.*

[153] A. Gallo, *Private communication.*

[154] *Canon electron tubes and devices website*, `https://etd.canon/en/index.html`.

[155] I. Zagorodnov and T. Weiland, "The short-range transverse Wakefields in Tesla accelerating structure," in *Proceedings of the 2003 Particle Accelerator Conference*, IEEE, vol. 5, 2003, pp. 3249–3251.

[156] M. Behtouei, "A Ka-band linearizer TW accelerating structure for the Compact Light XLS project," Istituto Nazionale di Fisica Nucleare (Laboratori Nazionali di Frascati), Tech. Rep. INFN-19-11/LNF, 2019.

[157] L. Faillace, *Private communication.*

[158] *Thermal expansion in Wikipedia*, `https://en.wikipedia.org/wiki/Thermal_expansion`.

List of Figures

List of Tables